Design and Calibration of High Accuracy Spherical Joints

by

Alec Robertson

Bachelor of Engineering in Mechanical Engineering
Monash University, 1996

Bachelor of Science in Computer Science and Applied Mathematics
Monash University, 1994

Melbourne, Australia

Submitted to the Department of Mechanical Engineering
in Partial Fulfillment of the Requirements for the Degree of

Master of Science in Mechanical Engineering
at the
Massachusetts Institute of Technology

May 2003

© 2003 Massachusetts Institute of Technology
All Rights Reserved

Signature of Author . . . .
Department of Mechanical Engineering
May 9, 2002

Certified by . . . .
Alexander H. Slocum
Professor, Mechanical Engineering
Thesis Supervisor

Accepted by . . . .
Ain A. Sonin
Chairman, Department Committee on Graduate Students

BARKER

MASSACHUSETTS INSTITUTE
OF TECHNOLOGY
JUL 0 8 2003
LIBRARIES

Design and Calibration of High Accuracy Spherical Joints

by

ALEC ROBERTSON

Submitted to the Department of Mechanical Engineering
on May 9, 2003 in Partial Fulfillment of the
Requirements for the Degree of Masters of Science in
Mechanical Engineering

Abstract

A fundamental limit associated with current industrial robots is their accuracy. Parallel robots offer many benefits compared to serial robots due to their superior accuracy and stiffness. Amongst the most important components in these robots are the three degree of freedom bearings connecting the robot's parallel arms. Spherical joints have been developed based on a ball and socket configuration, preloaded by rings of magnets arrayed about the socket. Four prototypes have been implemented based on point, rolling, sliding and fluid contact mechanisms and a spherical-kinematic test mechanism has been constructed to automate the measurement of joint accuracy.

The average error for the joint prototypes is found to be 4 micrometers and the maximum error is 12 micrometers; which can be reduced to 8 micrometers through calibration. The maximum preload force is found to be approximately 100N, rendering these joints suitable for high accuracy non-contact applications, such as in-line measurement and inspection.

Thesis Supervisor: Professor Alexander H. Slocum

Title: Professor of Mechanical Engineering

ACKNOWLEDGEMENTS

Funding for this research was provided by ABB Corporate Research, under the guidance of Professor Torgny Brogårdh and Dr. ZhongXue Gan. I would like to thank both Torgny and Gan for their help throughout the Masters thesis. Thanks must also go to my advisor Professor Alexander Slocum and to my MIT colleagues who helped along the way, in particular Adam Rzepniewski, who worked with me during the initial design phase and Charles Dumont, who helped develop the advanced modeling algorithms. Finally, I would like to thank my family and friends for their support and feedback throughout the thesis.

TABLE OF CONTENTS

ACKNOWLEDGEMENTS **5**

TABLE OF CONTENTS **7**

LIST OF FIGURES **11**

LIST OF TABLES **15**

NOMENCLATURE **17**

CHAPTER 1. INTRODUCTION **19**
1.1 Motivation 19
1.2 Parallel Robot Overview 20
1.3 Parallel Robot Joints 22
1.4 Joint Survey 24
1.5 Functional Requirements 26
    1.5.1 Spherical motion 26
    1.5.2 Contact Type 28
    1.5.3 Preload 28
1.6 Conclusion 30

CHAPTER 2. DESIGN PROCESS **33**
2.1 Overview 33
2.2 Joint Design 35
    2.2.1 Strategy Phase 35
    2.2.2 Concept Phase 39
    2.2.3 Module Phase 45
    2.2.4 Manufacture 48
2.3 Test Rig Design 53
    2.3.1 Strategy Phase 53
    2.3.2 Concept Phase 55
    2.3.3 Module Phase 59
    2.3.4 Manufacture 61
2.4 Conclusion 63

CHAPTER 3. ANALYSIS AND MEASUREMENT **65**
3.1 Overview 65
3.2 Preload Analysis 68
3.2.1 Magnet Characterization 68
3.2.2 Sliding and Fluid Contact Prototypes 68
3.2.3 Point and Rolling Contact Prototypes 72
3.3 Accuracy Analysis 73
3.3.1 Sphere Fit Model 73
3.3.2 Kinematic Model 74
3.4 Thermal Analysis 81
3.5 Contact Analysis 82
3.6 Preload Measurement 84
3.7 Measurement and Calibration 85
3.7.1 Rolling Contact Joint 85
3.7.2 Point Contact Joint 88
3.7.3 Sliding Contact Joint 89
3.7.4 Joint Comparison 90
3.8 Conclusions 91

CHAPTER 4. FLUID CONTACT JOINT **93**
4.1 Overview 93
4.2 Analysis 94
4.2.1 Fluid Flow Analysis 94
4.2.2 Preload Analysis 101
4.2.3 Stiffness Analysis 103
4.3 Manufacture 107
4.4 Measurement 108
4.4.1 Fluid Flow Measurement 108
4.4.2 Stiffness Measurement 110
4.4.3 Accuracy Measurement 116
4.4.4 Joint Comparison 117
4.5 Conclusions 119

CHAPTER 5. ADVANCED MODELING **121**
5.1 Overview 121
5.2 Genetic Programming Based Model Improvement 122

5.2.1 Introduction 122
5.2.2 Implementation 124
5.2.3 Results and Analysis 128
5.2.4 Framework 133

5.3 Spherical Joint Models 135

5.4 Conclusions 139

CHAPTER 6. CONCLUSIONS **141**

CHAPTER 7. REFERENCES **145**

LIST OF FIGURES

Figure 1.1 Delta robot configuration 20
Figure 1.2 ABB IRB340 robot 20
Figure 1.3 Tau robot configuration 21
Figure 1.4 Tau measurement prototype 21
Figure 1.5 Three degree of freedom spherical joint 23
Figure 1.6 Delta robot joint pair 23
Figure 1.7 Tau robot prototype 23
Figure 1.8 Modified universal joint 23
Figure 1.9 Automotive rod end 24
Figure 1.10 Ball bar mechanisms 24
Figure 1.11 Flat pad air bearing 25
Figure 1.12 Spherical joint 25
Figure 2.1 Modified universal joint 35
Figure 2.2 Magnetic air bearing 35
Figure 2.3 Flexure joint 35
Figure 2.4 Slot and ball 36
Figure 2.5 Spring preload 36
Figure 2.6 Double cup 36
Figure 2.7 Sliding arm universal joint 36
Figure 2.8 Modified universal joint 37
Figure 2.9 Kinematic chain 37
Figure 2.10 Porous carbon air 37
Figure 2.11 Magnetic cup 37
Figure 2.12 Sealed spring 37
Figure 2.13 Spherical motion concept tree 40
Figure 2.14 Sliding contact assembly model 48
Figure 2.15 Sliding contact exploded model 48
Figure 2.16 Rolling contact assembly model 49

Figure 2.17 Rolling contact exploded model 49
Figure 2.18 Sliding contact socket 49
Figure 2.19 Sliding contact socket 49
Figure 2.20 Sliding contact joint 49
Figure 2.21 Point contact 50
Figure 2.22 Rolling contact 50
Figure 2.23 Rolling contact joint 50
Figure 2.24 Double ball bar 53
Figure 2.25 Universal mechanism 53
Figure 2.26 Actuated clamp 53
Figure 2.27 Test rig base 61
Figure 2.28 Test rig complete mechanism 61
Figure 2.29 OMAX waterjet path. 62
Figure 2.30 Spherical kinematic test rig 62
Figure 2.31 Test rig and CMM probe 62
Figure 3.1 Rolling contact 66
Figure 3.2 Point contact 66
Figure 3.3 Sliding contact 66
Figure 3.4 Test rig 66
Figure 3.5 Generic spherical joint schematic 68
Figure 3.6 Force balance for socket fixed mounting 69
Figure 3.7 Socket fixed configuration 70
Figure 3.8 Ball fixed configuration 70
Figure 3.9 Preload characteristics for sliding and fluid contact joints 70
Figure 3.10 Sliding and fluid contact force distribution 71
Figure 3.11 Preload characteristics for point and rolling contact joint 72
Figure 3.12 Spherical joint sphere fit model 73
Figure 3.13 Spherical joint structural loop 74
Figure 3.14 Spherical joint nominal kinematic model 75
Figure 3.15 Singular value decomposition 75
Figure 3.16 Calibration algorithm 77

Figure 3.17 Error model inverse kinematics 78
Figure 3.18 Error budget repeatability 79
Figure 3.19 Error budget accuracy 79
Figure 3.20 Thermal expansion of joint socket 81
Figure 3.21 Contact mechanics for point and rolling contact joints 82
Figure 3.22 Deformation between two spheres 82
Figure 3.23 Hertz contact deformation coefficients 83
Figure 3.24 Measurement of magnet force 84
Figure 3.25 Measured and predicted preload forces 84
Figure 3.26 Accuracy distribution of rolling contact prototype 87
Figure 3.27 Accuracy distribution of point contact prototype 88
Figure 3.28 Accuracy distribution of sliding contact prototype 89
Figure 3.29 Maximum and mean residual errors for joint prototypes 90
Figure 3.30 Predicted and measured preload forces 90
Figure 4.1 Fluid contact joint prior to replication 93
Figure 4.2 Polar coordinates and corresponding area and volume elements 94
Figure 4.3 Fluid contact joint schematic 95
Figure 4.4 Navier Stokes equations in cylindrical coordinates 95
Figure 4.5 Flow assumptions 96
Figure 4.6 Reduced Navier Stokes equations 96
Figure 4.7 Flow profile for radial axis equation 97
Figure 4.8 Volume flow rate 97
Figure 4.9 Pressure drop and resistance profiles 98
Figure 4.10 Equivalent socket dimensions in cylindrical coordinates 98
Figure 4.11 Inlet pressure 99
Figure 4.12 Stiffness formulation 100
Figure 4.13 Design flowchart for air bearing joint 102
Figure 4.14 Magnet, air gap and contact stiffness regimes 103
Figure 4.15 Force-displacement schematic for fluid contact joint 104
Figure 4.16 Magnet regime stiffness model 104
Figure 4.17 Fluid regime linearized stiffness model 105

Figure 4.18 Replication material stiffness model 105
Figure 4.19 Brass orifice housing stiffness model 106
Figure 4.20 Air bearing chassis with pneumatic connectors 107
Figure 4.21 Vertical displacement as a function of inlet pressure 108
Figure 4.22 Predicted air gap as a function of inlet pressure 109
Figure 4.23 Texture analyzer mounted with socket and ball 110
Figure 4.24 Force-displacement characteristics with encoder displacement data . . 111
Figure 4.25 Extensometer force-displacement characteristics for tension cycle . . . 112
Figure 4.26 Contact region force-displacement characteristics 113
Figure 4.27 Fluid region force-displacement characteristics 113
Figure 4.28 Force-displacement characteristics for air and no air 115
Figure 4.29 Fluid contact joint residual error distribution 116
Figure 4.30 Maximum and mean residual errors for joint prototypes 117
Figure 4.31 Predicted and measured preload forces 117
Figure 5.1 ABB IRB6400R Industrial Robot 121
Figure 5.2 Compensator model 124
Figure 5.3 Cross over and mutation for linear sequence 126
Figure 5.4 Linear sequence and equations 126
Figure 5.5 Fitness function 127
Figure 5.6 Binary tree crossover 128
Figure 5.7 Fitness vs. generation 129
Figure 5.8 Extrapolation of linear sequence 129
Figure 5.9 Histogram of referenced inputs for standard model 130
Figure 5.10 Linear sequence compensation and equation 131
Figure 5.11 Comparison of calibration models 132
Figure 5.12 Histogram of referenced inputs for improved model 133
Figure 5.13 Histogram of referenced inputs for spherical joint 135
Figure 5.14 Linear sequence compensation for spherical joint 135
Figure 5.15 Relationship between error parameters and axis 1 motion 136
Figure 5.16 Accuracy distribution for improved joint model 138

LIST OF TABLES

TABLE 1.1 Functional specifications 26
TABLE 1.2 Preliminary functional requirements 29
TABLE 2.1 Joint strategy table 38
TABLE 2.2 Spherical motion concepts 39
TABLE 2.3 Contact type concepts 40
TABLE 2.4 Preload concepts 41
TABLE 2.5 Joint design concepts 42
TABLE 2.6 Concept evaluation chart 44
TABLE 2.7 Sliding and fluid contact joint generations 45
TABLE 2.8 Point and rolling contact joint generations 47
TABLE 2.9 Test rig strategies 54
TABLE 2.10 Test rig concepts 55
TABLE 2.11 Test rig concepts for accuracy measurement 56
TABLE 2.12 Concept evaluation chart 58
TABLE 2.13 Test rig design generations 59
TABLE 3.1 Preload optimization for sliding contact joint 71
TABLE 3.2 Reduced calibration model parameters 76
TABLE 3.3 Hertz contact deformation spreadsheet 83
TABLE 3.4 Comparison of calibration methods 86
TABLE 3.5 Kinematic calibration 87
TABLE 4.1 Preload design guide for fluid bearing joint 101
TABLE 4.2 Fluid flow design guide for fluid contact joint 102
TABLE 4.3 Stiffness coefficients for fluid and contact regimes 114
TABLE 5.1 Mathematical operators and input registers 125
TABLE 5.2 Error parameters for improved joint model 137

NOMENCLATURE

UPPER CASE:

F	Force [N]. Forward kinematics function [m]
X	Position vector [m]
M	Measurement position vector [m]
E	Error position vector. Elastic modulus [Pa]
J	Jacobian matrix
U	Left eigenmatrix
V	Right eigenmatrix
S	Singular value matrix
L	Length [m]
T	Temperature [$^\circ$C]
V	Volume [m^3]
A	Area [m^2]
R	Resistance [Pa/m^3]
P	Pressure [Pa]
Q	Flow rate [m^3/s]
K	Stiffness [N/m]

LOWER CASE:

r	Radius [m]
l	Length [m]
u	Velocity [m/s]
x	Position [m]
y	Position [m]
z	Position [m]
h	Air gap [m]

GREEK:

θ	Angle [rad]
γ	Angle [rad]
ϕ	Angle [rad]
α	Angle [rad]. Coefficient [-]
ε	Error parameter vector. Angle [rad]
δ	Displacement [m]
α_T	Coefficient of thermal expansion [m/$^\circ$C]
λ	Hertz contact coefficient [-]
ν	Poisson's ratio [-]
μ	Viscosity [Ns/m^2]
η	Conversion factor [-]
β	Coefficient [-]

Chapter 1

INTRODUCTION

1.1 Motivation

A fundamental limit associated with current industrial robots is their accuracy. Typically, special machines are used in applications such as measurement, high precision manufacturing, machining and assembly. However, there is a growing demand from industry to introduce more flexible production methods for these high precision applications and thus new robot concepts and robot components are required. Robot manufacturers are undertaking an investigation into a new family of parallel arm robots to fulfill these demands for higher accuracy. Amongst the most important components in these robots are the bearings, especially for the two or three degree of freedom (DOF) joints connecting the robot's parallel arms. It is therefore very important to build up a bearing technology expertise to be able to optimize bearings and bearing concepts to the different demands on parallel arm robots for different applications. The bearing technology consists of both bearing kinematics and material science. Examples of kinematics are revolute, universal and ball and socket joints and examples of materials are steel, aluminum, ceramics and plastics. Ball and socket bearings offer high accuracy and a large singularity free workspace, however one significant problem with these bearings is friction between two surfaces while sliding relative to one another. One possibility to reduce the friction significantly while simultaneously increasing the accuracy is to use aerostatic bearings.

1.2 Parallel Robot Overview

A common parallel robot form is the delta structure *[Clavel, 1989]* which is shown in Figure 1.1. This robot comprises three sets of two links which intersect at a triangular end-effector plate such that each pair connects to the midpoint of each side of the plate. This provides six connection points, which fully constrains the motion of the end-effector. The necessary degrees of freedom are provided by three rotary actuators connected to the upper ends of the arm pairs, constraining all rotations of the triangular plate and allowing three translational degrees of freedom. This structure is referred to as a 2-2-2 configuration to describe the connection of the arms to the plate. The ABB IRB340 robot, Figure 1.2, is an example of a Delta implementation which is typically used for high speed pick and place applications.

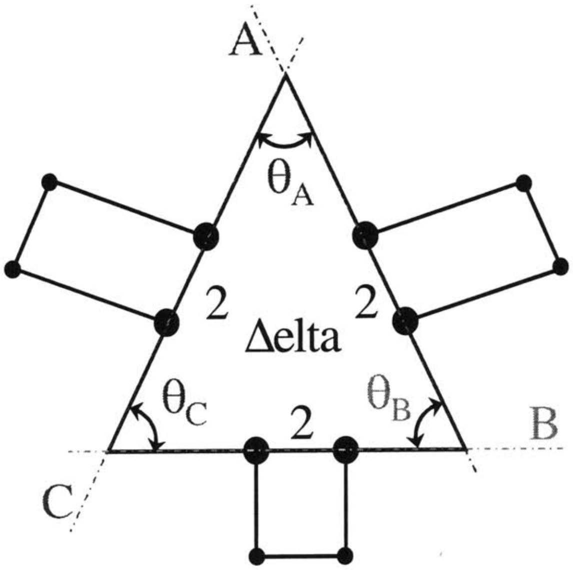

Figure 1.1 Delta robot configuration

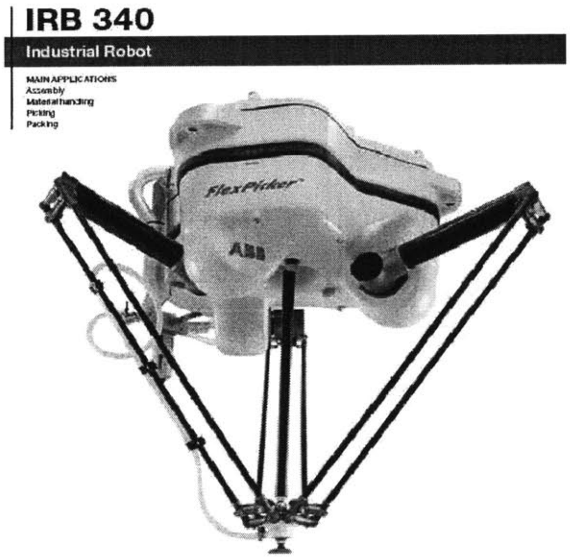

Figure 1.2 ABB IRB340 robot

The Delta robot configuration is advantageous due to its simplicity and symmetry, which provides for consistent performance and high stiffness throughout the majority of the workspace. However, the workspace to robot volume ratio is low, as is typical of many parallel manipulators; furthermore, the configuration and stiffness degenerates as the apex angle (θ_A) of the end-effector triangle decreases. If the angle decreases to zero, making the connection between two arms pairs parallel, then the structure inherits an extra degree of freedom and is no longer fully constrained. In order to improve the workspace to robot volume ratio and allow for a greater flexibility in placement of the arms, the Tau configuration was developed *[Brogårdh, 1997]* and *[Brogårdh et al, 1998]*. The basic Tau configuration modifies the Delta structure by constraining the arms in a 3-2-1 configuration as shown in Figure 1.3. This structure allows for arm sets to be mounted in parallel, thus providing a greater scope for possible configurations. The structure is no longer axisymmetric, however, which introduces deviations in performance and stiffness dependent on the location in the workspace and the design of the robot structure. The measurement robot prototype (Figure 1.4) mounts the single arm in the vertical plane with the double and triple arm sets mounted in the horizontal plane. The robot can rotate fully about the central post, allowing for a large workspace to robot volume ratio while maintaining consistent performance and stiffness throughout the workspace.

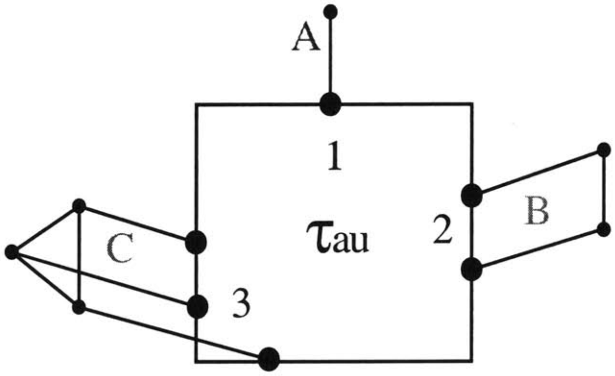

Figure 1.3 Tau robot configuration

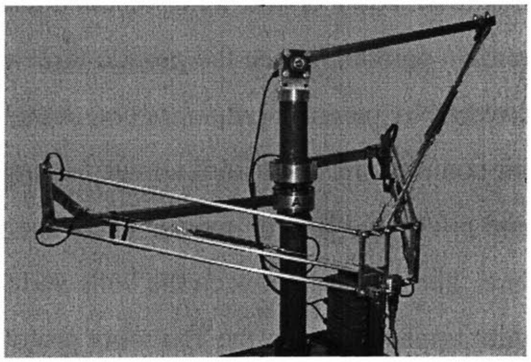

Figure 1.4 Tau measurement prototype

1.3 Parallel Robot Joints

The Delta and Tau configurations constrain rotations in all three axes (roll, pitch and yaw) and allow translation in all three axes (x, y and z). The connection between the arms and the end-effector plate must therefore consist of three degree of freedom joints, and the connection between the rotary actuators and the arms should be two degree of freedom (universal) joints. It is also possible to connect the actuators to the arms via three degree of freedom joints, however this allows the lower arms to rotate freely about their own longitudinal axis, which does not affect the motion of the end-effector. An idealized three degree of freedom joint is shown in Figure 1.5. This joint comprises a ball seated in a hemispherical socket; the socket is attached to the ball by some preload mechanism, such as a spring, magnetic force or negative pressure (suction). This type of joint is typically referred to as a spherical joint as all three rotary axes (roll, pitch and yaw) intersect at the center of the ball. The IRB340 Delta robot configuration allows for a simplification and modularization of the joint connections. The configuration requires that each arm pair remain parallel, hence the pseudo three degree of freedom joint shown in Figure 1.6, and covered by patent *[Hvittfeldt et al, 2002]*, can be used for both the actuator and end-effector connections. This joint allows for large motion in the two key degrees of freedom (roll and pitch) and limited motion about the yaw axis, thus fully constraining the robot structure. The preload between the balls and the spherical sockets is provided by a spring. The joint implemented in the Tau robot prototype uses a combination of standard and modified universal joints (Figure 1.7 and Figure 1.8). Standard universal joints provide roll and pitch degrees of freedom and connect the actuators to the arms. Modified universal joints are mounted between the arms and the end-effector plate and are implemented by introducing a third degree of freedom in the form of a radial ball bearing in one of the shafts. Such joints represent a minor modification on existing technology and can be manufactured with high accuracy and stiffness. However, in the presence of errors, the axes of rotation no longer intersect at a common location, leading to a degeneration in the overall robot accuracy.

In order to improve the accuracy of the Tau robot prototype, a three degree of freedom joint is required which has a large angular working range; high accuracy and stiffness; and is cost effective.

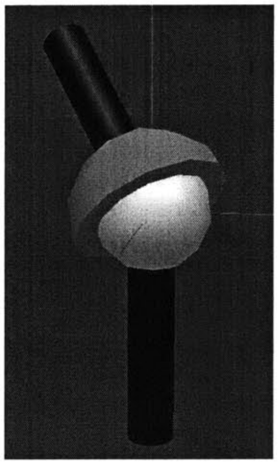

Figure 1.5 Three degree of freedom spherical joint

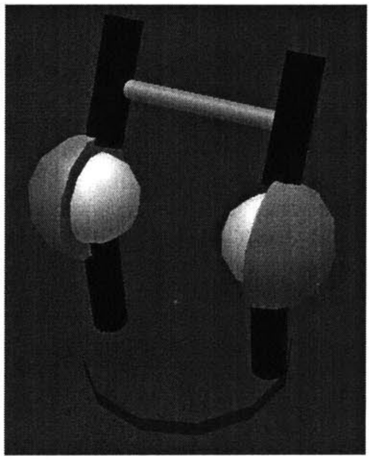

Figure 1.6 Delta robot joint pair

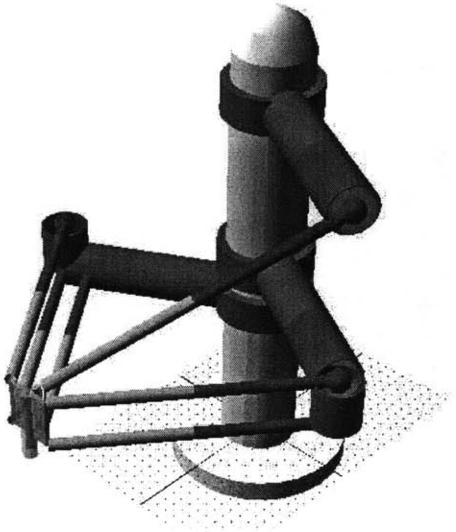

Figure 1.7 Tau robot prototype

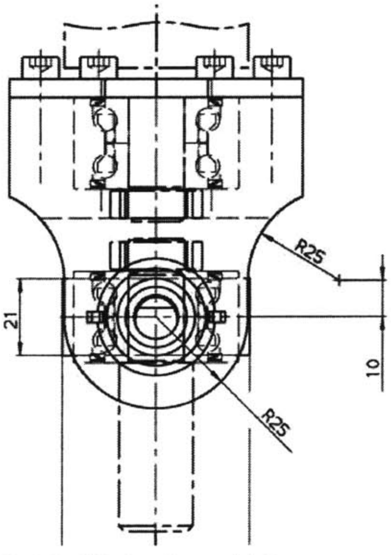

Figure 1.8 Modified universal joint

1.4 Joint Survey

Three degree of freedom joints with a limited working range, commonly referred to as "rod ends", are used extensively in automotive applications where they form the link between the steering rack and the wheel assembly (Figure 1.9). The spherical joints allow for a 30° angular displacement to account for misalignment errors during manufacturing and changes in orientation during operation of the vehicle. However, the angular range of rod end joints is insufficient for the robotics application, which requires an angular workspace on the order of 180°. In order to achieve a large angular range, the field of coordinate measurement machines typically use a ball bar apparatus *[Bryan, 1992]* to calibrate the geometric errors of the machine. These joints are very accurate, display an angular workspace of the order of 180°, and typically consist of a large steel or ceramic ball kinematically located on three points within a socket (Figure 1.10). The preload between the ball and socket is commonly provided by the weight of the ball bar itself, or using small magnets mounted in the socket. These joints, however, are designed for low load operation and can not tolerate large forces between the ball and the socket.

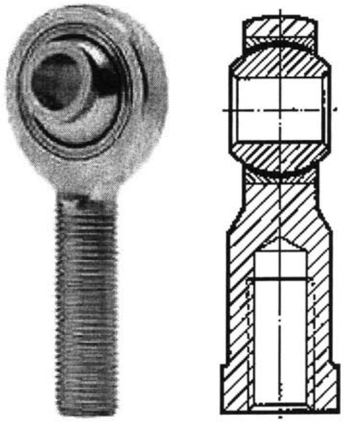

Figure 1.9 Automotive rod end

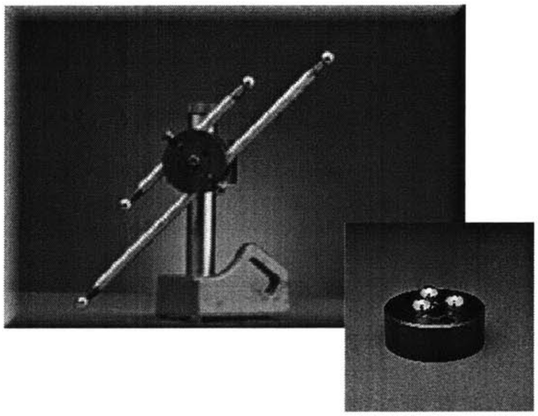

Figure 1.10 Ball bar mechanisms

A fundamental problem with the three degree of freedom spherical joints used in the Delta robot configuration is the friction between the ball and socket. This is reduced through the use of a teflon coating within the socket and a ceramic ball. An alternate approach to friction minimization is to introduce a high pressure film of air in between the ball and socket such as is used in air bearing applications. Typical air bearings designs are based on flat pads (Figure 1.11), with porous graphite or orifice based air intake mechanisms, however spherical rod ends have also been manufactured for high accuracy alignment of shafts spinning at high angular velocity.

Alternative mechanism approaches have been implemented, in order to achieve a large singularity free workspace. The double slotted spherical joint *[Bieg, 1999]*, refer to Figure 1.12, comprises three concentric housings to achieve a singularity free workspace cone of 270°. Whereas this exceeds the required 180°, the complexity of such a mechanism would result in kinematic inaccuracy.

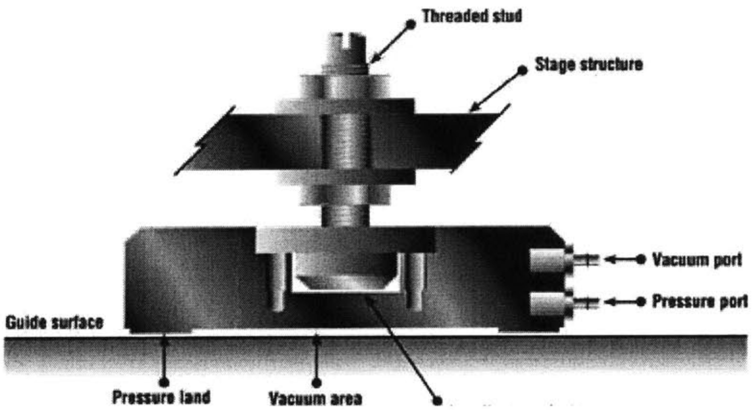
Threaded stud
Stage structure
Vacuum port
Pressure port
Guide surface
Pressure land
Vacuum area

Figure 1.11 Flat pad air bearing

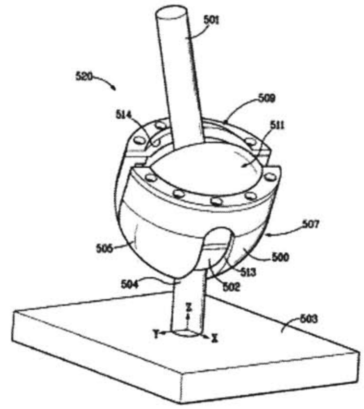
501
520
509
514
511
507
505
500
513
504
502
Z
Y
X
503

Figure 1.12 Spherical joint

1.5 Functional Requirements

The goal of the project is to design and construct a three degree of freedom joint, and determine the accuracy and stiffness of the joint throughout its workspace. These goals give rise to numerous functional requirements, which can be divided into three key categories; spherical motion; type of contact between surfaces; and the preload force required to prevent the joint from separating under operating loads.

TABLE 1.1 Functional specifications

Category	Functional Specifications	
Spherical Motion	Workspace	Restrictions
	Singularities	Elegance
	Joint type	Scaleable
	Accuracy	Maintenance
	Modeling	Modularity
	Calibration	
Contact Type	Contact Type	Lubrication
	Materials	Temperature
	Weight	Sealing
Preload	Preload	Stiffness
	Load capacity	Energy usage
	Safety	Robustness

1.5.1 Spherical motion

- Workspace. The joint should be capable of transcribing a hemispherical workspace, with an angular range of 180°. The deviation in position from an ideal sphere, at any point in the working range, represents the joint accuracy.
- Singularities. There should be no singularities within the required joint workspace.
- Joint type. The kinematic structure of the joint can be described as a chain of multi degree of freedom mechanisms. In order to achieve three degrees of freedom, the possibilities are 1+1+1 chains; 2+1 chains; and 3 chains. The 1+1+1 chain represents a robot-like chain of three orthogonal rotary joints. Whereas this represents a simple structure, it contains singularities within the workspace which are detrimental to performance. The 2+1 chain represents the modified universal joint structure, which contains no singularities, however does introduce kinematic inaccuracy as the third axis is offset from the other two. The 3 chain represents a pure spherical joint where all three

axes intersect at the same location. This structure promises the highest accuracy, however the design is more complex than the alternative approaches.

- Accuracy and repeatability. The accuracy of the joint should be of the order of several micrometers and the repeatability should be of the order of a fraction of a micrometer. High accuracy ensures that the joint does not significantly contribute to the inaccuracy of the robot structure. High repeatability ensures that the joint is not perturbed by stochastic effects such as friction and hysteresis, improving the controllability of the overall structure.
- Modeling. The joint should be described by a simple model, such that it may be integrated into an existing modeling framework without inconsistencies between models. All models should be capable of implementation in a real time system.
- Calibration. It should be possible to measure each joint individually, and then integrate the error parameters into the overall robot structure. Alternatively, it should be possible to calibrate the joint error parameters as a part of the robot structure. This requires the calibration model to be consistent with the existing robot calibration model and measurement techniques.
- Restrictions. No restrictions should be imposed on the robot design. Additionally, implementation of the joint in the robot structure should be optimized for the operating requirements.
- Elegance. The joint aesthetic should be consistent with the existing robot product range.
- Scalable. It should be possible to use the same joint concept for a range of robot sizes, from small pick and place robots similar to the delta robot, to larger machining centers.
- Maintenance. A minimal amount of maintenance should be required, commensurate with the techniques available for existing robots. The existing delta robot joints require no lubrication due to the teflon coating and are typically maintained only following a crash or similar damaging incident.
- Modular. A typical parallel robot requires twelve three degree of freedom joints, ideally a single joint structure can be used. Additionally, the components required for the joint should be readily available, and the part count should be minimize for cost efficiency.

1.5.2 Contact Type

- Contact Type. The connection between contacting members in the joint should be chosen so as to minimize the maintenance required during constant operation of the entire robot structure. Furthermore, friction should be minimized to improve working efficiency.
- Materials. The materials for the joint construction should be chosen to achieve the required temperature, stiffness and maintenance requirements. Additionally readily available materials should be implemented for cost efficiency.
- Weight. The joints should be lightweight, such that they do not significantly contribute to the dynamics of the robot structure.
- Lubrication. Ideally the joints should require no lubrication; however, if lubrication is necessary then the maintenance procedures should be consistent with existing protocols.
- Temperature. Due to the large temperature variations present in many robot applications, temperature effects should be minimized. Appropriate choice of materials and structural design are also key factors determining the temperature variance of the joint structure.
- Sealing. For hygienic applications such as food packaging, or for use in dirty environments, the robot and joints must be sealed in order to prevent contamination of the joint or environment. Sealing of joints individually, and as a part of the robot structure, should be possible.

1.5.3 Preload

- Preload. The joint preload may be applied by any method that is consistent with the functional requirements, in particular the workspace and stiffness requirements.
- Load capacity. The load capacity defines the required preload and is determined by the target robot application.
- Safety. Under no circumstances should the joint prevent a safety hazard to robot users, or surrounding equipment. Highest forces are typically generated during an unexpected incident such as a collision, therefore the joint preload should be designed to hold under such circumstances. A mechanical tether could also be used as an additional safety level.
- Robustness. The joint should remain attached following a collision or similar damaging incident. Furthermore, the joint should be readily handled by maintenance staff and should be relatively impervious to damage by miss-handling.

- Stiffness. High stiffness is required to ensure minimal deflection, and hence accuracy degradation, during operation. The stiffness should be greater than ten newtons per micrometer.
- Energy usage. Ideally the joint should require no additionally energy sources, however if required these should be readily available in existing installations. It should be as efficient as possible to improve cost effectiveness.

The function requirements and some nominal specifications are summarized in Table 1.2.

TABLE 1.2 Preliminary functional requirements

Category	Requirement	Specification
Spherical Motion	Workspace	large (>180deg)
	Singularities	none
	Type	maximize accuracy
	Accuracy	very high (low µm)
	Modeling	consistent with existing methods
	Calibration	potential for calibration of individual joint
	Restrictions	no restrictions, allow optimization of structure
	Elegance	consistent aesthetic
	Scaleable	scaleable within reason
	Maintenance	low/no maintenance required
	Modularity	minimize cost and number of parts
Contact type	Contact type	minimize friction and maintenance
	Material	minimize cost
	Weight	lightweight
	Lubrication	no/low lubrication required
	Temperature	low temperature variance
	Sealing	allow sealing of individual joint
Preload	Preload	no separation
	Load capacity	application defined
	Safety	high safety
	Robustness	no separation following collision
	Stiffness	high (>10N/µm)
	Energy usage	passvely actuated, minimal energy useage

1.6 Conclusion

Investigation into the functional requirements for the spherical joint reveals that spherical motion, contact type and preload are the key requirements. Spherical motion encapsulates such requirements as a singularity-free workspace of 180° and a high accuracy of several micrometers. Contact type represents the interaction between the elements of the joint structure and considers lubrication, materials and the contact mechanics. Finally, the preload determines the mechanism by which the joint is physically constrained, and the resultant stiffness and load capacity of the joint.

An iterative design process is presented in Chapter 2, wherein the key functional requirements are expanded into working prototypes. The implemented process involves the initial development of basic sketches and first order calculations in the strategy phase, followed by the design of simple solid models in the concept phase. Promising concepts are chosen and detailed designs and sub-assemblies developed during the module phase. Finally, a set of working prototypes are developed in the manufacturing phase. The nature of the design process allows the successive specification of design ideas, with a review mechanism inherent through the iterative process. Four prototypes are developed based on a ball and socket configuration, preloaded by magnets within the socket. Each prototype implements a different contact mechanism: point, rolling, sliding and fluid. Test protocols for the validation of joint accuracy and stiffness are also developed using the same design process.

Chapter 3 describes the modeling and testing of three of the four joint prototypes, based on point, rolling and sliding contact mechanisms. A measurement and calibration process, derived from robot calibration applications, is proposed for the determination of joint accuracy and key error sources within each prototype. The calibration process is generic and allows for the direct comparison of joint characteristics.

The final joint prototype, based on a fluid contact mechanism, is covered in Chapter 4. High pressure air is injected into the cavity between the ball and socket to produce a low friction, high accuracy contact mechanism. This fluid contact joint is measured and calibrated in the same fashion as for the three other prototypes and the relative merits of each joint discussed. Joint stiffness is determined using a tensile tester and related to the three stiffness regimes inherent in the fluid contact joint: direct contact between the ball and socket; stiffness of the fluid gap; and stiffness of the magnet preload.

Chapter 5 validates the calibration algorithms developed in Chapter 3 by extending the modeling framework to include multi-axis robotic manipulators. Using the ABB IRB6400R robot as a test case, calibration models are developed and found to produce similar results to existing models implemented in the robot controller. Genetic Programming is used to improve robot accuracy through the implementation of additional physically based models. Finally, the techniques developed for robot manipulators are extended to include the joint prototypes, with the goal of reaching a maximum calibrated accuracy on the order of several micrometers.

Chapter 2

DESIGN PROCESS

2.1 Overview

The design process for the spherical joints and the test rig is based on a five step process.

1. Requirements – determine the key functional requirements and arrange these into a hierarchy of key specifications with underlying sub-specifications.
2. Strategies – develop basic sketches and justify with first order calculations.
3. Concepts – create solid models and ways to realize the chosen strategies.
4. Modules – develop the detailed design on the chosen concepts and define sub-assemblies.
5. Manufacture – create the required parts and assemble the final product.

The functional requirements are derived from the literature survey, refer to Chapter 1.5. These categories form the basis for the design and evaluation of appropriate joint prototypes. The strategy phase represents the initial brainstorming component of the design process, wherein the key functional requirements are used to develop basic ideas which are sketched and compared using analysis tables developed to facilitate the subsequent ranking of ideas. The concept phase expands the key functional requirements investigated in the Strategy phase and develops functional requirement sub-components with the goal of creating a set of viable models. The final set of concept models is compared to a baseline model and several of the best candidates chosen for continued analysis. The Module phase implements the chosen concept models as physical prototypes.

Final joint designs are chosen based on a ball and socket configuration, wherein the ball is seated in a hemispherical socket and preloaded by magnets. Three prototypes are implemented based on varying contact mechanisms between the ball and the socket: point, rolling and sliding.

2.2 Joint Design

2.2.1 Strategy Phase

The basic design sketches presented in Figure 2.1 through Figure 2.12 present various strategies based on the function requirements; covering the spectrum from existing technologies, based on the universal joint; and extending to newer concepts such as flexure joints and linkage mechanisms.

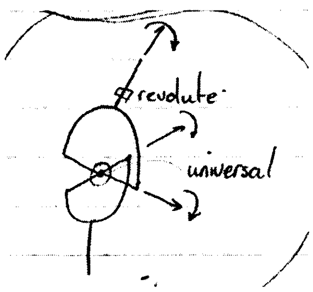

Figure 2.1 Modified universal joint

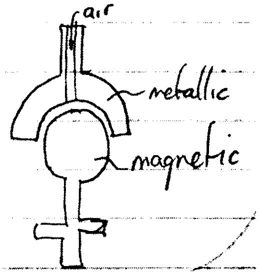

Figure 2.2 Magnetic air bearing

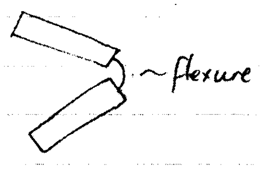

Figure 2.3 Flexure joint

The modified universal joint represents the simplest variation on the standard universal joint and implements an additional revolute bearing at one of the output shafts. This provides for a high stiffness joint but does decrease the accuracy due to misalignment of the revolute bearing axis with the universal joint axis. To minimize this, the magnetic air bearing implements a ball and socket joint with all axes coincident at the center of the ball. It extends the flat pad bearing design by considering a hemispherical socket with a single orifice at the apex. Air is fed in through the shaft to provide the necessary air film and the ball is magnetized and the socket is ferromagnetic to provide the required preload. However, separation is an issue, which is addressed by the flexure joint which takes an alternate approach by replacing revolute joints with flexible members, as is common in micro-electro-mechanical-system (MEMS) devices. While effective at the micrometer scale, these joints may not provide the range of motion and robustness required at the macro scale.

The slot and ball joint is a variant of the ball and socket design wherein the spherical ball is housed in a hemispherical socket. The preload is provided by a slotted retainer cup, which can rotate about the annular bearing. This design provides the requisite range of motion; however there exist singularities when the joint motion is perpendicular to the slot direction. Instead of implementing a rigid preload device, the spring preload design provides the preload using several flexible springs attached from the socket edges to the ball apex. This provides a singularity free workspace, however stiffness varies at the extremities of the workspace as the spring force becomes large, resulting in variable dynamic performance throughout the joint workspace.

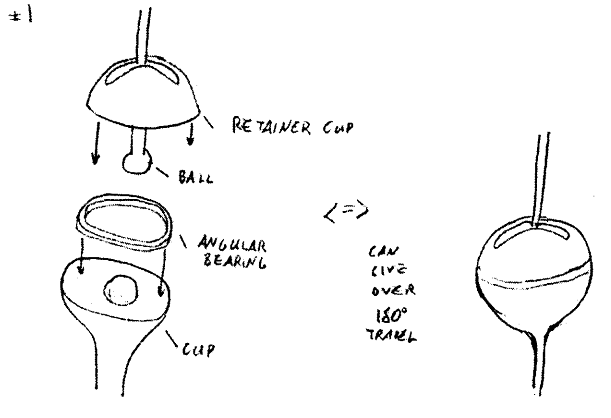
±1
RETAINER CUP
BALL
ANGULAR BEARING
CUP
<=>
CAN GIVE OVER 180° TRAVEL

Figure 2.4 Slot and ball

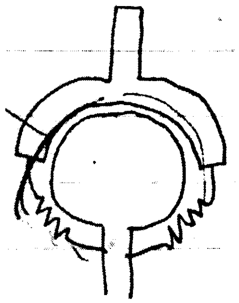

Figure 2.5 Spring preload

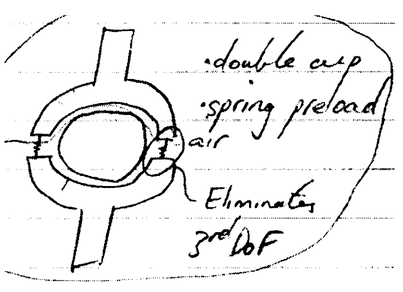
•double cup
•spring preload
air
Eliminates
3rd DoF

Figure 2.6 Double cup

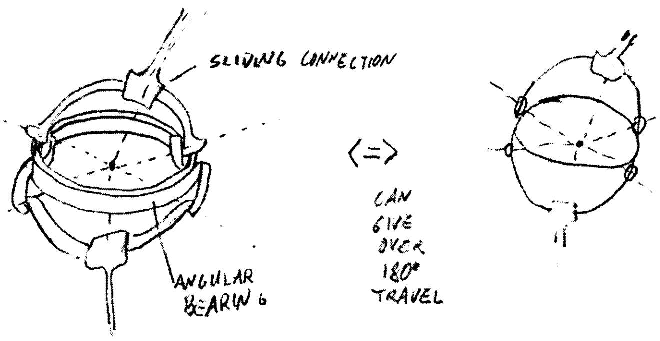
SLIDING CONNECTION
ANGULAR BEARING
<=>
CAN GIVE OVER 180° TRAVEL

Figure 2.7 Sliding arm universal joint

The double cup spring preload seeks to improve this performance degradation by implementing two sockets connected by shorter springs, with a spherical ball riding freely in between. This design, however, does not provide the required amount of travel to achieve a workspace of 180°. The sliding arm universal joint provides more than the required travel by mounting two identical sliding mechanisms on either side of an annular bearing.

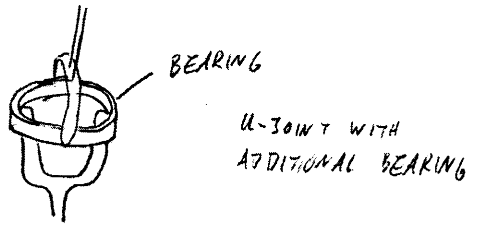
BEARING
U-JOINT WITH
ADDITIONAL BEARING

Figure 2.8 Modified universal joint

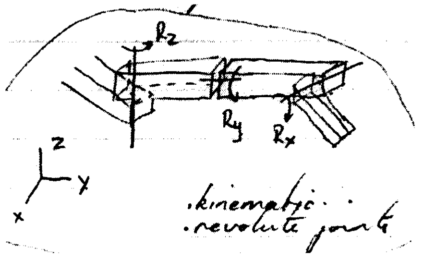
R_z
R_y
R_x
z
y
x
.kinematic
.revolute joint

Figure 2.9 Kinematic chain

The second modified universal joint uses a large annular bearing at the center of the joint, instead of a revolute bearing at one of the shafts, to achieve the third degree of freedom. The kinematic chain joint links three revolute joints mounted orthogonally to achieve three degrees of freedom; unfortunately this design is affected by multiple singularities in the workspace.

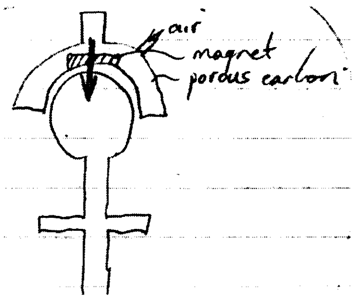
air
magnet
porous carbon

Figure 2.10 Porous carbon air

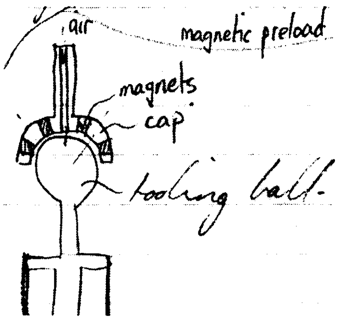
air
magnetic preload
magnets
cap
tooling ball

Figure 2.11 Magnetic cup

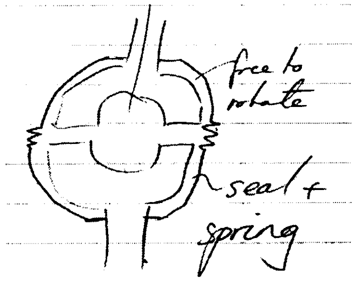
free to rotate
seal + spring

Figure 2.12 Sealed spring

The porous carbon air joint provides a variation to the single orifice ball and socket design by allowing the inlet pressurized air to enter through a porous carbon socket. This provides a more homogeneous air transfer mechanism, however the robustness of the porous carbon compared to steel or aluminum must be established. The magnetic cup is a variation of the magnetic ball design, wherein the socket is manufactured out of a non-ferromagnetic material and then populated with magnets. The inlet air may be supplied through a single orifice at the joint shaft or through multiple orifices arranged about the circumference of the socket. The sealed spring double socket design attempts to rectify the variable dynamic performance problems associated with the standard double cup design by allowing the springs to freely rotate with the joint motion, while providing a preload force to prevent separation. Additionally, the spring enclosure can be combined with the seal to satisfy the sealing functional requirement.

TABLE 2.1 Joint strategy table

Functional Categories	Design Parameters	Analysis	References	Risks	Counter Measures
Spherical motion	3DOF	3 Intersecting axes	Medical, Automotive	Separation during collision	Leash
	2+1DOF	2 Intersecting axes	Robotics	Kinematic inaccuracy, backlash	Improved models, apply preload
	1+1+1DOF	1 intersecting axis	Serial robotics	Singularities	Configuration
Contact Type	Point	Contact mechanics	Hertz	Wear, friction	Coating, rolling
	Rolling	Dynamics	Bearings	Wear, friction	Coating
	Sliding	Contact mechanics	Statics	Wear, friction	Lubrication
	Fluid	Fluid dynamics	Aerostatic bearings	Accuracy of film	Manufacturing process
Preload	Implicit mechanical	Material mechanics	Statics	Fatigue, wear	Material strength
	External force	Forces and moments	Statics	Separation	Tether

The strategy sketches have been classified into various categories and key design parameters extracted; the results are shown in Table 2.1. The spherical motion function requirement can be decomposed into the three kinematic chain alternatives; 1+1+1DOF as commonly found in robotics applications; 2+1DOF as typified by the modified universal joint; and 3DOF as found in rod ends and other spherical mechanisms. The contact type can be divided into four key mechanisms; point, as found in static kinematic couplings for coordinate measurement machines; rolling, such as rod end or spherical bearings; sliding, such as the teflon coating used for the delta robot joints; and fluid such as aerostatic or hydrostatic bearings. Finally, the preload force can be applied by an external force such as a spring or a magnet, or by an implicit mechanism that is integral to the joint design, such as a mechanical retainer.

2.2.2 Concept Phase

The strategy phase presented an array of idea sketches and distilled the key characteristics into a design parameter chart. The concept phase considers each design parameter of the strategy table and expands and evaluates suitable alternatives. The spherical motion concept table (Table 2.2) and concept tree (Figure 2.13) expand the three key motion mechanisms and evaluate each sub component in the same fashion as with the strategy phase.

TABLE 2.2 Spherical motion concepts

Functional Categories	Design Parameters	Analysis	References	Risks	Counter Measures
3DOF	Shoulder	Sliding friction	Powell	Separation during collision	Tether
	Kinematic	Hertz contact	Measurement	Friction	Coating, rolling elements
	Flexure	Beam bending	Timoshenko	Failure	Lifetime prediction
	Spherical mechanical	Sliding friction	Pat pend: 20010002964	Complexity	Simplify
2+1DOF	Universal + revolute	Joint kinematics	INA	Kinematic inaccuracy	Improved models
	Hookes	Joint kinematics	INA	Kinematic inaccuracy	Improved models
	Slot and revolute	Bearing yield stress during use	Patent: 6,234,703	Singular position when axes aligned	Design platform to ensure that axes will never align
1+1+1DOF	Revolute chain	Robotics	Denavit-Hartenberg	Singularity	Design constraints

The contact-type concept charts, detailed in Table 2.3, expand upon the four original contact mechanisms of point, rolling, sliding and fluid contact. The point and rolling mechanisms are similar ideas comprising three small spheres mounted in the socket, supporting a larger ball kinematically as described by Hertz deformation theory (kinematic). The sliding surface ideas comprise a relative motion of flat surfaces as well as a sliding between a spherical ball and a hemispherical cavity (shoulder). The fluid film category presents air, oil and gas as alternatives, with air being the most viable due to the requirements of safety and sealing.

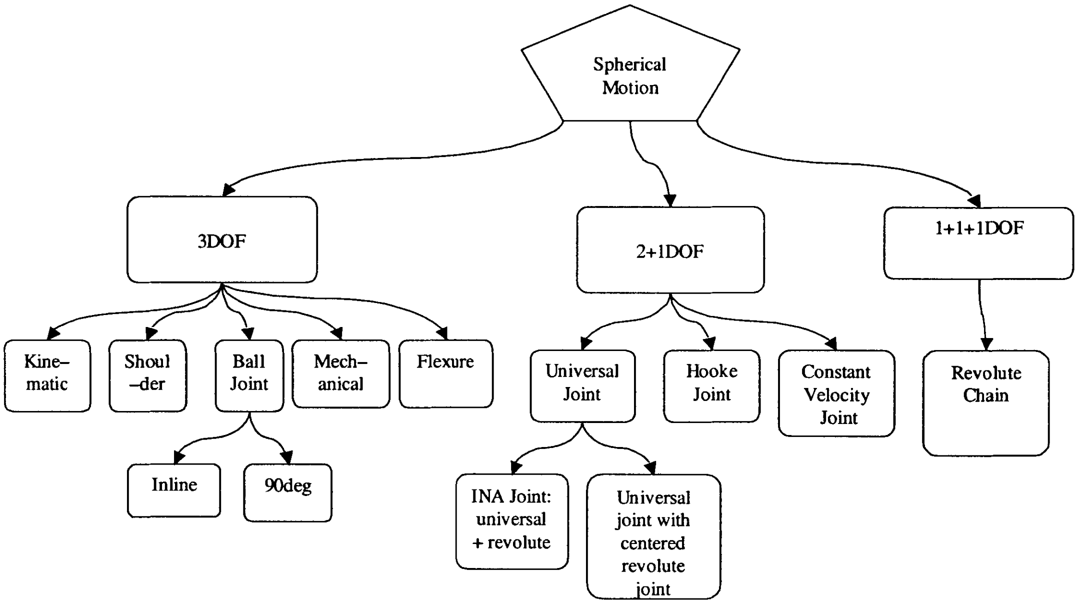
Spherical Motion
3DOF
2+1DOF
1+1+1DOF
Kine–matic
Shoul–der
Ball Joint
Mech–anical
Flexure
Inline
90deg
Universal Joint
Hooke Joint
Constant Velocity Joint
Revolute Chain
INA Joint: universal + revolute
Universal joint with centered revolute joint

Figure 2.13 Spherical motion concept tree

TABLE 2.3 Contact type concepts

Functional Categories	Design Process (Ideas)	Analysis	References	Risks	Counter Measures
Point	Ball on ball	Hertz contact	Hertz	Wear, friction, deformation	Coating
	Ball on groove	Kinematic Coupling	Slocum	Wear, friction	Coating
Rolling	Ball on ball	Hertz contact	Hertz	Deformation	Coating
	Ball on groove	Kinematic Coupling	Slocum	Wear, friction	Coating
Sliding	Ball on hemisphere	Hertz contact	Hertz	Friction	Lubrication
	Flat on flat	Statics	Popov	Friction	Lubrication
Fluid	Air	Fluid Flow	Navier Stokes	Use in dirty environments? Input and output of air	Seal
	Oil	Hydro-dynamics	Navier Stokes	Use in clean environment?	Seal
	Gas	Fluid Flow	Navier Stokes	Safety?	Seal

The preload concepts described in Table 2.4 expand the initial two strategy components of implicit mechanical and external force. The implicit mechanical coupling is an integral part of the joint design and is likely to be subject to deformation and yield considerations as described by structural mechanics analysis. The external force mechanisms may be supplied by springs, as with the delta robot; gravity which is commonly used for large coordinate measurement machines mounted on air bearings; vacuum as is typically used for small flat pad air bearings; or magnets where the magnetic field is used to provide an attractive force.

TABLE 2.4 Preload concepts

Functional Categories	Design Parameters	Analysis	References	Risks	Counter Measures
Implicit Mechanical	Mechanical connection	Material stresses and strains	Structural mechanics	Failure	Lifetime prediction
External force	Magnet	Magnet theory Permanent/ electromagnet	Magnetic theory	Separation due to motion or collision.	Tether
	Spring	F=kx	Linear elastic mechanics	Change in stiffness dependent on position, spring constricts motion	Mount spring along joint Z axis
	Vacuum	Fluid flow	New Way	Insufficient force	Larger surface
	Tether	Mechanical constraint	Statics	Constricts motion	Integrate into design
	Gravity	F=mg	Newton	Insufficient force	Combination

The three concept tables are combined to create a set of concept models, as described in Table 2.5. The spherical motion is restricted to three intersecting axes as the other two options (1+1+1DOF and 2+1DOF) result in kinematic inaccuracy. Each contact mechanism (point, rolling, sliding and fluid) is represented and both implicit and external forces are considered.

TABLE 2.5 Joint design concepts

Concept	Diagram	Description
Slot and Revolute	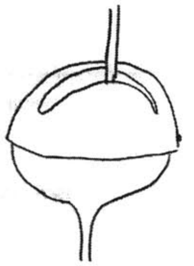	A traditional shoulder joint design flavor, using an angular contact bearing and a separate cap to achieve greater working range and load capacity. Preload achieved by constraining bearing races; inner race to bottom, outer race to cap.
Magnet pre-loaded friction contact shoulder joint	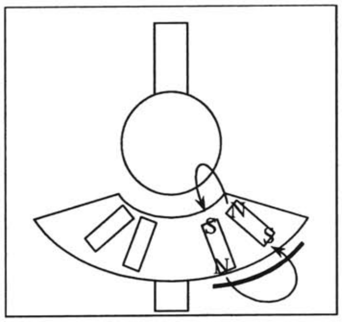 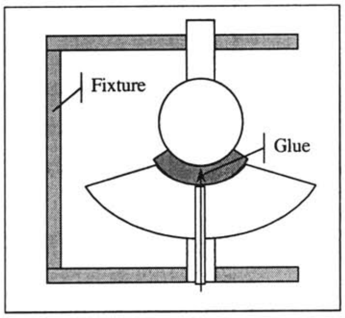	The ball is a standard tooling ball. The hemi–spherical socket cavity is machined by a spherical end mill. The magnets are placed around the socket in pairs such that the flux exits one magnet passes through the ball, enters the other and makes the return path via a steel plate on the back of the socket. The friction joint is achieved by mounting the ball and socket in a fixture that defines the separation of the two components. A low–friction glue is injected into the cavity while the two elements remain in the fixture and allowed to dry. The ball must be coated with a substance to ensure the glue dries only to the socket.
Magnet pre-loaded air bearing shoulder joint	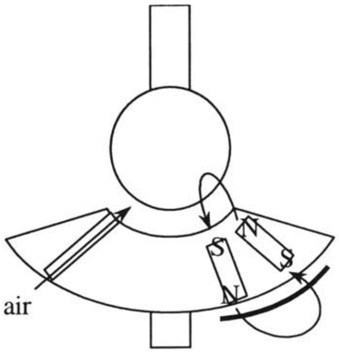	Using the same components as the magnetic preloaded friction joint, air is used to form the interface between the ball and socket. Micro-nozzles are drilled through the socket, or the socket is made from porous carbon, in order to introduce air into the ball-socket interface. Possibility for self-cleaning. Must have precise ball and cap and large preload force to prevent separation. Ensure even spread of air and magnets and analyze chance of instability and chatter.

Spring pre-loaded friction/air contact shoulder joint	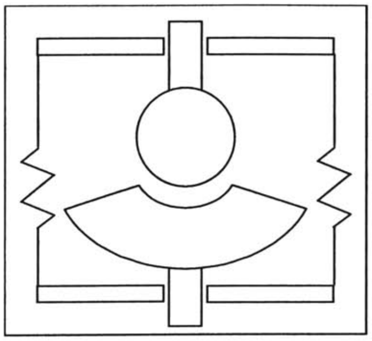	The same socket and ball components are used, however the preload is achieved by means of a spring mounted between the socket and the ball structures, similar to *[Hvittfeldt et al, 2002]*. The spring housing on the ball side must be allowed to rotate in order to achieve the third degree of freedom. The spring can be mounted directly to the socket or a similar housing can be used for the socket side. Analyze the preload force and consider extreme cases where one side is limp and the other tightened.
Dual socket, single ball	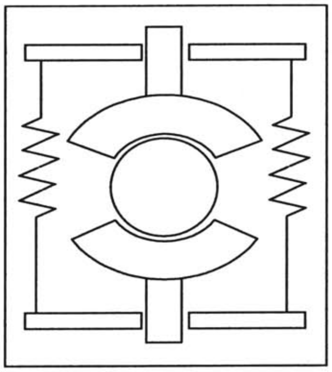	Two sockets are machined using a spherical end mill. A ball bearing is used in the center to separate the sockets. The double socket design allows for modular construction. Preload can consist of springs or magnets; contact can consist of air or friction. Must machine three precision surfaces (2 sockets, 1 ball). Ensure that the socket, in extreme positions, does not catch the springs. Consider non-linearity of springs at extreme positions.
Magnet pre-loaded friction kinematic socket and ball	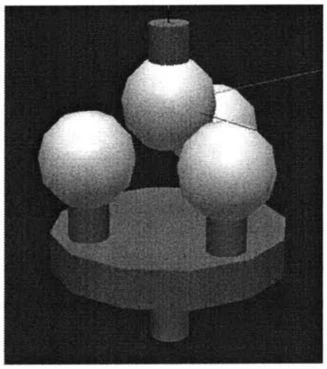	Three balls form the socket. They are each mounted on magnets such that each magnet is aligned in the same direction. This creates a flux path that is strongest at the apex of the three spheres - the magnets should be mounted on a steel plate to maximize the magnetic field. The ball component is a larger ball bearing that is held in place by the magnetic field. Analyze effect of dirt on the friction between the balls and the separation force from one of the three balls. Investigate effect of relative ball sizes and locations. Use machined surfaces with larger Hertzian contact area instead of balls to increase the load-bearing surface and allow improved lubrication.

From the set of six concept models, three are chosen: shoulder; kinematic; and slot and revolute. These are compared to the INA modified universal joint currently used for the ABB Tau robot prototype (Table 2.6). The shoulder joint utilizes magnets for preload and has the potential to implement either the surface or fluid contact mechanisms. The kinematic joint also implements magnetic preload and could illustrate the point or rolling contact mechanisms.

TABLE 2.6 Concept evaluation chart

Functional Requirement	**Specification**	**Baseline**	**Strategy 1**	**Strategy 2**	**Strategy 3**
		INA	Shoulder	Kinematic	Slot+revolute
Safety	No separation	0	–	–	+
Accuracy	Very high (low μm)	0	+	++	+
Workspace	>135deg	0	0	0	0
Stiffness	High (>10N/μm)	0	+	+	+
Robustness	Robust	0	–	–	0
Lubrication	low/no lubrication	0	+	+	0
Weight	Lightweight	0	+	+	0
Temperature	Low effects	0	0	+	–
Maintenance	Low/no maintenance	0	0	0	0
Modular	Low part count	0	+	+	0
Scaleable	reason	0	+	+	0
Singularities	None	0	0	0	–
Restrictions	None	0	0	0	–
Load capacity	Application defined	0	0	0	0
Preload	No separation	0	0	0	0
motion	Open	0	0	0	0
Modeling	existing	0	+	–	0
Energy usage	Minimize energy	0	–	0	0
Elegance	Consistent aesthetic	0	+	+	0
Materials	Minimize cost	0	0	0	0
Sealing	Full seal	0	0	0	0
Calibration	existing	0	+	+	+
		0	6+	7+	1+

2.2.3 Module Phase

The chosen concept models are further developed into three prototypes. The shoulder concept is implemented with the sliding surface contact mechanisms (Table 2.7); the kinematic concept is used to illustrate point and rolling contact mechanisms (Table 2.8). All three implementations use magnetic preload and the three intersecting axes spherical motion design.

TABLE 2.7 Sliding and fluid contact joint generations

Generation	Description
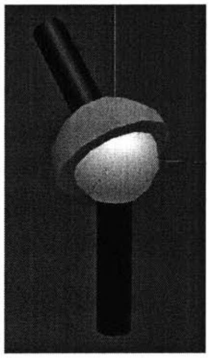	Original prototype comprising a tooling–ball like ball component mating with a hemispherical socket. The socket in turn has a hemispherical cup machined into the flat surface to accommodate the ball. The contact type could be air (either through porous socket materials or through micro–nozzles) or direct contact via a low friction material that could be injected into the gap (fixturing required). This design allows less than 180° of motion due to the hemispherical socket and large shaft size.
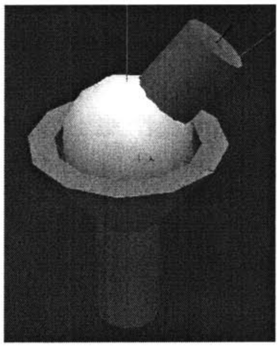	The socket is simply a turned cylinder forming a cone at the socket end. This eliminates the need for connection of the socket to the shaft; the shaft end can also be threaded in the same turning process. The mating surface is handled in a similar fashion to the original prototype.

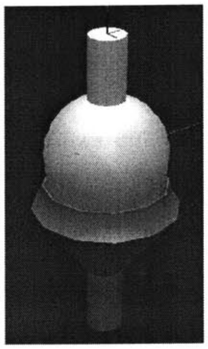	The design incorporates a larger ball to socket ratio and smaller shafts. This allows for more than 180° of motion in the Rx (roll) and Ry (pitch) directions. It remains to be determined how much material is required for the socket, with consideration for stiffness, strength, robustness and effect of preload.
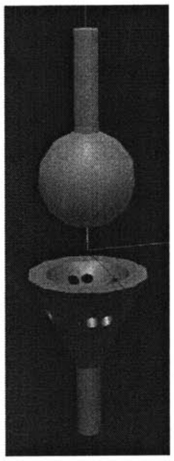	Simplified socket (probably chamfer off edges to provide more range of motion). Allows 180° in all directions with a 70° cup size and the preload magnet slots at 35°. These slots are drilled through 6mm holes that can accommodate permanent or electromagnets. Magnets are arranged in pairs to allow for increased magnetic force (two pole design) while maintaining a small footprint on the surface of the socket. The ball is a 50mm chrome steel ball — both ball and socket have a 12mm shaft glued, EDM or screwed into a periphery.
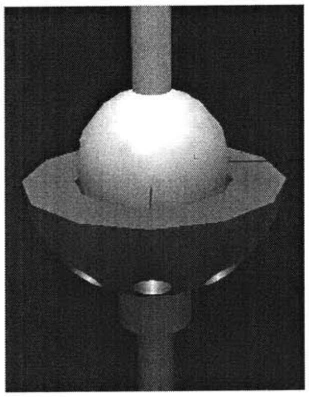	Simplified socket machined from diameter 60mm steel or aluminum cylindrical stock. 8 holes are drilled about the circumference of the socket at 45° to mount the magnets and provide the preload

TABLE 2.8 Point and rolling contact joint generations

Generation	Description
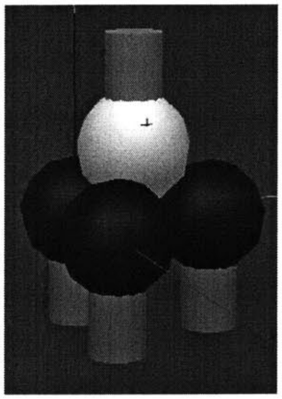	First concept model. Three tooling balls form the socket and each contact at a point with a larger tooling ball which connects to the second shaft. The magnets are connected to the base of each of the socket tooling balls.
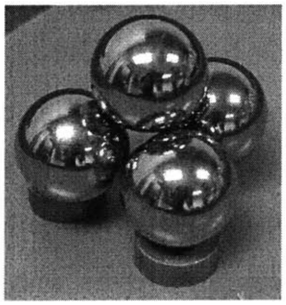	Basic proof of concept prototype. Ball bearings and loose magnets are arranged in the kinematic configuration and the preload force tested for various magnet orientations. Maximum force is achieved by aligning all magnets with the same polarity.
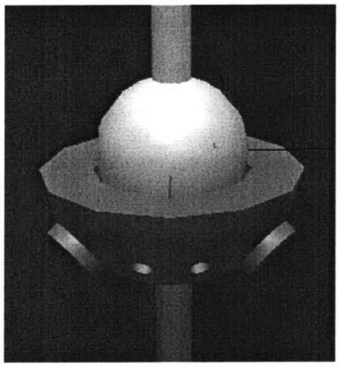	Basic solid model. The rolling contact prototype is shown with the ball transfers (solid ball bearing mounted on smaller ball bearings to allow free rotation of the ball within the enclosure) mounted about the socket. The smaller holes on the same annulus as the ball transfers are for the 6mm magnets. Additional holes are required about a second ring around the socket to provide a comparable preload force to the ball and socket prototypes.

2.2.4 Manufacture

Three prototypes have been implemented, each comprising an aluminum socket machined from 3.5" (90mm) stock and a 2" (50mm) diameter solid steel ball bearing. Separation between ball and socket is prevented by a magnetic preload force supplied by a ring of magnets about the circumference of the socket. Three primary contact mechanisms have been investigated: point, rolling and surface contact. The fourth mechanism, fluid contact, is presented in Chapter 4. The point contact prototype locates the ball kinematically upon three spheres embedded within the socket. Given minimal Hertz deformation due to the relatively low preload forces, the primary source of error for this type of joint is the accuracy of the ball. The main problem with this design is the friction inherent in the point contact region. The rolling contact prototype seeks to alleviate this friction problem by utilizing commercially available rolling ball-transfers mounted in the socket in place of the solid steel spheres. This dramatically reduces the friction but potentially increases the errors due to the additional influence of the ball transfer accuracy. The sliding contact prototype creates an accurate mounting surface through replication with a Teflon-laced epoxy. This provides a larger contact region to minimize contact stresses with reduced friction due to the Teflon contact surface. Despite the potential accuracy of such a joint, the friction is still significant. The assembly models and manufactured prototypes are detailed in Figure 2.14 through Figure 2.23.

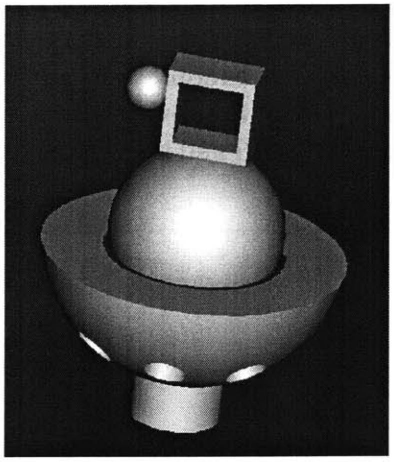

Figure 2.14 Sliding contact assembly model

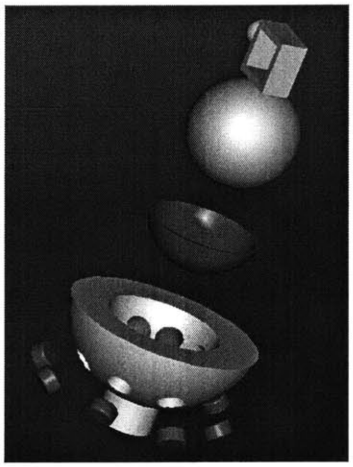

Figure 2.15 Sliding contact exploded model

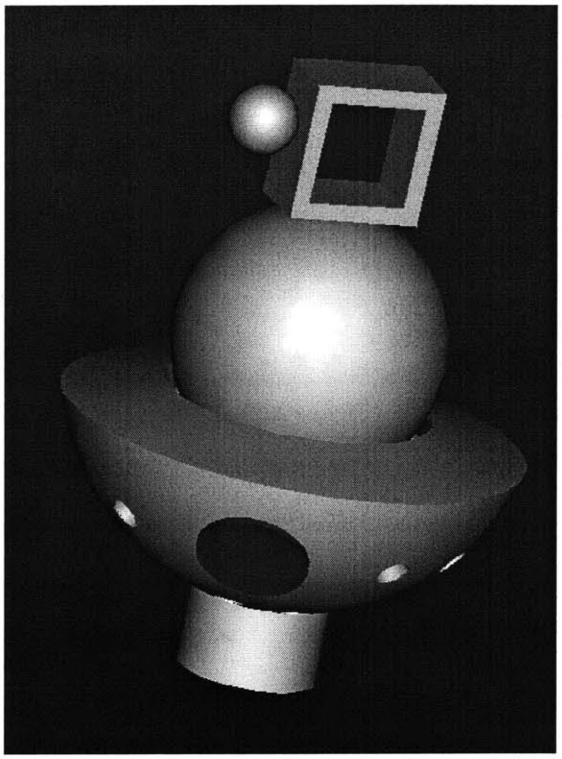

Figure 2.16 Rolling contact assembly model

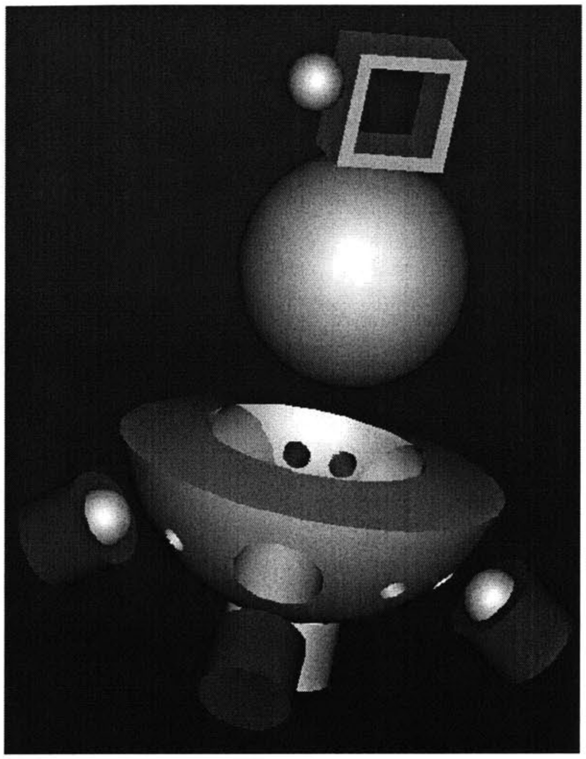

Figure 2.17 Rolling contact exploded model

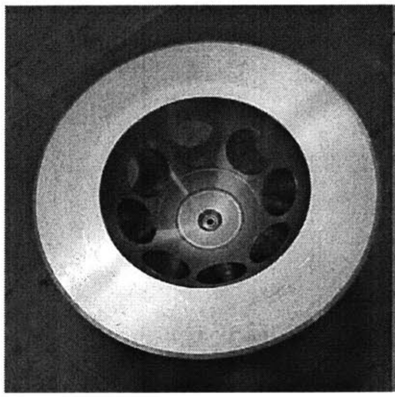

Figure 2.18 Sliding contact socket

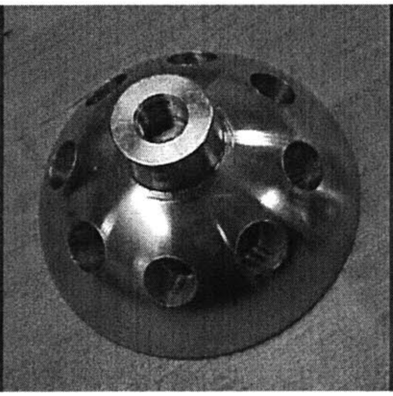

Figure 2.19 Sliding contact socket

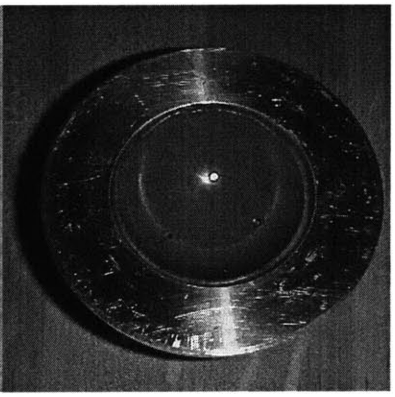

Figure 2.20 Sliding contact joint

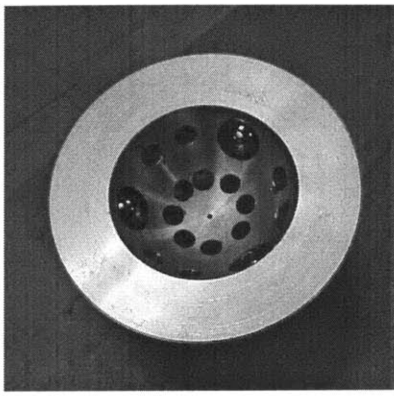

Figure 2.21 Point contact

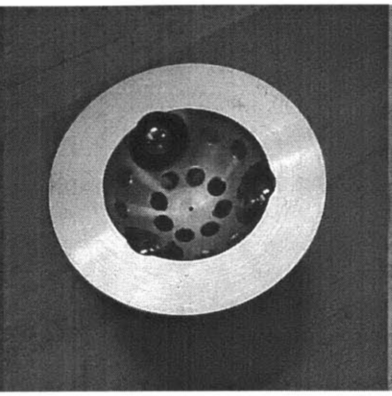

Figure 2.22 Rolling contact

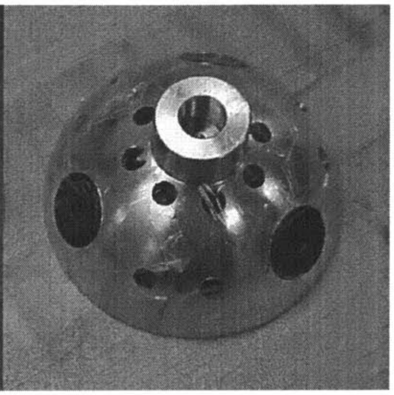

Figure 2.23 Rolling contact joint

Machining process

1. Cut 3.5" (90mm) stock to correct length
2. Fix in 3-jaw chuck
3. Turn face
4. Rough and fine turn outer surface
5. Drill center 1/16" (1.5mm) hole
6. Drill shaft 1/12" (2mm) hole
7. Remove from lathe and fasten on boss end
8. Face, rough and fine turn inner hole
9. Mount the face in an indexing chuck and set to desired angle (45° for shoulder, 21°/52° for kinematic). Mount in mill.
10. Tram in (with dial gauge or pen) to determine correct X-Y location for hole

11. Drill desired hole (½", 12mm for shoulder, ¼", 6mm for kinematic). Index to next angle and repeat.

Replication process

1. Glue the desired number of magnets into a cylinder.
2. Attach one disk of thickness 1/32" (0.75mm) to the end of each magnet cylinder.
3. Place several 1/16" (1.5mm) O-rings between the ball and socket. Mount the assembly in a mill. Determine the Z-axis of the assembly by tramming. Note the position of the assembly in the mill. Coat the ball with a release fluid (e.g. oil).
4. Insert the magnet cylinder and butt up against the ball with the plastic disk end. Glue the magnet cylinder in place with Loctite. The 1/32" (0.75mm) plastic spacer disk will ensure that the magnet cylinder sits 1/32" (0.75mm) above the surface of the socket.
5. Remove the ball, remove the 1/16" (1.5mm) O-rings and 1/32" (0.75mm) plastic spacers.
6. Replace the ball such that the position of the mill is at the same position as noted. The ball will therefore be 1/16" (1.5mm) from the socket in all places except for where the magnets are 1/32" (0.75mm) from the ball.
7. Inject the replication fluid through the small hole in the socket center into the 1/16" (1.5mm) cavity. Continue until the fluid fills the entire gap. Ensure no air pockets by injecting fluid slowly from the bottom of the socket and allowing fluid to overflow socket edge. Bubbles in the fluid will exit before the epoxy is able to set fully.

8. Hold the assembly together while the replication fluid dries, at which stage the ball can be removed (the release fluid will facilitate removal of the ball).

Process Notes

- Use of the 1/16" (1.5mm) spacers to set the initial ball-socket gap requires the subsequent separation of the assembly for removal of the spacers prior to replication. For the replicated joints, it may be possible to "eject" these spacers using a pressurized jet of air, however this may cause distortion in the gap.
- A jigless method is to drill several 1/32" (0.75mm) holes in the socket and insert a bolt, or threaded orifice mount, such that the cylinder extends 1/16" (1.5mm) into the socket. The ball can be butted against these cylinders, which act as the separators. The cylinders remain in place during replication. They are removed for the sliding contact joint, but remain in place for the fluid joint to supply the air, without requiring additional modifications. An issue may be the effect of having a small hole in the direct contact joint, such that the surface is inconsistent causing increased friction or errors in the motion of the joint.

2.3 Test Rig Design

The five step iterative design process is used to develop a prototype for the joint test rig. The functional requirements are the subset of the joint requirements pertaining to the accuracy and preload of the joint. The primary focus for the joint test rig is the determination of positional accuracy; additionally, repeatability, preload force and friction characteristics should be determined for each prototype.

2.3.1 Strategy Phase

The strategy sketches are presented in Figure 2.24 through Figure 2.26. The double ball bar is based on mechanisms of the same name *[Bryan, 1992]* that are used in coordinate measurement machine (CMM) calibration and allow measurement of linear displacement of the central ball bar axis. The joints allow accurate spherical motion for each end of the ball bar; one end is fixed to the CMM probe and the other end fixed to the table. The position of the upper joint as determined by the CMM is used to calibrate both joints. The universal mechanism actuates two of the joint's axes via semicircular rings mounted orthogonally on the CMM table. The third axis rotates the joint about its third axis. The actuated clamp is also intended to be mounted in a CMM and uses passive actuation via a flexible clamp to move the joint through its workspace.

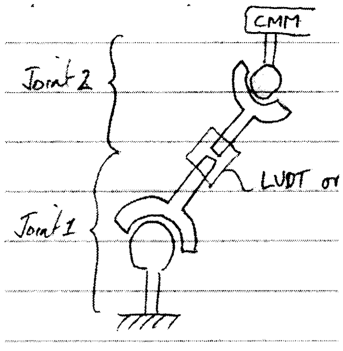

Figure 2.24 Double ball bar

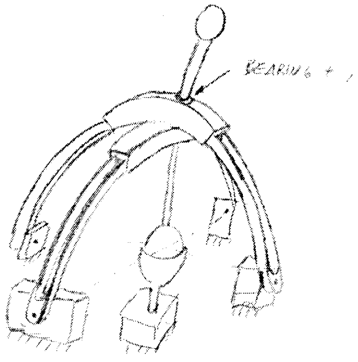

Figure 2.25 Universal mechanism

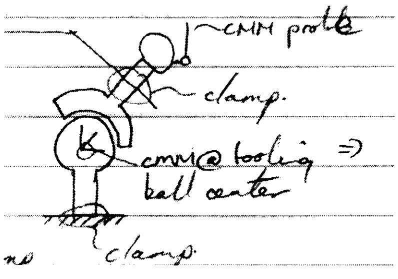

Figure 2.26 Actuated clamp

The three key functional requirements: spherical motion, contact type, and preload force and their relevant subcomponent design parameters are analyzed in the same fashion as with the joint prototypes as detailed in Table 2.9.

TABLE 2.9 Test rig strategies

Functional Categories	Design Parameters	Analysis	References	Risks	Counter Measures
Spherical motion	Accuracy	Measure position	Robotics	Inaccuracy of measurement system	High accuracy machine
	Repeatability	Measure position difference	Robotics	Replace to same position	Positioning fixture
	Range of travel	Measure angle	Inclinometers	What axis	Fix axes, measure both
Contact Type	Surface finish	Profile surface	Profilometry	Cost	Borrow machine
	Maintenance	Simulate duty cycles	Machinery testing	Unrealistic cycles	Ask customer
Preload	Weight	Weigh	Statics	Accuracy	High resolution scale
	Safety	Try to break/pull apart	Tensile testing	Accuracy	Sensitive load cell
	Stiffness	Push and pull	Tensile testing	Accuracy	Sensitive load cell

2.3.2 Concept Phase

The design parameters from the strategy chart are further expanded, analyzed for viability and summarized in Table 2.10. Detailed concepts are presented in Table 2.11 and the ranked prototypes are evaluated in Table 2.12.

TABLE 2.10 Test rig concepts

Functional Requirements	Design Parameters	Analysis	References	Risks	Counter Measures
Weight	Scale	$F=mg$	Statics	Accuracy	High resolution scales
Safety	Tensile tester	Strength test	Materials	Sensitivity	Access to machine
Stiffness	Separation	$F = kx$	Statics	Unrealistic cycles	Customer cycles
Maintenance	Long term	Lifetime	Manufacturin	Testing time	Accelerated testing
	Collision tests	Energy transfer	Dynamics	Unrealistic	Robot collisions
Accuracy	Calibration	$F(\theta,\varepsilon)–M(x,y,z)$	Shröer	Measure RxRyRz?	Inclinometer
Repeatability	Repeatability tests	ISO tests	ISO	Measure or fix RxRyRz	Flexure, Kinematic Coupling
Surface finish	Surface finish	Profilometer	Zygo	Shape unsuitable	Check
	CMM	$M(x,y,z)$	NIST	CMM Inaccuracy	Accurate CMM, symmetry
	Shape fitting	$F(r)– M(x,y,z)$	Modeling	How to interpret	Sphere model
	Double ball bar	$F(\theta,\varepsilon)–M(r)$	CMM	Separate joint parameters	Double joint model
Workspace	Inclinometer	θx, θy	Wyler	Angle	360° inclinometer
	Protractor	θx, θy	Metrology	Accuracy	How accurate does it need to be?

TABLE 2.11 Test rig concepts for accuracy measurement

Concept	Diagram	Description
Inclinometer based range of travel measurement	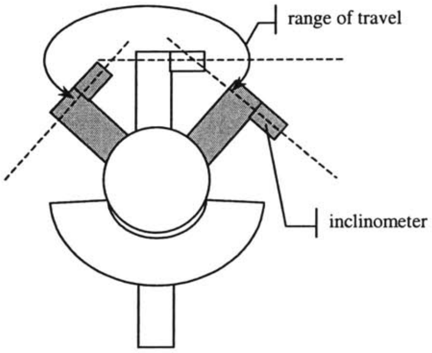	Attach an inclinometer to the upper shaft of the joint. Move the joint in a plane (1D inclinometer) and record the angular displacement of the joint. Use of a 2D inclinometer will allow the full working range of the joint to be determined.
Double joint ball bar	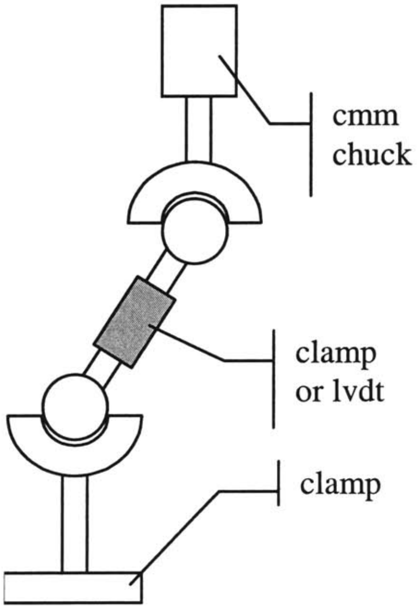	One joint is fixed to the CMM table, the other end is clamped to another joint. The end of the second joint sits in the CMM chuck. Movement of the CMM will result in fixed-radius rotations about the joint centers and enable calibration of the joint error parameters. To obtain an extra degree of freedom and hence utilize a greater measurement volume, an LVDT or linear track with encoder can be mounted between the bearing shafts instead of the clamp.
Surface finish	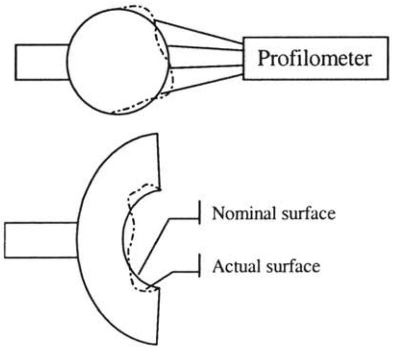	Mount the ball in a Zygo (or similar) profilometer and measure the accuracy of the ball surface. Repeat for the socket.

Relative motion of ball and socket	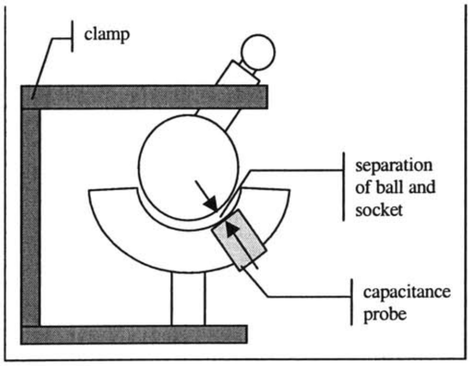 clamp separation of ball and socket capacitance probe	Capacitance probes measure separation between the probe and a metallic surface to sub-micron accuracy. Mount a capacitance probe in the socket and measure the distance to the ball. Move the ball around as per the CMM measurements and measure the variation of separation. This gives an indication as to the interface motion of the two components.
Repeatability	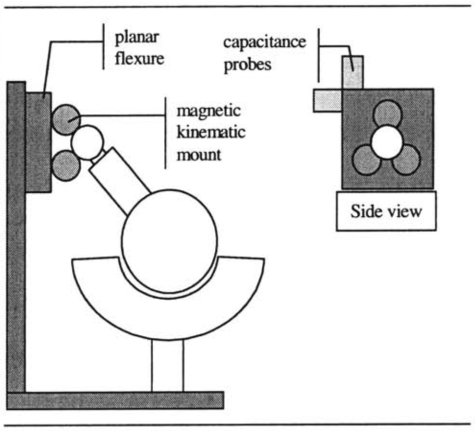 planar flexure capacitance probes magnetic kinematic mount Side view	The repeatability of the joint represents its ability to move to the same position with a given accuracy over a certain number of trials. A magnetic kinematic (constrain position but allow rotation) or KC (constrain all 6DOF) mount is mounted on a planar x-y flexure. The tooling ball on the end of the ball joint can then sit accurately at the apex of the kinematic mount. The kinematic mount can move in the x-y plane directions and capacitance probes can be used to measure the deflection. Any deviations in position due to inaccuracies of the joint cause the kinematic mount to move and hence the capacitance probes to record a positional deviation.

TABLE 2.12 Concept evaluation chart

Function	Strategy 1	Strategy 2	Strategy 3	Strategy 4	Strategy 5	Strategy 6	Strategy 7
	CMM	Double Ball bar	Surface finish	Relative motion	Repeat-ability	Tensile Tester	Inclino-meter
Safety	0	0	0	0	0	+	0
Accuracy	++	+	0	0	0	0	0
Repeatability	+	+	+	+	++	0	0
Travel	+	+	0	0	0	0	++
Stiffness	0	0	0	0	0	++	0
Robustness	0	0	0	0	0	+	0
Lubrication	0	0	+	+	0	0	0
Weight	0	0	0	0	0	0	0
Temperature	+	+	+	+	+	0	+
Maintenance	0	0	+	+	0	0	0
Singularities	0	0	0	0	0	0	0
Load capacity	0	0	0	0	0	+	0
Calibration	+	0	0	0	0	0	0
Total	6+	4+	4+	4+	3+	5+	3+

A spherical kinematic test rig is proposed for the measurement of the endpoint position of the joint shaft; the position data can then be used to fit a basic sphere shape (determine radius and center) and more advanced information such as joint center eccentricity and non-linear effects. A joint tensile tester is proposed for the preload and stiffness measurements for each joint. These machines are readily available (Instron, Stable Microsystems) and can be easily used with minimal modifications.

2.3.3 Module Phase

The spherical mechanism test rig evolution is detailed in Table 2.13.

TABLE 2.13 Test rig design generations

Generations	Description
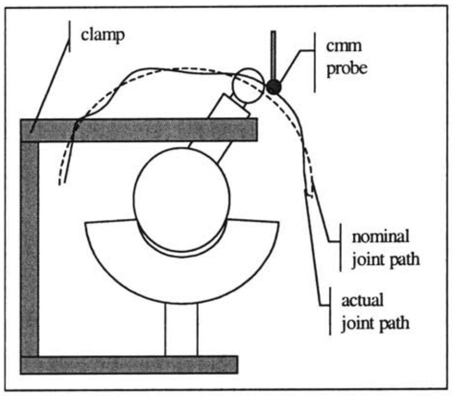 clamp cmm probe nominal joint path actual joint path	Fix the spherical joint in a CMM with a special clamp fixture. This fixture allows the joint to be moved throughout its working range but fixes that position while measurements are being taken. The CMM probe touches a tooling ball mounted at the other end of the shaft of the ball component. The path traced by the ball will approximate a sphere. Fitting this to a nominal sphere can give an indication as to the accuracy of the joint
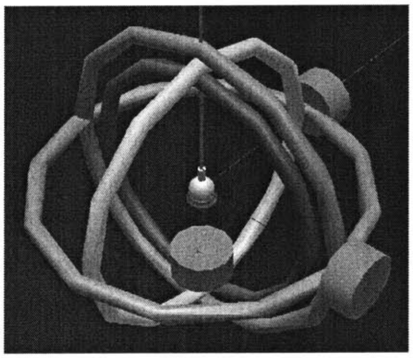	Fit the joint in a gimbal structure that provides the same RxRyRz motion as the joint. The large cylinders are motors and the tori rotate about each of the x-, y- and z-axes. The 3DOF joint is clamped in the center, the current design which features closed tori obstructs the motion.
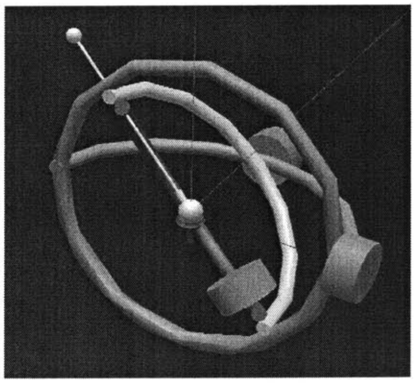	C-section torus configuration allows access to the joint for mounting in the CMM. Moving support of the Ry beam is necessary at the ends, the other two beams are supported by stationary (relative to the last beam) bearings at the extremities.

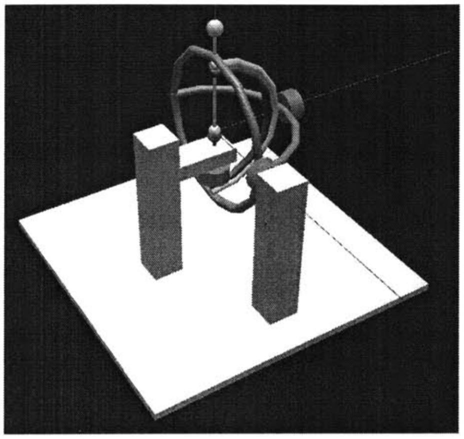	C-section torus mounted in CMM. The joint and test rig mount to columns which in turn mount directly on the CMM. The flexibility of each column and the corresponding deflection under the expected loads must be determined.
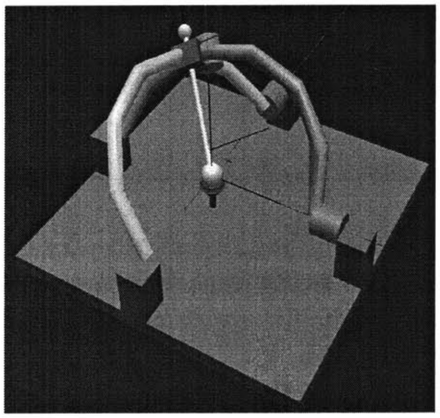	Alternative concept involving fixed Rx and Ry stages and an end effector mounted Rz. The advantage is that the Rx and Ry stages are fixed to base and the joint can be directly mounted to a platform or CMM table. The disadvantage is that parasitic motion in Rz occurs for Rx and Ry near 90°
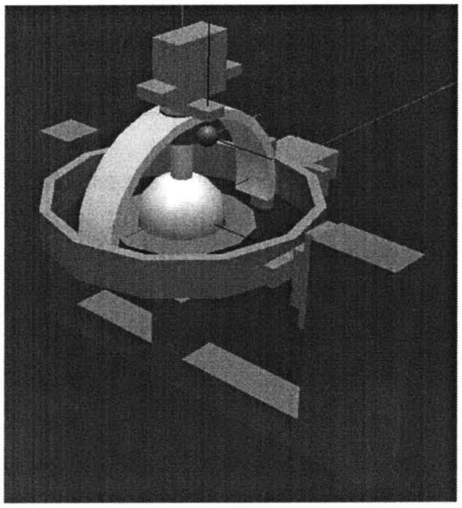	Improved working area by moving Rz motor to the top of the structure and measuring the tooling ball inside the structure.

2.3.4 Manufacture

The spherical kinematic test rig (Figure 2.27, Figure 2.28) allows the actuation of each of the spherical joint's degrees of freedom for the purpose of measurement in a coordinate measurement machine (CMM). It comprises three concentric rings that are actuated by radio-control servomotors: the x-axis motor is mounted on the base; the y-axis motor is mounted on the x-axis ring; and the z-axis motor is mounted on the y-axis ring. The test rig stiffness is designed to be significantly less than the joint stiffness in order to avoid deformation of the joint during measurements.

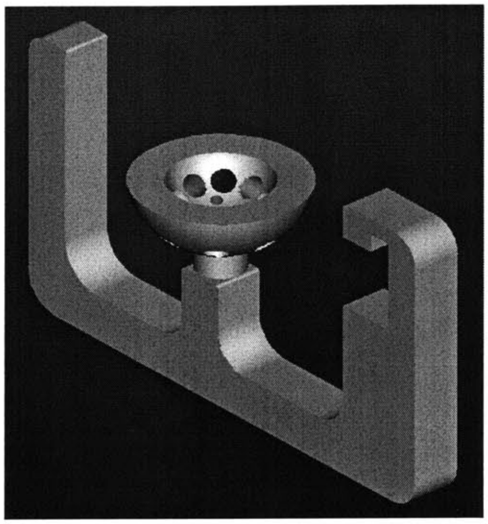

Figure 2.27 Test rig base

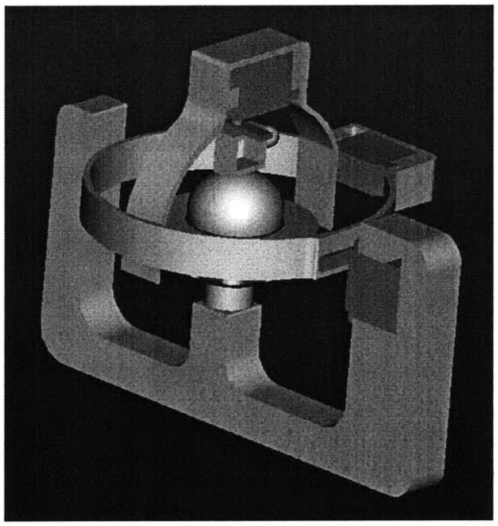

Figure 2.28 Test rig complete mechanism

The test rig is predominantly manufactured using the OMAX waterjet *[OMAX, 2002]*. The base, x-axis and y-axis rings are cut out of a single 1" (25mm) thick sheet Aluminum sheet as shown in Figure 2.29. Standard radio control servomotors are mounted in recessed pockets on each component and each successive axis mounted directly to the servo horn of the previous axis. The z-axis servo horn is connected to the joint via a velcro connection that acts as a breakaway joint, preventing relative motion of the z-axis motor and the ball, but allowing release in the case of a collision. A tooling ball is mounted on the joint shaft to allow measurements by the CMM probe. The test rig can be manually actuated with a radio control unit or automated via a commercially available micro controller. It is mounted in the CMM and then run through a set of approximately 30 poses, distributed evenly about the joint workspace (Figure 2.30 and Figure 2.31). For each pose, the tooling ball center is measured, and the set of joint poses and measured positions compiled for analysis.

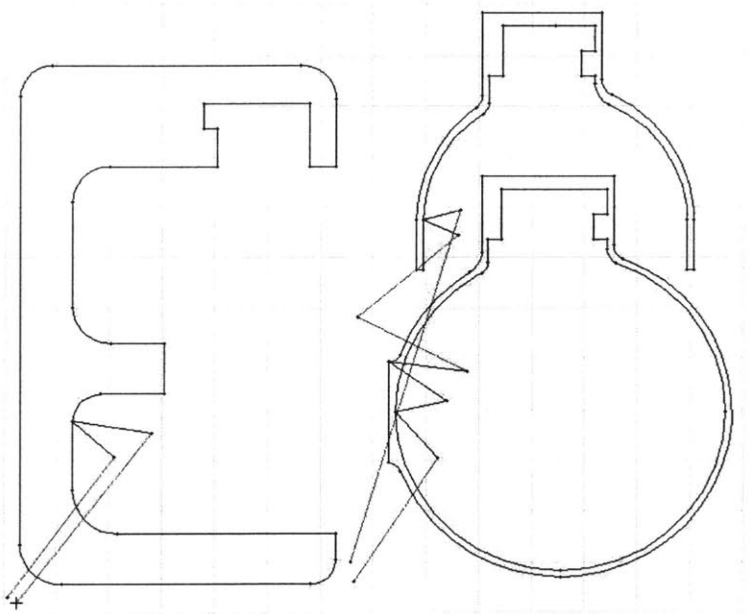

Figure 2.29 OMAX waterjet path.

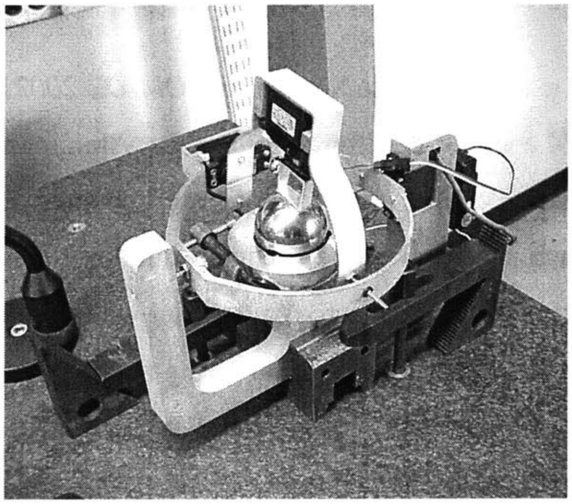

Figure 2.30 Spherical kinematic test rig

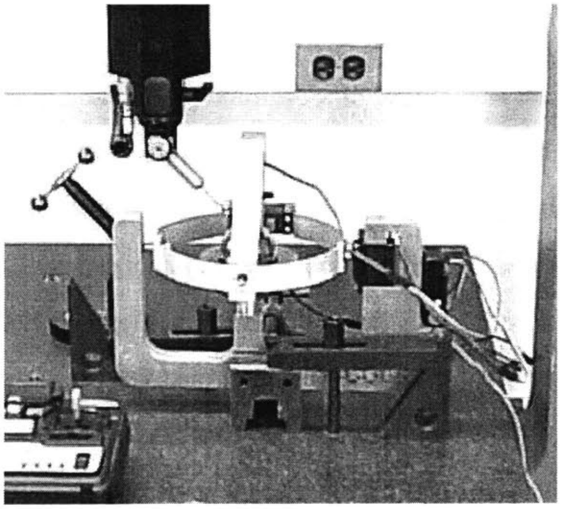

Figure 2.31 Test rig and CMM probe

2.4 Conclusion

A five step iterative design process is used to develop three joint prototypes and a test rig to measure the accuracy of each prototype. Additionally, a tensile testing machine is utilized to determine the preload force of each joint prototype. The individual stages of the process: Requirements; Strategy; Concept; and Module; are used to specify, brainstorm, refine and manufacture the prototypes. At each step evaluation tables are used to determine a set of viable alternatives and to allow comparison of the relative merits of each approach. The final prototypes developed should represent the optimal design for the given set of functional requirements.

Chapter 3

ANALYSIS AND MEASUREMENT

3.1 Overview

Spherical joints have been developed based on the ball and socket concept, wherein a spherical ball sits in a hemi-spherical cavity. Three designs are implemented; based on point, rolling and surface contact mechanisms. The point contact joint is implemented by kinematically mounting the ball on three smaller spheres embedded in the socket, as per ball bar mechanisms *[Bryan, 1992]*. The rolling contact joint uses ball-transfer components instead of fixed spheres to significantly reduce friction. Each ball-transfer comprises a large spherical bearing supported by many balls of smaller diameter, thus reducing the friction through rolling contact and supporting the applied load over many points of contact. The sliding contact joint implements a high accuracy, low-friction, replicated surface between the ball and socket, using a teflon-laced epoxy *[Slocum, 1992]*. Each joint design incorporates a magnetic preload wherein the socket is populated with various configurations of permanent magnets that attract the solid steel ball.

Each spherical joint prototype is tested using a spherical kinematic test rig that allows the independent actuation of each of the joints' degrees of freedom: roll (rotation about a nominal x-axis), pitch (y- axis rotation), and yaw (z-axis rotation). Each prototype is measured by affixing a tooling ball to a shaft attached to the ball and mounting the joint in the test rig, which itself is mounted in a coordinate measurement machine (CMM). The test rig actuates the joint to various positions in its working space and the CMM measures the position of the center of the tooling ball.

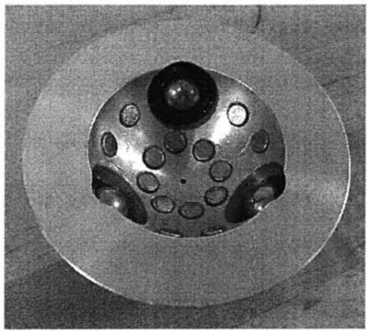

Figure 3.1 Rolling contact

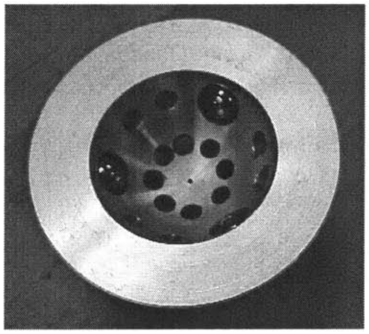

Figure 3.2 Point contact

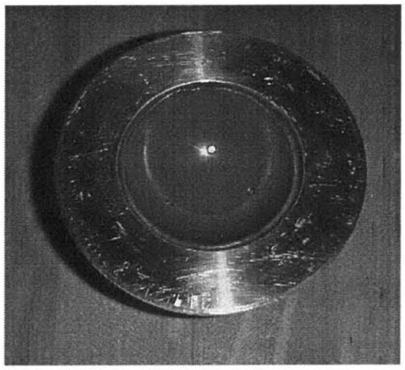

Figure 3.3 Sliding contact

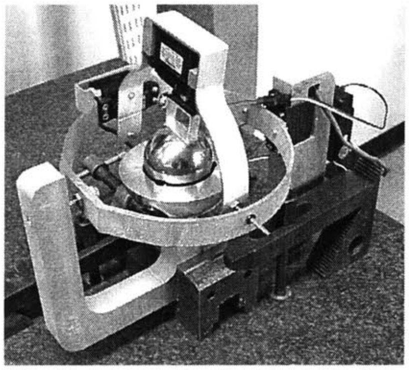

Figure 3.4 Test rig

Joint accuracy is characterized using a geometric sphere-fit algorithm to fit the measurement data to a standard sphere through the calculation of the best-fit sphere center and radius. The final (sphere-fit) error is the deviation of each measurement position from the best-fit radius. Additionally, a kinematic parameter estimation algorithm has been developed to characterize the individual error parameters within the joint, such as the eccentricity of the axes of rotation. The passive joint is treated as a three degree-of-freedom mechanism and the error parameters determined through a numerical Jacobian-based technique *[Bernhardt et al, 1993]*. As the joint prototypes have no angular feedback and the test rig is relatively inaccurate, joint angle positions are not accurately known and needed to be re-calculated for each measurement location. The calibration sequence involves the initial estimation of kinematic error parameters (based on the current joint angles) followed by the update of the joint angles (based on the updated error parameters and the measurement location). This “leap-frog” algorithm continues until both the error parameters and the joint angles converge; the final (calibrated) error is the difference between the predicted and the measured joint position.

Measurements of the joint prototypes indicate a best case sphere-fit error of 12μm and a calibrated error of 8μm. The error of the CMM is estimated to be 2μm.

3.2 Preload Analysis

3.2.1 Magnet Characterization

The preload for all prototype designs is based on a single ring of magnet pairs, arranged in an altering north-south configuration to maximize the resultant preload force. In order to predict the preload force for a given magnet configuration, each magnet is considered to be a point force source and the preload determined through a simple force balance. A more detailed approach would involve modeling the magnetic properties and developing a model for the socket based on the inherent magnetic properties.

3.2.2 Sliding and Fluid Contact Prototypes

The preload required to hold the ball and socket together can be initially calculated through a basic static force balancing analysis. Consider an applied force (F_a) acting at an angle theta (θ), resisted by a preload force (F_p) acting at an angle gamma (γ). The socket angle alpha (α) defines the size of the socket and constrains the applied and preload angles as shown in Figure 3.5.

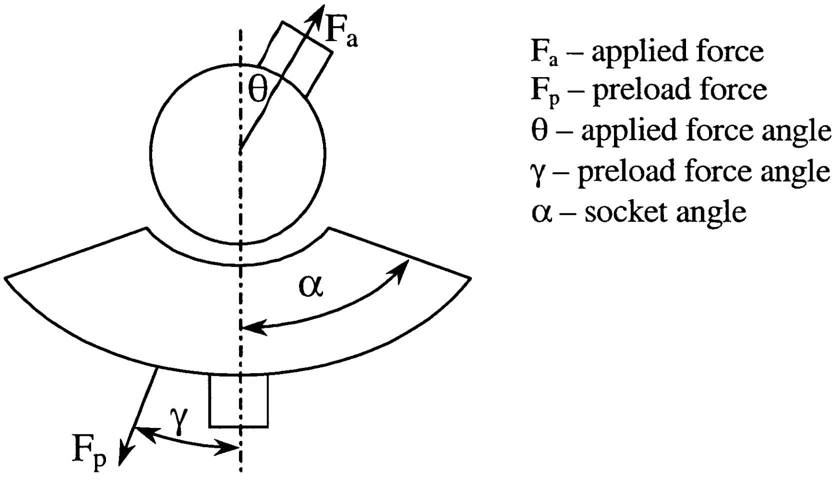
F_a
θ
α
γ
F_p
F_a – applied force
F_p – preload force
θ – applied force angle
γ – preload force angle
α – socket angle

Figure 3.5 Generic spherical joint schematic

For highly conforming surfaces, the reaction force (F_n) will be a distribution along the length of the contact surface. To simplify the analysis, the reaction force will be considered to act at a point, defined by the angle phi (ϕ) from the vertical (refer to Figure 3.6).

The allowable applied force for a given preload is determined for two configurations: ball fixed and socket fixed. The ball fixed configuration considers mounting cases where the ball is fixed to the robot actuator and the socket moves about the ball; the opposite applies for the socket fixed case. The ball down configuration results in a maximum applied force that is equal to the preload force as both are always acting in the same direction. The socket fixed configuration, however, results in a maximum applied force that depends on the ball angle as described in Figure 3.6.

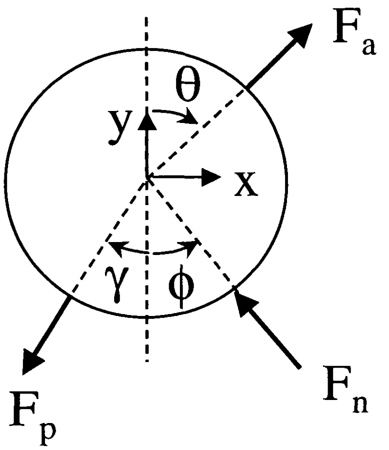

Force and moment equilibrium :

$$\sum F_x = 0 = F_a \sin\theta - F_n \sin\phi$$

$$\sum F_y = 0 = F_a \cos\theta - n F_p \cos\gamma + F_n \cos\phi$$

$$\sum M_z = 0$$

Rearrange :

$$F_n = F_a \frac{\sin\theta}{\sin\phi}$$

Substitute :

$$F_a \cos\theta - n F_p \cos\gamma + F_a \frac{\sin\theta}{\sin\phi} \cos\phi$$

$$F_a = \frac{n F_p \cos\gamma}{\cos\theta + \sin\theta \cot\phi}$$

Figure 3.6 Force balance for socket fixed mounting

The resulting equations for determining the maximum applied force are shown in Figure 3.7 and Figure 3.8; note that the ball-down configuration is independent of the joint angle and that the socket-down equation reduces to the ball-down equation when the joint angle is zero.

Both preload relationships are shown in normalized form in Figure 3.9; the ball fixed configuration results in a constant preload while the socket fixed configuration results in a degradation of preload force of 50% throughout the workspace of the ball. Clearly the ball fixed configuration is optimal and this should be chosen for mounting to the robot structure.

$$F_A = \frac{\sum F_P \cos\gamma}{\cos\theta + \sin\theta \cot\phi}$$

Figure 3.7 Socket fixed configuration

$$F_A = \sum F_P \cos\gamma$$

Figure 3.8 Ball fixed configuration

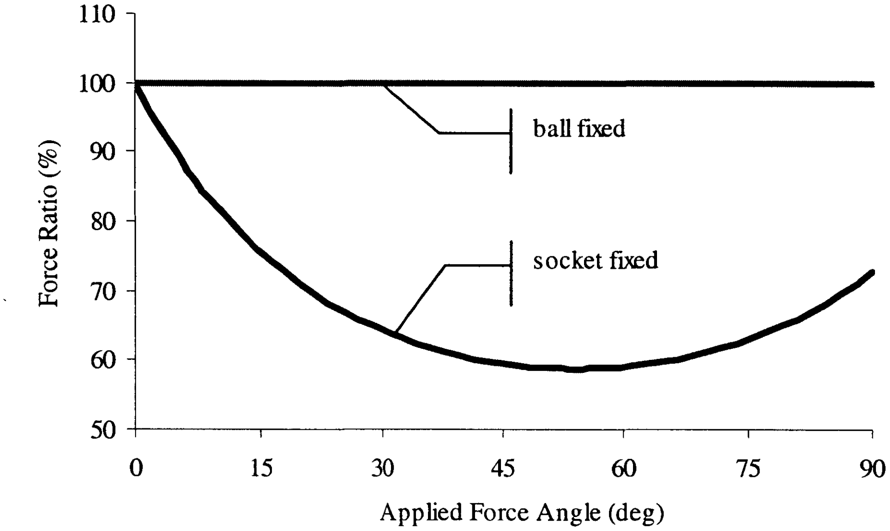

Figure 3.9 Preload characteristics for sliding and fluid contact joints

The maximum allowable force and the geometric and magnet placements are determined by an optimization process. The force balancing equations are used to determine the allowable applied force for difference ball angles, given a certain cup size and magnet placement. The minimum allowable force for the entire ball angle range (for a given cup size and magnet configuration) represents the maximum allowable force for that configuration. The maximum allowable force is determined for different magnet varieties and varying cup sizes and magnet placements. Magnet placement is maximized by placing as many magnets as possible about the circumference drawn by the preload angle as shown in Table 3.1.

TABLE 3.1 Preload optimization for sliding contact joint

Socket Angle (deg)	Preload Force (N)	Preload Angle (deg)	Magnet Diam (mm)	Magnet Thickness (mm)	Cost ($)	Area Ratio (%)	Socket Pressure (psi)
72	83.7	54	12	6	8	29.4	3.5
54	86.4	36	12	6	6	29.4	4.8
63	86.4	36	12	6	6	25.2	4.2
72	86.4	36	12	6	6	22.0	3.6
72	100.7	45	12	6	8	29.4	4.2
63	**100.7**	**45**	**12**	**6**	**8**	**33.6**	**4.8**

The force distribution is shown in Figure 3.10; this indicates that the maximum allowable force (assuming that the ball is fixed and the socket allowed to slide freely) is approximately 100N for a single row of ½" (12mm) magnets. Additionally, the optimal socket size is determined to be 63°, which results in the highest socket pressure for the given surface area and preload force. The prototype socket angle is 75°, chosen based on the ball and shaft sizes; this optimization indicates that the socket can be made 15% smaller without loss of predicted performance.

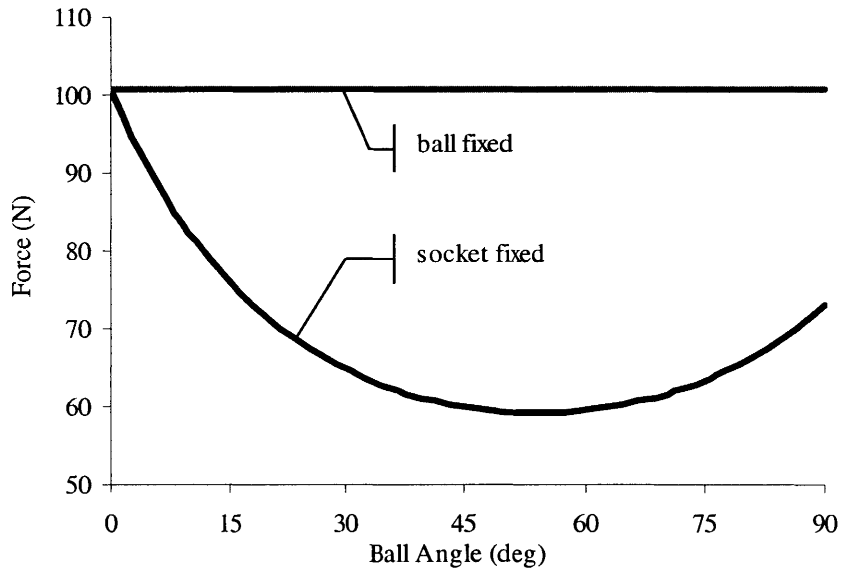

Figure 3.10 Sliding and fluid contact force distribution

3.2.3 Point and Rolling Contact Prototypes

The force balance for the point and rolling contact joints is similar to the sliding contact joint, in terms of applied and preload forces, however as the contact region is now a point, the reaction force angle is known. The force balance can then be solved in three dimensions for the three normal forces at the contact region. The magnets are arranged in two rows around the socket to accommodate the fixed tooling balls in the point contact joint and the ball transfers in the rolling contact joint. Performing an equivalent optimization to the sliding contact joint yields a configuration with six ¼" (6mm) magnets at 45° as well as eight ¼" (6mm) magnets at 22°. This yields a preload force of 50N for a single row of magnets, increasing to 65N with three layers of un-shunted magnets.

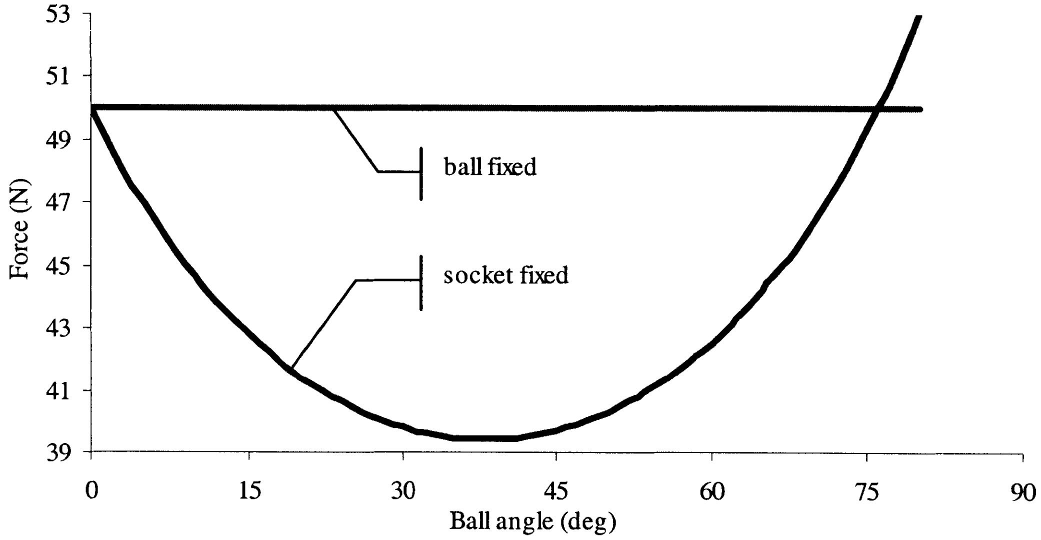

Figure 3.11 Preload characteristics for point and rolling contact joint

The preload characteristics are similar to the sliding contact joint in that the ball fixed case displays a constant preload. Additionally, the socket fixed case has the same preload at a ball angle of zero degrees, however the degradation is merely 20% as the ball is moved through the workspace. Finally, at large ball angles (greater than 75°), a force magnification is achieved, due to the influence of the reaction forces at the contact spheres.

3.3 Accuracy Analysis

Each spherical joint prototype is modeled as a simple three degree-of-freedom mechanism, with three orthogonal axes: roll (rotation about the joint x-axis); pitch (y-axis rotation); and yaw (z-axis rotation). This allows each of the joints to be modeled and measured in the same fashion and the final accuracy characteristics directly compared. Two key models have been developed: a sphere fit model and a kinematic model.

3.3.1 Sphere Fit Model

The sphere fit model assumes all axes intersect at a common location and fits a sphere center and radius to the measurement data by minimizing the residual error between the predicted tooling ball location and the measured position (Figure 3.12). The remaining residual error represents the accuracy of the joint.

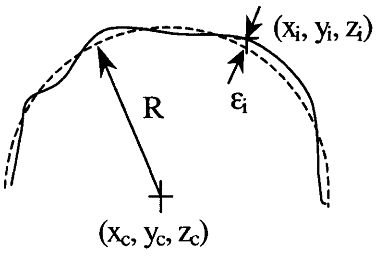

$$\varepsilon_i = R - \sqrt{(x_i - x_c)^2 + (y_i - y_c)^2 + (z_i - z_c)^2}$$

$$F(x_c, y_c, z_c, R) = \min\left(\sum_i \left(\varepsilon_i^2\right)\right)$$

Where:

x_i, y_i, z_i : measured coordinates
x_c, y_c, z_c : sphere center coordinates
ε_i : residual radial error

Figure 3.12 Spherical joint sphere fit model

3.3.2 Kinematic Model

Structural Loop

The kinematic model extends the sphere-fit model by introducing a nominal forward kinematic model between the measurement system and the end effector (Figure 3.13 and Figure 3.14). Six frames are introduced to describe the joint center in relation to the measurement system coordinate frame; the roll, pitch and yaw joint angles; and the tooling ball center in relation to the joint center. The spherical joint angles are used as input to the kinematic model to determine the position of the tooling ball center. In a similar error minimization process to the sphere-fit, the nominal forward kinematic model attempts to fit the joint center and end effector location (radius) to the measurement data.

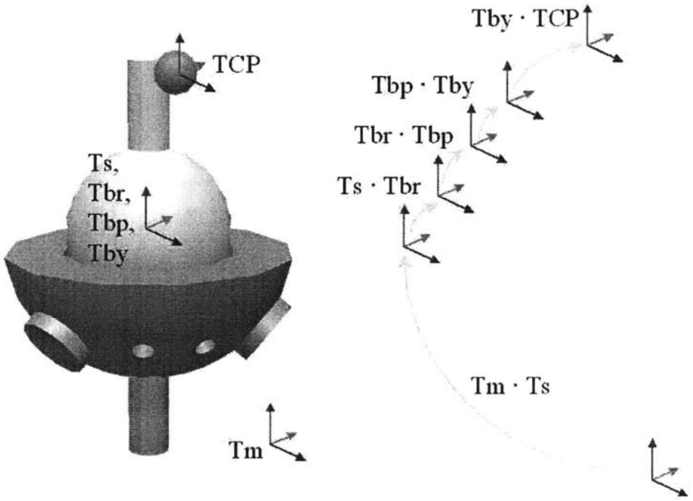

Frame descriptions:

1. Tm: measurement system
2. Ts: socket
3. Tbr: ball roll (θ_1)
4. Tbp: ball pitch (θ_2)
5. Tby: ball yaw (θ_3)
6. TCP: end effector

Figure 3.13 Spherical joint structural loop

The extended forward kinematic model introduces position and orientation errors between each of the nominal kinematic frames in order to characterize the location and magnitude of the joint errors. Initially, the set of error parameters over defines the system and it is necessary to reduce the number of parameters such that only the non-redundant error sources are considered. This is achieved by computing a numerical Jacobian matrix from a sequence of joint positions (Figure 3.15).

Nominal Forward Kinematics :

$$X(x,y,z) = F(\theta_1,\theta_2,\theta_3)$$
$$= Tm \cdot Ts \cdot Tbr \cdot Tbp \cdot Tby \cdot TCP$$

Where :

$X(x,y,z)$: calculate position

θ_1 : roll angle

θ_2 : pitch angle

θ_3 : *yaw* angle

Figure 3.14 Spherical joint nominal kinematic model

Extended kinematic model:

$$X(x,y,z) = F(\theta,\varepsilon)$$

$F(\theta,\varepsilon)$: forward kinematic model

$X(x,y,z)$: calculated position vector

θ : joint angle $(\theta_1,\theta_2,\theta_3)$ vector

ε : error parameter vector

Jacobian:

$$J = \begin{pmatrix} \frac{\partial F_x(\theta_1)}{\partial \varepsilon_1} & \frac{\partial F_x(\theta_1)}{\partial \varepsilon_2} & \cdots & \frac{\partial F_x}{\partial \varepsilon_{nn}} \\ \frac{\partial F_y(\theta_1)}{\partial \varepsilon_1} & & & \\ \frac{\partial F_z(\theta_1)}{\partial \varepsilon_1} & & & \\ \vdots & & \ddots & \vdots \\ \frac{\partial F_z(\theta_M)}{\partial \varepsilon_1} & & \cdots & \frac{\partial F_z(\theta_M)}{\partial \varepsilon_{n1}} \end{pmatrix}$$

Singular Value Decomposition

$$J = U \cdot S \cdot V^T$$

U : left eigenmatrix (orthonormal: $U^{-1} = U^T$)

S: eigenvalue matrix (diagonal matrix)

V : right eigenmatrix (orthonormal: $V^{-1} = V^T$)

Figure 3.15 Singular value decomposition

Model Reduction

The joint angles are determined randomly, subject to an "Equal Distribution Criteria" which dictates that each position should differ from all the other joint positions. This ensures that the full working area of the joint is considered in the analysis and calibration process and that redundant joint positions are not used. Given a sufficiently large simulated pose set (approximately 100 poses), the model can be reduced until the condition number of the Jacobian is below 50. The process is typically manually performed wherein the right eigenmatrix (V) from each iteration's SVD breakdown of the Jacobian is analyzed for matching pairs or singular values. A Matlab script has been created to automate the process, and a 20 trial reduction used to determine the most common solution. The model reduction reveals 6 observable parameters for the joint assembly. The chosen parameter set is shown in Table 3.2; parameters coincident with the joint angles are ignored and the joint center frame is calibrated, requiring Tx, Ty and Tz parameters as well as Rx, Ry and Rz parameters. This analysis is completed without consideration for passive joint realignment; that should an error be introduced the passive joints will realign to minimize the error. A forward kinematic model should be developed to minimize the error by altering the passive joint angles within a certain range. This is physically equivalent to finding the position of minimal stress or minimal energy.

TABLE 3.2 Reduced calibration model parameters

Type	Frame	Parameter	Index	Description
Required	Tm_Ts	TxTyTz RxRyRz	1...6	Full 6DOF base frame required to transform measurement data in measurement system base frame to socket frame (relationship between measurement system location and the joint base coordinate system)
Required	Tby_TCP	TxTyTz	25...27	Full positional TCP (rotational elements only observable with 6DOF measurement system)
Choose All	Ts_Tbr	Rz	12	Z–axis rotation error (roll axis)
	Tbr_Tbp	Tz	15	Z–axis translation error (pitch axis)
	Tbp_Tby	Tx	19	X–axis translation error (yaw axis)
	Tbp_Tby	Rx	22	X–axis rotation error (yaw axis)
Choose 1	Tbr_Tbp	Ty	14	Y–axis translation error (pitch axis)
	Tbp_Tby	Ty	20	Y–axis translation error (yaw axis)
Choose 1	Ts_Tbr	Ry	11	Y–axis rotation error (roll axis)
	Tbp_Tby	Ry	23	Y–axis rotation error (yaw axis)

The full set of error parameters comprises 6 parameters for the base frame; 3 for the TCP; 3 for the positional error between axes; and 3 for the off-axis rotational error between axes. Given input joint angles, and values for the error parameters, the error forward kinematics will output the position of the tool center point of the joint.

Calibration

A linear regression solver, utilizing the singular value decomposition of the Jacobian matrix, is then used to determine the error parameters by comparing the error forward kinematics with the measured positions (Figure 3.16). This process is derived from robot calibration applications *[Hayati et al, 1985]*, however in this case the input joint angles are not well known due to the inaccuracies of the spherical kinematic test rig. The input joint angles are recomputed in a similar fashion to the error parameters; an inverse kinematic model is developed to compute the joint angles given an end-effector coordinate.

Calibration :	
$E = M - X$	$E(x, y, z)$: error vector
	$M(x, y, z)$: measured positions
	$X(x,y,z)$: calculated position
$J \cdot \partial\varepsilon = E$	$\partial\varepsilon$: parameter update vector
$U \cdot S \cdot V^T \cdot \partial\varepsilon = E$	substitute SVD of Jacobian matrix
$\partial\varepsilon = V \cdot \left(\frac{1}{S}\right) \cdot U^T \cdot E$	compute parameter update vector
Leap Frog Solver :	
$\theta_{new} = F^{-1}(X,\theta,\varepsilon)$	
$\theta = \theta_{new}$	$F^{-1}(X,\theta,\varepsilon)$: inverse kinematics
	θ_{new} : updated joint angles

Figure 3.16 Calibration algorithm

For each iteration, the error parameters are determined for a given set of joint angles, the joint angles are recomputed and the next iteration error parameters determined from the new joint angles. This process is referred to as a "leap-frog" solver as solver alternates between output error parameters and input joint angles. The measured coordinates do not change, and the final converged represents the best fit between the measured coordinates and the end-effector positions computed from the joint angles. If the error parameters are set to zero (i.e. only the joint center and radius are calibrated), then the extended forward kinematic model becomes the nominal forward kinematic model which is numerically equivalent to the sphere fit model.

The joint angles are recomputed using the inverse kinematics algorithm, which can be determined analytically given a simple system, however for flexibility and consistency, a similar Jacobian based approach as implemented for the error parameter calibration is used (Figure 3.17). Each iteration involves a parameter estimation followed by a re-computation of the joint angles; both components should converge following a certain number of iterations.

Inverse Kinematics :

$$\theta = F^{-1}(M, \theta, \varepsilon)$$

where :

$$\theta = \theta(\theta_1, \theta_2, \theta_3) = \text{joint angles}$$

$$M = M(x, y, z) = \text{measured positions}$$

Jacobian :

$$J = \begin{pmatrix} \frac{\partial F_x}{\partial \theta_1} & \frac{\partial F_z}{\partial \theta_2} & \frac{\partial F_z}{\partial \theta_3} \\ \frac{\partial F_y}{\partial \theta_1} & \frac{\partial F_y}{\partial \theta_2} & \frac{\partial F_y}{\partial \theta_3} \\ \frac{\partial F_z}{\partial \theta_1} & \frac{\partial F_z}{\partial \theta_2} & \frac{\partial F_z}{\partial \theta_3} \end{pmatrix}$$

SVD :

$$J = U \cdot S \cdot V^T$$

Calibration :

$$E = M - F = \text{Error Vector}$$

$$\partial\theta = \text{joint update vector}$$

$$J \cdot \partial\theta = E$$

$$U \cdot S \cdot V^T \cdot \partial\theta = E$$

$$\partial\theta = V \cdot \left(\frac{1}{S}\right) \cdot U^T \cdot E$$

$$\theta = \theta + \partial\theta$$

Figure 3.17 Error model inverse kinematics

Error Budget

A Monte Carlo simulation is used to determine the final positional error distribution at the tool center point. A set of 100 joint angles are randomly generated, subject to the "Equal Distribution Criteria", and each parameter is assigned a random value from within a certain range. The range of values for each parameter is typically determined by the physical entity that the parameter represents. For example, the positional error between axes represents an asphericity of the ball, which is determined to be on the order of one micrometer as stated by the manufacturer's specifications. Furthermore, errors must be characterized as stochastic or systematic. Stochastic errors represent those conditions which occur randomly during the operation of the joint, such as friction or wear. Systematic errors include those effects that are consistent during the operation of the joint, such as physical eccentricities in the ball shape. Stochastic errors contribute to the repeatability of the joint and systematic errors contribute to the accuracy of the joint.

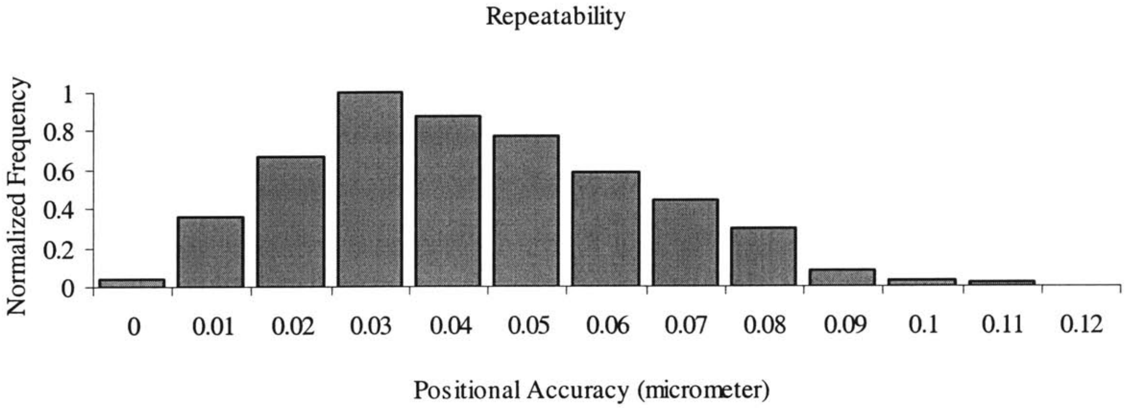

Figure 3.18 Error budget repeatability

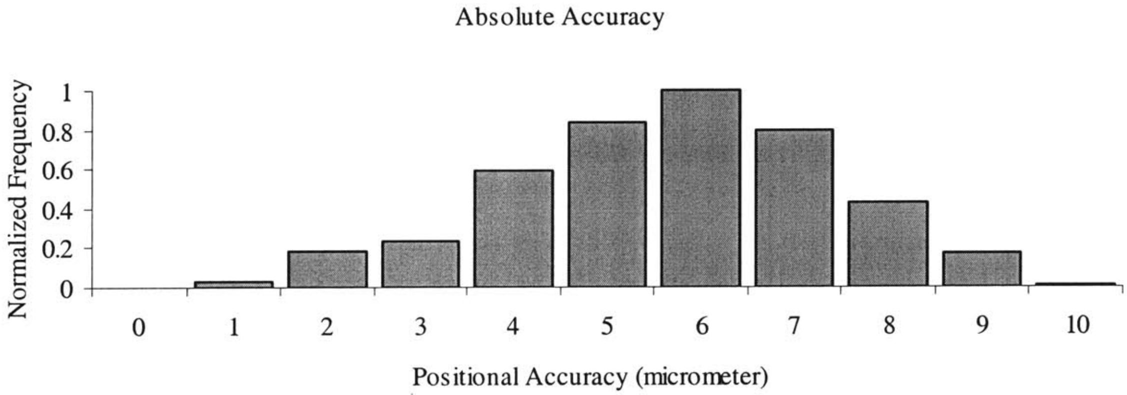

Figure 3.19 Error budget accuracy

For each joint angle, the error parameters are initially set to zero to obtain the nominal position. Following this, 1000 variations of error parameters within the defined ranges are tested and the difference between the output and nominal positions is registered. This is completed for both the repeatability and accuracy error parameters and the final differences collated into a normalized distribution. The worst case situation (mean plus three standard deviations) predict a repeatability of 0.1µm (Figure 3.18) and an accuracy of 10µm (Figure 3.19).

3.4 Thermal Analysis

During the measurement process it is important to consider the effect of temperature variation on the joint accuracy. The primary structure subject to variation is the socket, which is modeled as a simple column of length 2" (50mm) as shown in Figure 3.20.

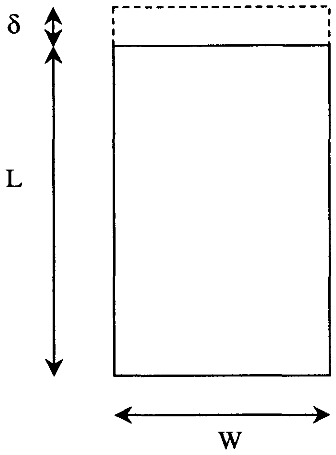

Thermal expansion

$$\delta = L \cdot \alpha_T \cdot \Delta T \qquad \mu\text{m}$$

$$\frac{\delta}{\Delta T} = \alpha_T \cdot L \qquad \frac{\mu\text{m}}{°C}$$

Coefficients

$$\alpha_{T\,\text{aluminum}} = 23.6 \qquad \frac{\mu\text{m}}{\text{m}}$$

$$L = 50 \qquad \text{mm}$$

Expansion of socket column

$$\frac{\delta}{\Delta T} = 23.6 \cdot 50 \times 10^{-3} \qquad \frac{\mu\text{m}}{°C}$$

$$= 1.18 \qquad \frac{\mu\text{m}}{°C}$$

Figure 3.20 Thermal expansion of joint socket

The change in height of the column is determined to be approximately 1μm/°C. In order to ensure that temperature effects do not alter the accuracy of the measurements, the temperature should not change by more than 0.5° over the course of the measurements. This can be achieved in a temperature stabilized room and by monitoring the temperature around the test environment.

3.5 Contact Analysis

The deformation due to Hertz contact between two spherical objects must be considered in the accuracy budget of the point and rolling contact prototypes. The schematic for the force and contact mechanisms is detailed in Figure 3.21, where the ball radius (r_1) is typically 1" (25mm) and the socket sphere radius (r_2) is typically ½" (12mm). The socket angle (θ) is found through optimization to be 45° and the worst case preload force is 100N, resulting in a contact force of approximately 70N.

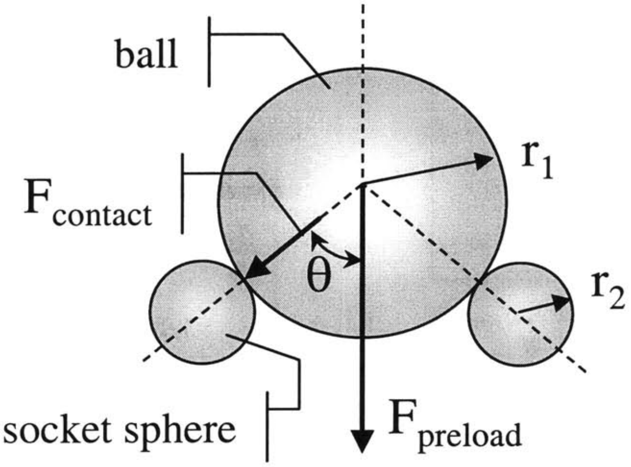

Figure 3.21 Contact mechanics for point and rolling contact joints

The deformation due to contact stress between the ball and the socket can be determined using Hertzian contact stress analysis *[Slocum, 1992]*, and is summarized in Figure 3.22 and Figure 3.23.

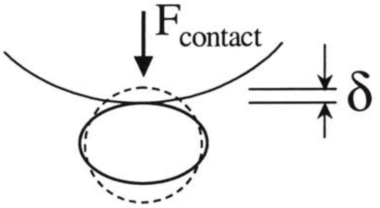

$$\delta = \lambda \left(\frac{2F_{contact}^2}{3 r_{eq} E_{eq}^2} \right)^{\frac{1}{3}}$$

Figure 3.22 Deformation between two spheres

Equivalent radius :

$$r_{eq} = \frac{1}{\left(\frac{1}{r_{1\,\mathrm{maj}}} + \frac{1}{r_{1\,\mathrm{min}}} + \frac{1}{r_{2\,\mathrm{maj}}} + \frac{1}{r_{2\,\mathrm{min}}}\right)}$$

Equivalent elastic modulus :

$$E_{eq} = \frac{1}{\left(\frac{1-\upsilon_1^2}{E_1} + \frac{1-\upsilon_2^2}{E_2}\right)}$$

υ : Poissons ratio

Contact coefficient (λ) :

$$\cos(\theta) = r_{eq}\sqrt{\left(\frac{1}{r_{1\,\mathrm{maj}}} - \frac{1}{r_{1\,\mathrm{min}}}\right)^2 + \left(\frac{1}{r_{2\,\mathrm{maj}}} - \frac{1}{r_{2\,\mathrm{min}}}\right)^2 + 2\left(\frac{1}{r_{1\,\mathrm{maj}}} - \frac{1}{r_{1\,\mathrm{min}}}\right)\left(\frac{1}{r_{2\,\mathrm{maj}}} - \frac{1}{r_{2\,\mathrm{min}}}\right)\cos(2\phi)}$$

ϕ : angle between the planes of principal curvature of the two bodies

$$\lambda = -0.214e^{-4.950\theta} - 0.179\theta^2 + 0.555\theta + 0.319$$

Figure 3.23 Hertz contact deformation coefficients

A spreadsheet (Table 3.3) is used to predict the final deformation under the given conditions. As the contact is between two spherical surfaces, only the minimum radii are considered, furthermore, the maximum contact stress is set to 75% of the yield stress. The resultant deflection of 0.5μm is negligible under the given preload forces. As such, Hertz deformation effects can be ignored for the point and rolling contact joints.

TABLE 3.3 Hertz contact deformation spreadsheet

Ronemaj	**1.00E+06**	Equivalent radius Re	0.0050
Ronemin	**2.54E-02**	costheta	1.0000
Rtwomaj	**1.00E+06**	theta	0.0002
Rtwomin	**6.30E-03**	alpha	3601.7275
Applied load F	**100**	beta	0.1702
Phi (degrees)	**0**	lambda	0.1053
Max contact stress	**2.25E+08**	ellipse c	6.85E-01
Elastic modulus Eone	**2.00E+11**	ellipse d	3.24E-05
Elastic modulus Etwo	**2.00E+11**	Contact pressure	2.15E+06
Poisson's ratio vone	**0.3**	Stress ratio (< 1)	0.01
Poisson's ratio vtwo	**0.3**	**Deflection (μunits)**	**0.50**
		Stiffness (load/μunits)	198.5

3.6 Preload Measurement

Individual magnets are connected to the ball via the 1/16" (1.5mm) spacer and a force exerted using a weight scale, until the separation force is reached. Figure 3.24 details the measurement setup and the separation force for each magnet for the 1/4" (6mm) and 1/2" (12mm) magnet varieties used in the prototypes.

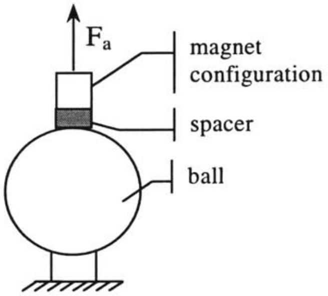

		Separation Force (N)		
Magnet	Stack:	1	2	3
1/2" (12mm)		18	24	27
1/4" (6mm)		4.5	5.4	5.8

Figure 3.24 Measurement of magnet force

The magnet point forces are used in the preload optimization routines to determine the preload force for a single row of magnets arranged about the socket. The separation force of the joints is measured in a tensile tester and the correlation between the predicted preload force and the measured for the individual magnet case is shown in Figure 3.25. The predicted agrees with the measured to within 10%.

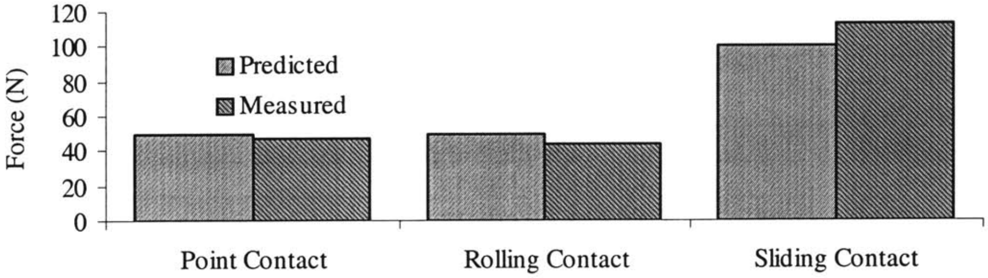

Figure 3.25 Measured and predicted preload forces

3.7 Measurement and Calibration

A Brown and Sharpe coordinate measurement machine in the MIT Laboratory for Manufacturing and Productivity is used to measure a set of test rig poses. In total 31, poses are measured, chosen for convenience and access rather than randomly generated as is typically the case. The joint is mounted in the test rig using a vice that is clamped to the table to avoid unwanted movements in the test rig. The CMM probe is calibrated to the known reference sphere and the accuracy tested by measuring a known flat of 4" (100mm) length. The accuracy of the CMM is found to be 0.0001" (2.5μm). For measurement of the joint end-effector, a sphere fit method is used in the CMM software to determine the center of the tooling ball sphere mounted on the ball shaft. For each pose of the joint, approximately 15 measurements of the tooling ball sphere are taken to ensure an accurate calculation of the tooling ball center. The test rig is used to position the joint approximately in a known position. The approximate joint positions and the measurements are then input into the calibration and modeling programs.

3.7.1 Rolling Contact Joint

The first step of the modeling process involves determining the validity of the absolute accuracy approach. To determine this, the results from the sphere fit are compared with the results from a calibration of the nominal joint. Both of these methods attempt to determine the joint center and the radius (magnitude or x, y, z components) by minimizing the residual error. In the case of the sphere fit, the residual error is the sum of the squares of the radial error, for the absolute accuracy it is the sum of the squares of the distance between the theoretical position and the measured position. The results from the two calibrations (Table 3.4) indicate that the sphere center (or CMM base) are co-located to within numerical accuracy. Furthermore, the sphere radius as computed by the sphere fit method is equivalent to the effective radius (the Euclidean norm of the x, y and z components of the TCP) as computed by the parameter calibration. This indicates that the two methods are compatible and that the absolute accuracy analysis described in Section 3.3 is valid.

TABLE 3.4 Comparison of calibration methods

Frame	Parameter	Sphere Fit	Base and TCP
Tm	Tx (mm)	**123.88**	**123.88**
	Ty (mm)	**28.11**	**28.11**
	Tz (mm)	**-205.64**	**-205.64**
	Rx (deg)		4.06
	Ry (deg)		-0.77
	Rz (deg)		-1.83
TCP	Tx (μm)		-18.71
	Ty (μm)		-1.81
	Tz (μm)		41.12
	Effective Radius (mm)		**45.21**
	Measured Radius (mm)	**45.21**	
Error	Mean (um)	2.70	2.70
	Mean+3SD (um)	12.00	12.00
	CMM (um)	2.00	2.00

The CMM, with an accuracy of 2 micrometer in the working range of the test rig, is used to measure the rolling contact joint. The absolute accuracy calibration can now be extended to include the positional and rotational errors in the joint. This is useful from an overall viewpoint in that when implemented in a robot manipulator that will be calibrated, it is necessary to determine the final compensated error of the joint. The results from several calibrations are detailed in Table 3.5; the final error for both calibrations is an improvement on the original error and converges to the repeatability of the CMM. The error parameters determined are consistent with those predicted in the error gain analysis (refer to Figure 3.19).

The accuracy distribution is presented in Figure 3.26: the sphere fit model results in a maximum error of approximately 12μm; the kinematic model reduces this error to 8μm. The mean and standard deviation of both models is of the order of 3μm. This indicates that the un-calibrated joint is accurate to within 12μm within its working range, and this can be further improved to 8μm with the addition of the position and orientation error parameters.

TABLE 3.5 Kinematic calibration

Frame	Parameter	Sphere Fit	Base and TCP	Position Offset	All Parameters
Tm	Tx (mm)	123.88	123.88	123.88	123.88
	Ty (mm)	28.11	28.11	28.10	28.10
	Tz (mm)	-205.64	-205.64	-205.63	-205.63
	Rx (deg)		4.06	4.05	-2.18
	Ry (deg)		-0.77	-0.93	1.48
	Rz (deg)		-1.83	-1.86	-2.10
TCP	Tx (μm)		-18.71	-18.61	-17.95
	Ty (μm)		-1.81	-1.82	-1.64
	Tz (μm)		41.12	41.18	41.48
Troll	Ry (deg)				-3.14
	Rz (deg)				1.63
Tpitch	Ty (μm)			-2.54	0.67
	Tz (μm)			-25.40	-22.95
Tyaw	Tx (μm)			20.32	25.47
	Rx (deg)				6.03
	Radius (mm)	45.21			
	Effective Radius (mm)		45.21	45.23	45.23
Error	Mean (μm)	2.70	2.70	2.40	1.95
	Mean+3SD (μm)	12.00	12.00	8.20	7.78
	CMM (μm)	2.00	2.00	2.00	2.00

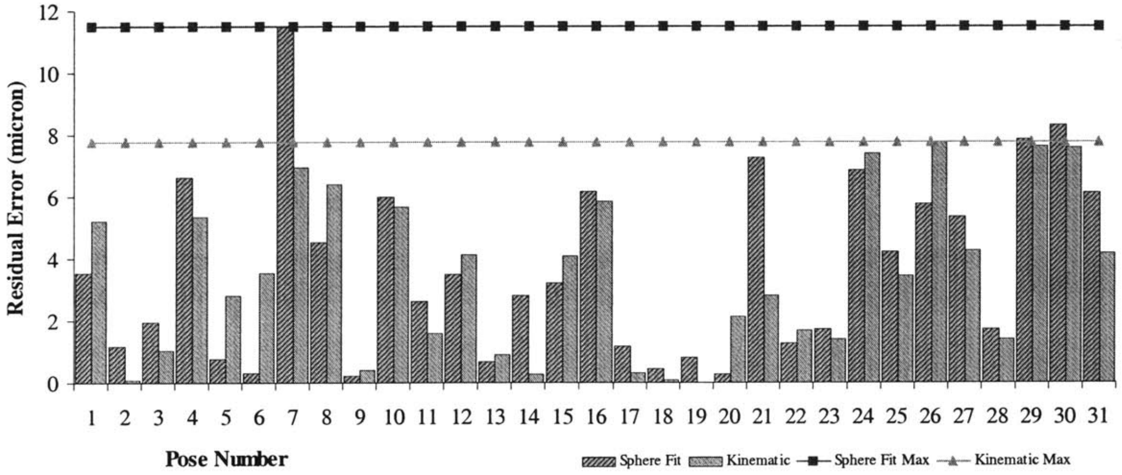

Figure 3.26 Accuracy distribution of rolling contact prototype

3.7.2 Point Contact Joint

The point contact prototype accuracy distribution is detailed in Figure 3.27. The maximum error is 22μm prior to calibration which is approximately double the predicted maximum error. This discrepancy is believed to be due to the high friction inherent in the joint design which can cause the test rig to torque the ball about one of the balls in the socket, resulting in a non-kinematic coupling between ball and socket.

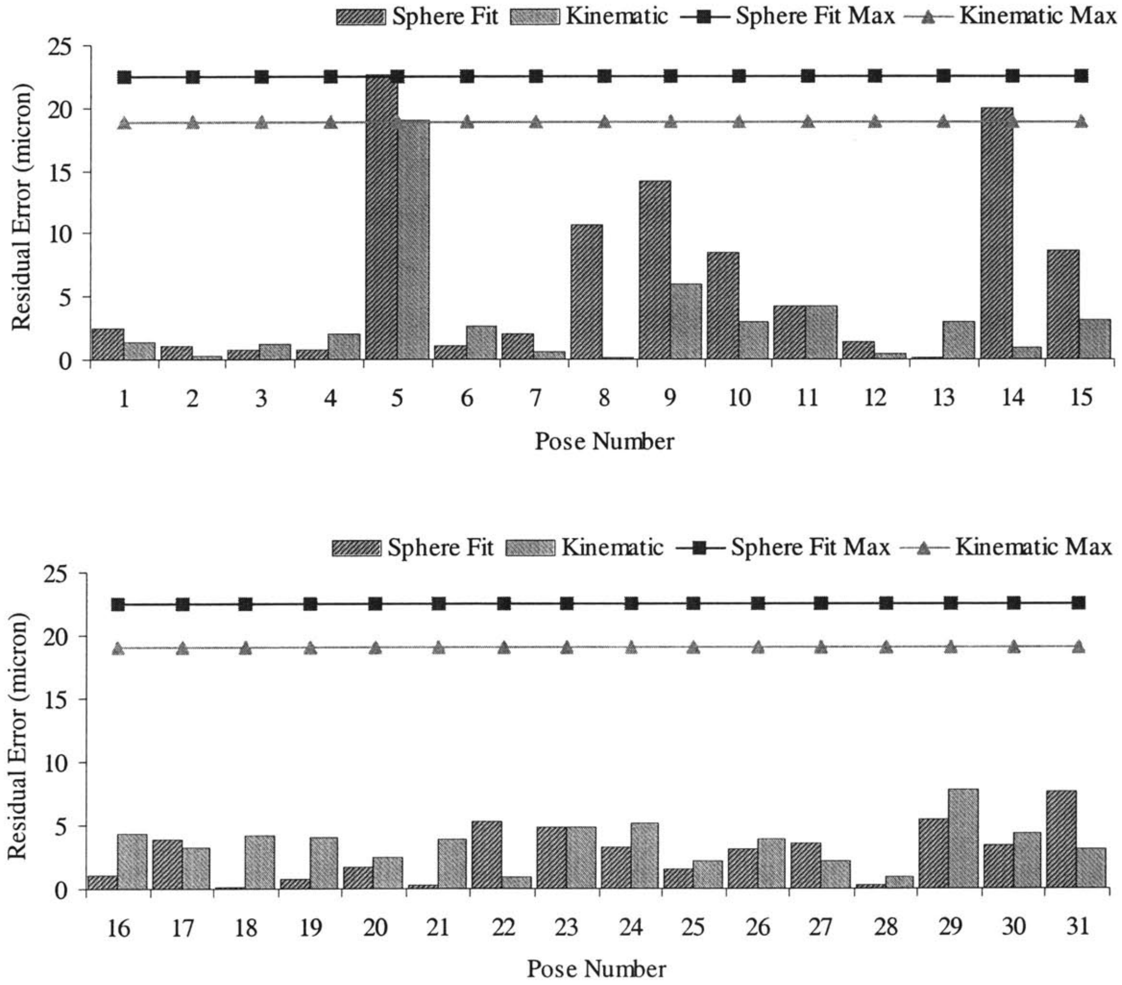

Figure 3.27 Accuracy distribution of point contact prototype

3.7.3 Sliding Contact Joint

The accuracy distribution of the sliding contact joint is detailed in Figure 3.28. The maximum error of 16μm is comparable to the predicted maximum error of 10μm; the discrepancy is likely to be due to irregularities in the replication process. Additionally, the high friction inherent in the joint can degrade the accuracy in a similar manner to with the point contact joint.

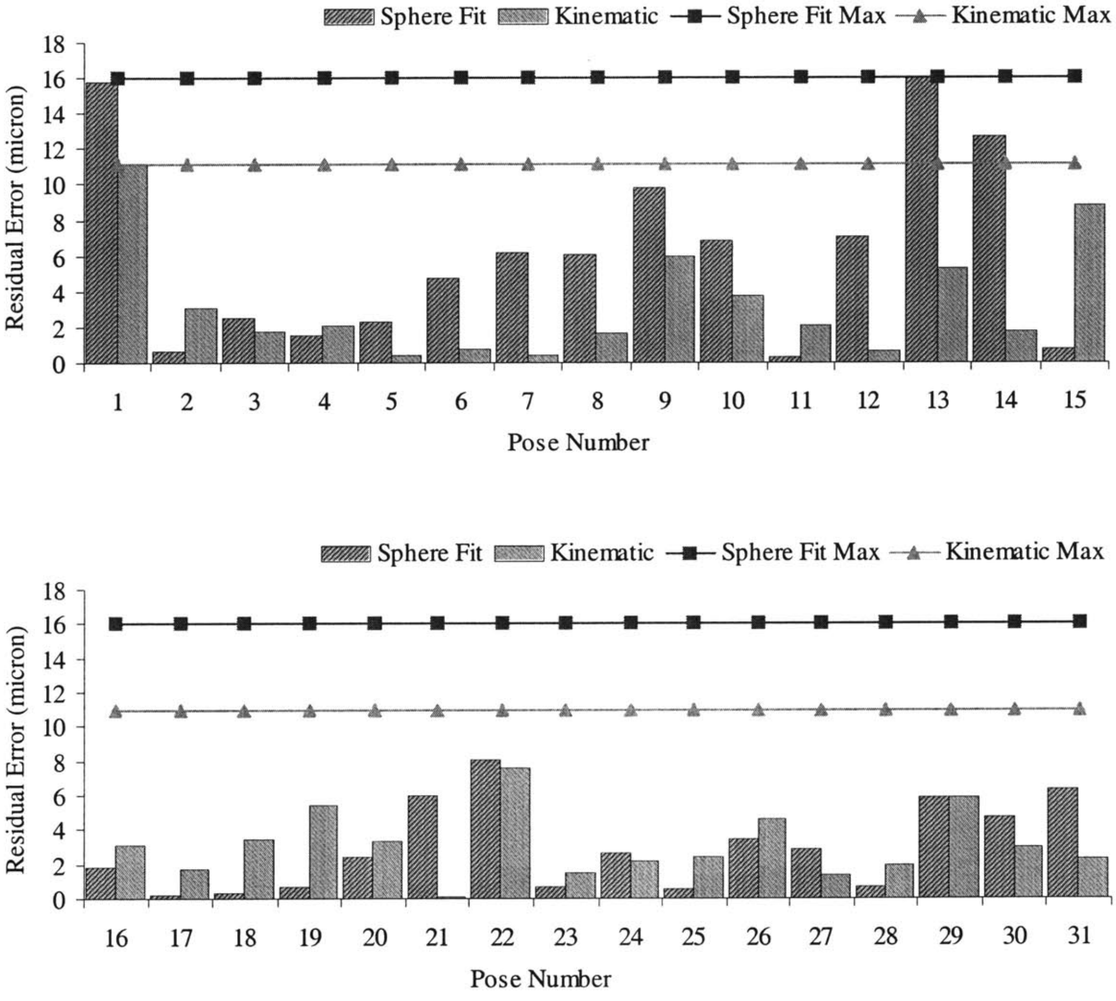

Figure 3.28 Accuracy distribution of sliding contact prototype

3.7.4 Joint Comparison

A summary of the joint measurements is presented in Table 3.29. The results agree with the initial estimations for the point and sliding contact joints, and are within the level of accuracy of the coordinate measurement machine used (approximately 2 to 3 micrometers). The point contact joint displays double the predicted error, due to high friction inherent in the direct point contact between the ball and the socket. The predicted preload forces agree to within 10% for each of the three joint prototypes, as summarized in Figure 3.30.

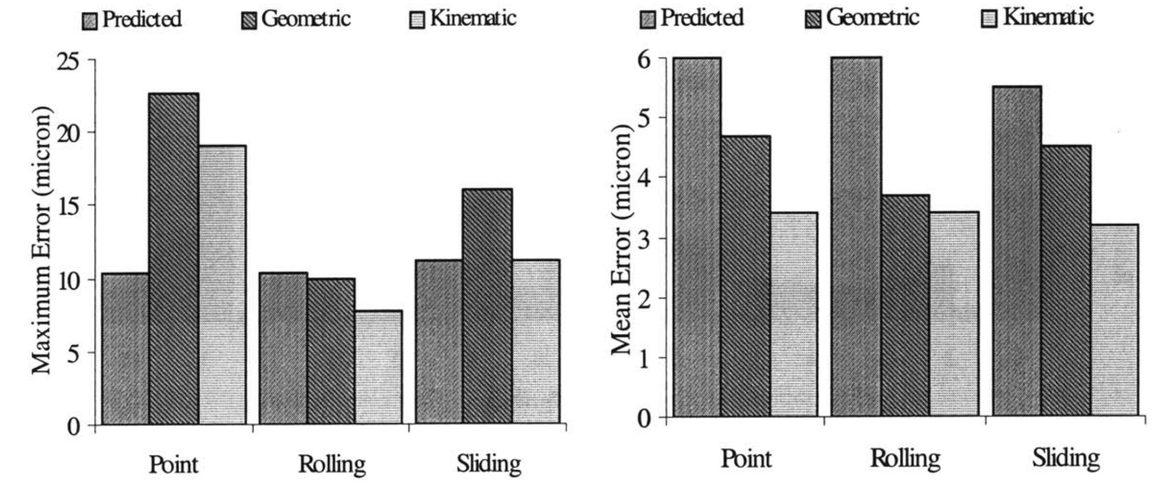

Figure 3.29 Maximum and mean residual errors for joint prototypes

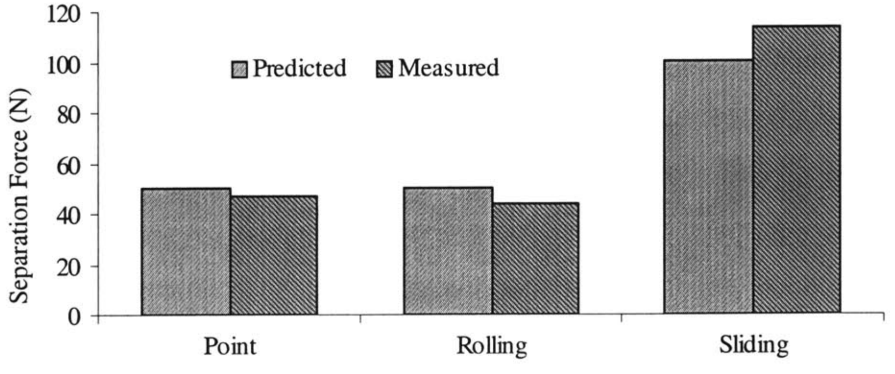

Figure 3.30 Predicted and measured preload forces

3.8 Conclusions

Three spherical joint prototypes have been developed for parallel robot applications. Each joint comprises an aluminum socket and a solid steel ball, preloaded by permanent magnets. The point contact prototype mounts the ball kinematically in the socket. The rolling contact joint significantly reduces friction by kinematically mounting the ball on rolling ball-transfers. The surface contact prototype uses replication to achieve a high-accuracy mating surface. A spherical kinematic test rig is used to actuate each joint to a predefined position, which is measured by a coordinate measurement machine. The resultant un-calibrated accuracy of the rolling contact joint is 12μm, which is reduced to 8 micron through calibration.

A fourth prototype is detailed in Chapter 4, based on a fluid contact mechanism. The replicated sliding contact design is extended to include three orifices placed around the socket to create a thin film of air between the ball and the socket. This significantly reduces the friction inherent in the replicated prototype while maintaining the high accuracy expected of a replicated joint.

The error distribution remaining after the kinematic calibration has a large discrepancy between maximum and minimum residuals. This indicates that the simple kinematic error model insufficiently describes the physical phenomena underlying the measured joint. An improved model will be investigated in Chapter 5 with the goal of reducing the calibrated joint error.

Chapter 4

FLUID CONTACT JOINT

4.1 Overview

The basic design of the fluid contact joint is inherited from the sliding contact joint. High-pressure air is injected into the base of the socket via a certain number of orifices, resulting in a thin air gap that supports the ball. The magnets arranged around the socket continue to provide the necessary preload to prevent separation. Given the available preload, the orifice aperture diameter and the air flow rates and pressures must be determined.

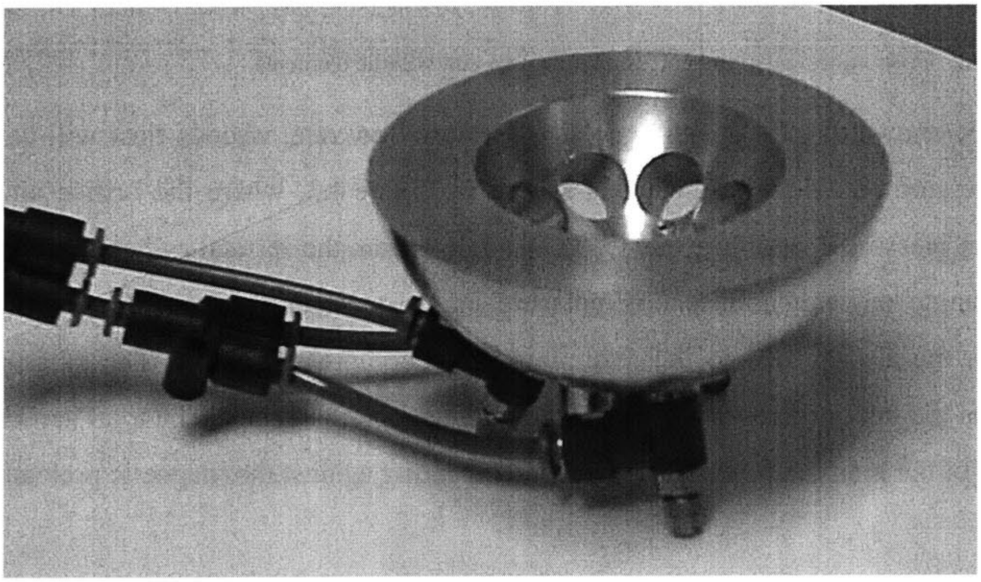

Figure 4.1 Fluid contact joint prior to replication

4.2 Analysis

4.2.1 Fluid Flow Analysis

From the basic sliding contact design, it is known that the maximum preload force is around 150N for three rows of magnets, decreasing to approximately 100N for a single row of magnets. The volume flow rate and pressure required to create an air gap under these preload forces needs to be determined; these in turn determine the characteristics of the orifices, in particular the aperture diameter. The fluidic system is modeled using a flat-plate assumption modeled by the Navier-Stokes equation in cylindrical coordinates (Figure 4.2) and neglecting inertia terms.

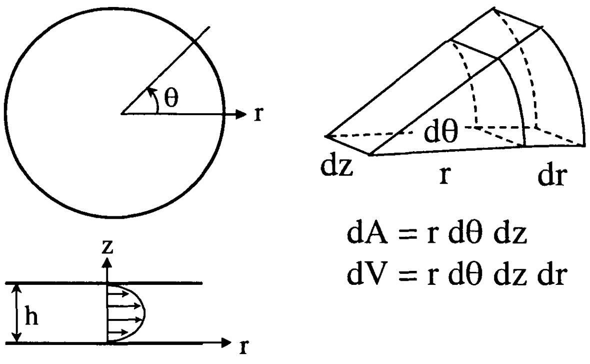

Figure 4.2 Polar coordinates and corresponding area and volume elements

It can be shown that for a small gap size and low flow rate, viscous flow will dominate. The pressure and flow schematic is shown in Figure 4.3, where the orifice air supply enters at pressure P_i and flow rate Q_i, at an angle ϕ from the vertical and exits at the socket edge (angle α) with atmospheric pressure P_a. A constant flow rate Q_i is maintained through the air gap due to the assumption of incompressible flow. The pressure drop between the inlet orifices and socket edge outlet supports the ball. The total vertical component of the pressure force must support the bearing against the magnetic preload force.

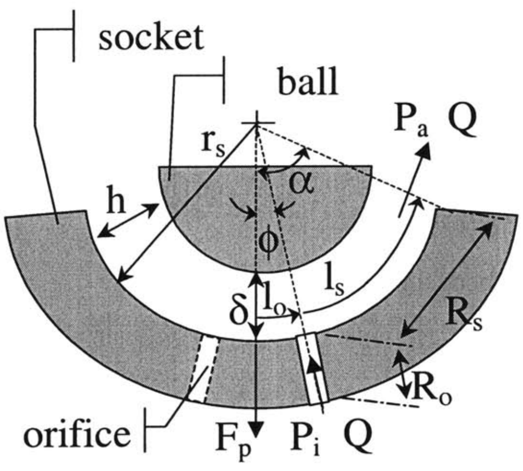

r_s	Socket radius
h	Air gap width
δ	Vertical displacement of ball
α	Socket arc angle
φ	Orifice arc angle
l_o	Orifice arc length
l_s	Socket arc length
P_i	Inlet pressure
Q	Flow rate
P_a	Outlet pressure (atmospheric)
R_o	Orifice resistance function
R_s	Socket resistance
h_0	Initial air gap
F_p	Vertical preload force

Figure 4.3 Fluid contact joint schematic

The Navier Stokes equations (Figure 4.4) in cylindrical coordinates describe the generic equations of motion for Newtonian fluids subject to incompressible flow.

$$\text{r axis}: \quad \rho\left(\frac{\partial u_r}{\partial t}+u_r\frac{\partial u_r}{\partial r}+\frac{u_\theta}{r}\frac{\partial u_r}{\partial \theta}-\frac{u_\theta{}^2}{r}+u_z\frac{\partial u_r}{\partial z}\right)=$$

$$-\frac{\partial P}{\partial r}+\mu\left(\frac{\partial^2 u_r}{\partial r^2}+\frac{1}{r}\frac{\partial u_r}{\partial r}-\frac{u_r}{r^2}+\frac{1}{r^2}\frac{\partial^2 u_r}{\partial \theta^2}+\frac{\partial^2 u_r}{\partial z^2}-\frac{2}{r^2}\frac{\partial u_\theta}{\partial \theta}\right)+F_r$$

$$\theta\text{ axis}: \quad \rho\left(\frac{\partial u_\theta}{\partial t}+u_r\frac{\partial u_\theta}{\partial r}+\frac{u_\theta}{r}\frac{\partial u_\theta}{\partial \theta}-\frac{u_r u_\theta}{r}+u_z\frac{\partial u_\theta}{\partial z}\right)=$$

$$-\frac{1}{r}\frac{\partial P}{\partial \theta}+\mu\left(\frac{\partial^2 u_\theta}{\partial r^2}+\frac{1}{r}\frac{\partial u_\theta}{\partial r}-\frac{u_\theta}{r^2}+\frac{1}{r^2}\frac{\partial^2 u_\theta}{\partial \theta^2}+\frac{\partial^2 u_\theta}{\partial z^2}-\frac{2}{r^2}\frac{\partial u_r}{\partial \theta}\right)+F_\theta$$

$$z\text{ axis}: \quad \rho\left(\frac{\partial u_z}{\partial t}+u_r\frac{\partial u_z}{\partial r}+\frac{u_\theta}{r}\frac{\partial u_z}{\partial \theta}+u_z\frac{\partial u_z}{\partial z}\right)=$$

$$-\frac{\partial P}{\partial z}+\mu\left(\frac{\partial^2 u_z}{\partial r^2}+\frac{1}{r}\frac{\partial u_z}{\partial r}+\frac{1}{r^2}\frac{\partial^2 u_z}{\partial \theta^2}+\frac{\partial^2 u_z}{\partial z^2}\right)+F_z$$

Figure 4.4 Navier Stokes equations in cylindrical coordinates

The assumptions of constant viscosity fluid, laminar, fully developed, incompressible flow are detailed in Figure 4.5.

$u_\theta = 0$	no swirling
$u_z = 0$	no flow between plates
$u_r = u_r(r, z)$	radial flow not a function of θ
$\dfrac{\partial u_i}{\partial t} = 0$	steady state
$F_i = 0$	no body forces

Figure 4.5 Flow assumptions

Flow assumptions and order of magnitude comparisons are used to cancel the majority of terms from the three Navier Stokes equations (Figure 4.6).

r axis :

$$\rho\left(u_r \frac{\partial u_r}{\partial r}\right) = -\frac{\partial P}{\partial r} + \mu\left(\frac{\partial^2 u_r}{\partial r^2} + \frac{1}{r}\frac{\partial u_r}{\partial r} - \frac{u_r}{r^2} + \frac{\partial^2 u_r}{\partial z^2}\right)$$

$$\frac{\partial^2 u_r}{\partial z^2} \gg \frac{\partial u_r}{\partial r}$$

order of magnitude comparison

$$\Rightarrow \quad \frac{\partial P}{\partial r} = \mu \frac{\partial^2 u_r}{\partial z^2}$$

θ axis :

$$\frac{\partial P}{\partial \theta} = 0$$

z axis :

$$\frac{\partial P}{\partial z} = 0$$

Figure 4.6 Reduced Navier Stokes equations

The theta- and z-axes flows are conservative; the r-axis flow can be solved for the flow profile (Figure 4.7).

Flow profile

$$\frac{\partial P}{\partial r} = \mu \frac{\partial^2 u_r}{\partial z^2}$$

$$u_r = \frac{1}{\mu} \iint \frac{\partial P}{\partial r} \partial z$$

$$u_r = \frac{1}{2\mu} \frac{\partial P}{\partial r} z^2 + c_1 z + c_2$$

Boundary conditions :

$$u_r(z = 0) = 0 \quad \rightarrow \quad c_2 = 0$$

$$u_r(z = h) = 0 \quad \rightarrow \quad c_1 = -\frac{1}{2\mu} \frac{\partial P}{\partial r} \frac{h}{2}$$

$$u_r = \frac{1}{2\mu} \frac{\partial P}{\partial r} z(z - h)$$

Figure 4.7 Flow profile for radial axis equation

The volumetric flow rate is the integral of the r-axis flow profile over the unit volume flow element (Figure 4.8).

$$Q = \int u_r dA$$

$$dA = r \cdot d\theta \cdot dz$$

$$u_r = \frac{1}{2\mu} \frac{\partial P}{\partial r} z(z - h)$$

$$Q = \int_{z=0}^{h} \int_{\theta=0}^{2\pi} u_r \cdot r \cdot d\theta \cdot dz$$

$$Q = 2\pi\, r \int_{z=0}^{h} \frac{1}{2\mu} \frac{\partial P}{\partial r} \left(z^2 - hz\right) \cdot dz$$

$$Q = \frac{\pi\, r}{\mu} \frac{\partial P}{\partial r} \left[\frac{z^3}{3} - \frac{hz^2}{2} \right]_{z=0}^{h} = \frac{\pi\, r}{\mu} \frac{\partial P}{\partial r} \left(\frac{h^3}{3} - \frac{h^3}{2} \right)$$

$$Q = -\frac{\pi\, r\, h^3}{6\mu} \frac{\partial P}{\partial r}$$

Figure 4.8 Volume flow rate

The pressure drop for a constant flow rate assumption can be integrated from the volumetric flow rate relationship. The resistance of the socket, defined as the change of pressure for a given change in volume flow, is used to characterize the socket (Figure 4.9).

$$Q = -\frac{\pi\, r\, h^3}{6\mu}\frac{\partial P}{\partial r} \qquad R_s = \frac{P_s}{Q}$$

$$\frac{\partial P}{\partial r} = \frac{-6Q\mu}{\pi\, r\, h^3} \qquad R_s = \frac{6\mu}{\pi h^3}\log_e\left(\frac{l_o + l_s}{l_o}\right)$$

$$\int_{P_s}^{P_a} \partial P = \frac{-6Q\mu}{\pi\, h^3}\int_{l_o}^{l_o+l_s}\frac{1}{r}\partial r$$

$$P_s = \frac{6Q\mu}{\pi\, h^3}\log_e\left(\frac{l_o + l_s}{l_o}\right)$$

Figure 4.9 Pressure drop and resistance profiles

The cylindrical coordinate assumption is valid for small gap sizes (h) related to the overall fluid flow distance (l_S). The joint dimensions (in spherical coordinates) must be converted to equivalent dimensions in cylindrical coordinates in order to properly represent the system (Figure 4.10). In particular, the orifice and socket arc lengths must be converted to linear distances based on the ratio of equivalent sphere–circle radii (Figure 4.10).

$\pi \cdot r_c^{\ 2} = \frac{2\varepsilon}{2\pi}4\pi \cdot r_s^{\ 2}$	equate circle surface area sphere surface area
$r_c = \sqrt{\frac{4 \cdot \varepsilon}{\pi}}\, r_s = \eta_r r_s$	equivalent circle radius
$h = h_0 + \delta \cdot \cos\alpha$	equivalent air gap at socket edge
$l_o = \eta_r \cdot r \cdot \phi$	equivalent radius to orifices
$l_s = \eta_r \cdot r \cdot (\phi - \alpha)$	equivalent length from orifices to socket edge
$A = \pi\left(r_s \cdot \sin\alpha\right)^2$	projected socket area

Figure 4.10 Equivalent socket dimensions in cylindrical coordinates

The required socket pressure drop (P_S) is determined by the preload force (F) which is the total preload force in the y-axis direction. Consequently, the area over which the force acts is the projected area (A) on the y-axis, rather than the surface area of the spherical surface over which the fluid flows. Given the socket pressure drop and resistance, the flow rate can be determined; as this is constant through both the orifices and the socket this determines the pressure drop over the orifices. The total pressure drop from the inlet pressure (P_i) to the outlet pressure (atmospheric) can be determined (Figure 4.11).

$$R_s = \frac{6\mu}{\pi h^3} \log_e \left(\frac{l_o + l_s}{l_o} \right) \qquad \text{socket resistance}$$

$$P_s = \frac{F_p}{\pi \left(r_s \sin \alpha \right)^2} \qquad \text{socket pressure}$$

$$Q = \frac{P_s}{R_s \cdot N_o} \qquad \text{inlet flow rate}$$

$$P_o = R_o \left(Q \right) \qquad \text{pressure drop across orifice}$$

$$P_i = P_s + P_o \qquad \text{inlet pressure}$$

Figure 4.11 Inlet pressure

For a given vertical displacement (δ), orifice resistance function (R_0), preload force (F) and joint dimensions (r_s, α, ϕ, h_0), the inlet pressure (P_i) can be determined. The pressure–displacement characteristics can then be measured and compared against the theoretical predictions.

The stiffness of the air gap is defined as the change in vertical displacement for a given applied force. The socket pressure drop is integrated over the projected socket area to obtain the force, which is differentiated with respect to the vertical displacement to obtain the stiffness. The resultant formulation, refer to Figure 4.12, reveals an inverse relationship between the stiffness and the vertical displacement.

$$P_s = \frac{6Q\mu}{\pi h^3}\log_e\left(\frac{r}{l_o}\right)$$

Pressure - flow relationship

$$h = h_0 + \delta\cos\alpha$$

Air gap - vertical displacement relationship

$$r = l_o + l_s$$

$$F = \int_A P_s\, dA$$

Integrate pressure over projected area

$$= \int_0^A \frac{6Q\mu}{\pi h^3}\log_e\left(\frac{r}{l_o}\right) dA$$

$$= \int_0^{2\pi}\int_0^r \frac{6Q\mu}{\pi h^3}\log_e\left(\frac{r}{l_o}\right) r\, dr\, d\theta$$

$$= \frac{3Q\mu}{h^3} r^2\left(2\log_e\left(\frac{r}{l_o}\right) - 1\right)$$

$$= \frac{k}{(h_0 + \delta\cos\alpha)^3}$$

$$k = 3Q\mu(l_o + l_s)^2\left(2\log_e\left(\frac{r}{l_o}\right) - 1\right)$$

Cubic stiffness coefficient

$$K_f = -\frac{dF}{d\delta} = -\frac{dF}{dh}\frac{dh}{d\delta}$$

Linear stiffness coefficient

$$= \frac{9Q\mu r^2\cos\alpha}{h^4}\left(2\log_e\left(\frac{r}{l_o}\right) - 1\right)$$

$$= \frac{3\pi r^2 P_s\cos\alpha}{2h}\left(2 - \frac{1}{\log_e\left(\frac{l_o + l_s}{l_o}\right)}\right)$$

Substitute socket pressure for flow

$$= \frac{3\pi(l_o + l_s)^2 P_s\cos\alpha}{2(h_0 + \delta\cos\alpha)}\left(2 - \frac{1}{\log_e\left(\frac{l_o + l_s}{l_o}\right)}\right)$$

Figure 4.12 Stiffness formulation

4.2.2 Preload Analysis

The preload design methodology developed for the point, rolling and sliding contact joints was applied to the fluid contact joint to optimize the placement of the magnets within the socket. As the dimensions of the air contact joint are identical to the sliding contact joint, a total of eight ½” (12mm) magnets are arranged at 45° to the vertical to provide a total preload force of approximately 100N as shown in Table 4.1. As with the sliding contact prototype, the socket angle (size of the socket) is chosen based on geometric constraints: the size of the ball and the size of the shaft. However this optimization reveals that an improvement in socket pressure is possible through a 15% reduction in the socket size.

TABLE 4.1 Preload design guide for fluid bearing joint

Socket Angle (deg)	Preload Force (N)	Preload Angle (deg)	Magnet Diam (mm)	Magnet Thickness (mm)	Cost ($)	Area Ratio (%)	Socket Pressure (atm)
72	83.7	54	12	6	8	29.4	0.2
54	86.4	36	12	6	6	29.4	0.3
63	86.4	36	12	6	6	25.2	0.3
72	86.4	36	12	6	6	22.0	0.2
72	100.7	45	12	6	8	29.4	0.3
63	**100.7**	**45**	**12**	**6**	**8**	**33.6**	**0.3**

Given the predicted preload force from the magnets, the socket pressure required to support the ball is determined from Figure 4.11. In order to minimize the power requirements for the operation of the joint, is desirable to minimize the pressure drop across the orifices. Typically, the orifice pressure drop is chosen to be similar to the socket pressure drop *[Slocum, 1992]* which would imply an orifice diameter of 0.003" (75μm). However, due to the low pressure drop (0.5 atm.) across the socket, this would require an inlet pressure of only 1 atmosphere. In order to measure the stiffness and fluid flow characteristics, it is necessary for the pressure set point to be higher, approximately 2.7 atm.; hence a smaller diameter orifice (0.002" or 50μm) was chosen. This predicts a vertical displacement of 38μm, corresponding to an air gap of 15μm, with a stiffness of 5.6N/μm and inlet pressure of 2.7 atmospheres, as detailed in Table 4.2.

TABLE 4.2 Fluid flow design guide for fluid contact joint

Design Characteristics						Pressure			
Disp (μm)	Air Gap (μm)	Preload (N)	Orifice Diam (μm)	Flow Rate (sccm)	Stiffness (N/μm)	Resistance Ratio	Socket (atm)	Orifice (atm)	Inlet (atm)
30	14.9	100.7	0.002	74.5	9.7	11.1	0.5	1.9	2.4
32	15.3	100.7	0.002	82.0	9.4	12.6	0.5	2.2	2.7
34	15.8	100.7	0.002	90.1	9.1	14.2	0.5	2.5	3.0
36	16.3	100.7	0.002	98.6	8.9	15.9	0.5	2.8	3.3
38	**16.8**	**100.7**	**0.002**	**107.7**	**8.6**	**17.7**	**0.5**	**3.1**	**3.6**
40	17.3	100.7	0.002	117.3	8.4	19.6	0.5	3.4	3.9
42	17.8	100.7	0.002	127.4	8.1	21.6	0.5	3.7	4.3
44	18.3	100.7	0.002	138.2	7.9	23.7	0.5	4.1	4.6
46	18.7	100.7	0.002	149.5	7.7	26.0	0.5	4.5	5.0
48	19.2	100.7	0.002	161.4	7.5	28.4	0.5	4.9	5.4
50	19.7	100.7	0.002	173.9	7.3	30.8	0.5	5.3	5.9

The design process flowchart for the fluid contact joint is summarized in Figure 4.13. Ranges for joint dimensions, required preload, magnet characteristics and orifice resistance data are supplied as input and the required inlet pressure and predicted joint stiffness are output. This enables various combinations to be compared and the optimal configuration chosen.

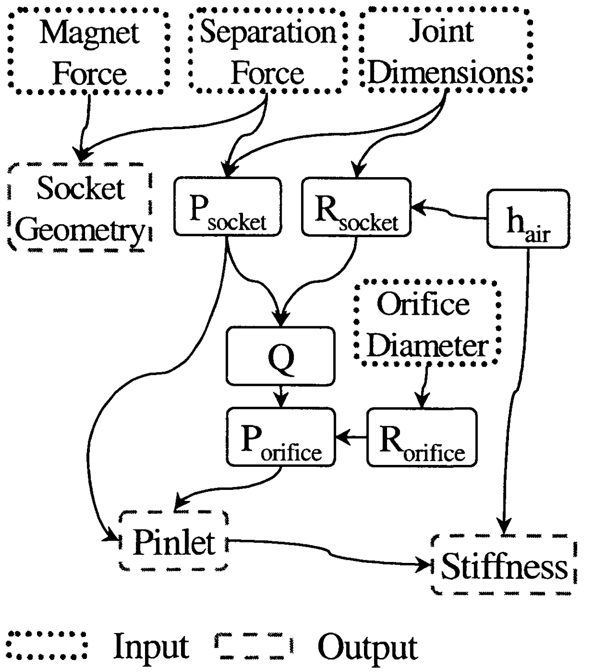
Magnet Force
Separation Force
Joint Dimensions
Socket Geometry
P socket
R socket
h air
Q
Orifice Diameter
P orifice
R orifice
Pinlet
Stiffness
Input
Output

Figure 4.13 Design flowchart for air bearing joint

4.2.3 Stiffness Analysis

The stiffness of the fluid film joint is characterized with a tensile testing machine. There are three primary regimes for the stiffness: magnet, fluid and contact (Figure 4.14). At a significant separation, the tensile tester load cell force is initialized to zero. As the ball approaches the socket, the magnet regime applies and the force will display an inverse parabolic profile. As the magnets are exerting a tensile force on the ball, the force as measured is positive.

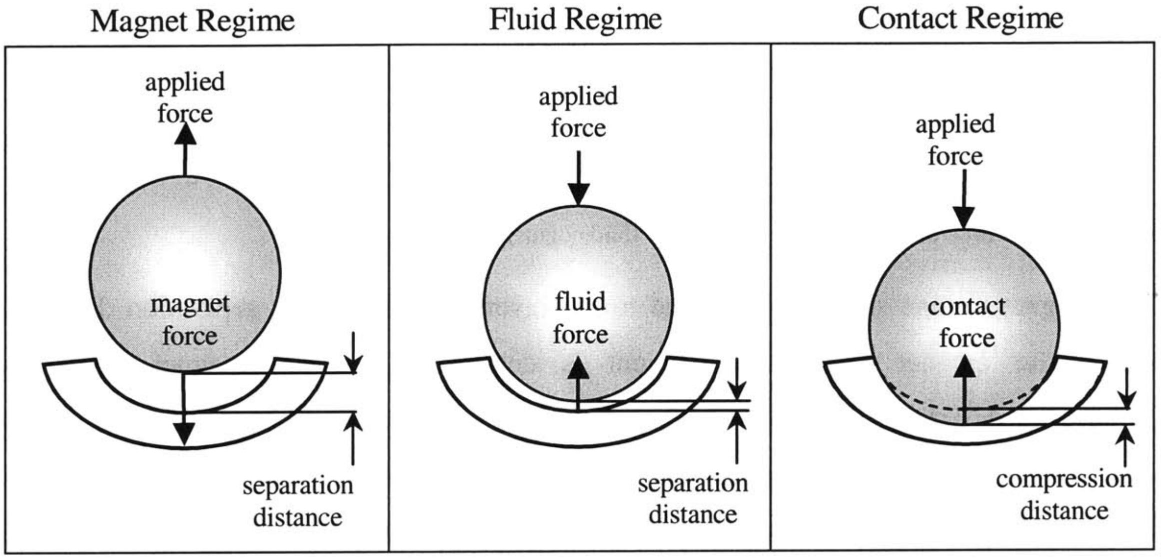
Magnet Regime
Fluid Regime
Contact Regime
applied force
magnet force
separation distance
applied force
fluid force
separation distance
applied force
contact force
compression distance

Figure 4.14 Magnet, air gap and contact stiffness regimes

The fluid regime represents the transition between the magnet and contact regimes and occurs at a separation of approximately 40 micrometers. At the point of contact between the ball and the socket surface, the force reaches its maximum tensile (positive) value – this represents the maximum preload force for the joint. Beyond the contact point, the contact regime applies and the force registered by the load cell is compressive (negative) and has a nominally linear profile. The tensile tester is retracted when the compressive force reaches a set point; refer to Figure 4.15 for a schematic of the three stiffness regimes.

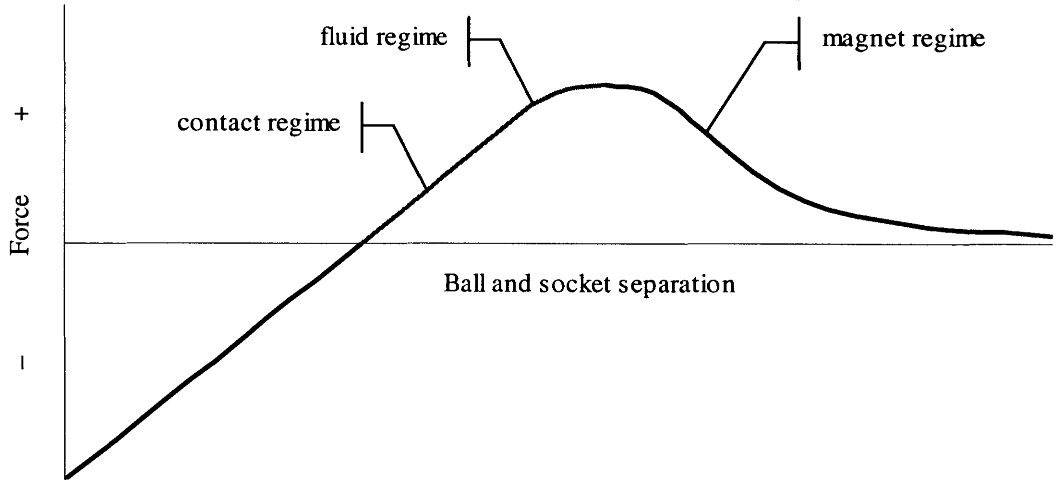

Figure 4.15 Force-displacement schematic for fluid contact joint

The magnet regime stiffness is related to the inverse square of the separation distance, where the magnet stiffness coefficient is determined by the magnet properties (Figure 4.16). Extension of the fluid flow model (Figure 4.12) reveals an inverse relationship between the force and the vertical displacement of the ball within the fluid stiffness regime (Figure 4.17). For a nominal vertical displacement of 53µm, this corresponds to a stiffness of 7.7 Newtons per micrometer. The stiffness of the contact regime is linear, with the stiffness parameter related to the elastic modulus of the epoxy replication material (2.4GPa *[Callister, 1994]*), as detailed in Figure 4.18. The predicted stiffness is 2700 N/µm. If the compression of the brass orifice mounting tubes is considered, the stiffness decreases to 140N/µm (Figure 4.19). The resultant contact stiffness is likely to lie within these two limits.

Magnet regime :

$$F = \frac{K_m}{x^2}$$

F : applied force

x : separation of ball and socket

K_m : magnet stiffness coefficien t

Figure 4.16 Magnet regime stiffness model

Fluid regime :

$F = K_f\, x$

F : applied force

x : vertical displacement $= 50\mu m$

$$K_f = \frac{2\pi(l_o + l_s)^2 P_s \cos\alpha}{h_0 + (\delta - h_0)\cos\alpha}\left(2 - \frac{1}{\log_e\left(\frac{l_o + l_s}{l_o}\right)}\right)$$

$$= \frac{144.4}{0.24\delta + 7.6}$$

$$= 7.3\,\frac{N}{\mu m}$$

K_f : linear stiffness (N/μm)

l_o : orifice arc length $= 11.5$mm

l_s : socket edge arc length $= 32.2$mm

P_s : socket pressure $= 0.5$atm

α : socket angle $= 76°$

h_0 : initial air gap $= 10\mu m$

Figure 4.17 Fluid regime linearized stiffness model

Replication material contact stiffness :

$F = K_{cr}x$

F : applied force

x : measured displacement

$$K_c = \frac{E_r A_r}{t}$$

K_{cr} : contact stiffness

E_r : elastic modulus $= 2.4$GPa

A_r : socket area

t : thickness $= 1.8$mm

$$A = \pi\, r_s^{\,2}$$

r_s : socket radius $= 25.4$mm

$$K_c = \frac{E\pi\, r_s^{\,2}}{t}$$

$$= 2700\frac{N}{\mu m}$$

Figure 4.18 Replication material stiffness model

Brass orifice housing contact stiffness :

$F = K_{cb} x$ F : applied force

x : measured displacement

$$K_{cb} = \frac{E_b A_b}{L}$$

K_{cb} : contact stiffness

E_b : elastic modulus $= 110\text{GPa}$

A_b : area of housing

L : thickness $= 10\text{mm}$

$A = \pi r^2$ r_b : housing radius = 2mm

$$K_c = \frac{E_b \pi r_b^{\,2}}{L}$$

$$= 140 \frac{N}{\mu m}$$

Figure 4.19 Brass orifice housing stiffness model

4.3 Manufacture

The fluid contact socket is machined in the same fashion as the existing sliding contact socket, using identical basic chassis and magnet mounting holes. Three tapped orifice holes are drilled at 20° to accept the orifice insert at one end and the tube connector at the other. The chassis with tubing and pneumatic connectors is shown in Figure 4.20.

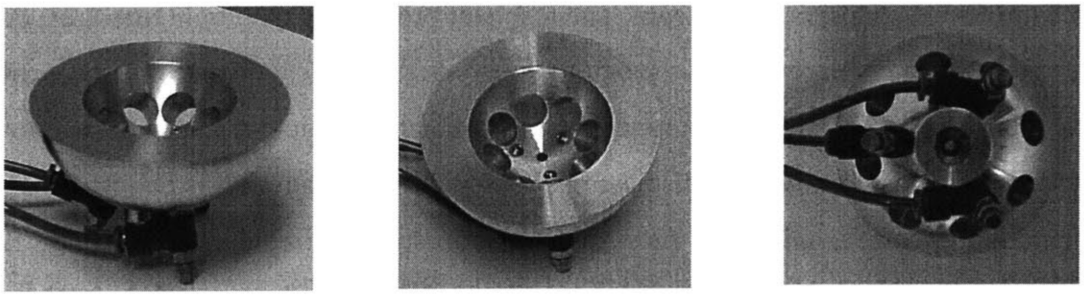

Figure 4.20 Air bearing chassis with pneumatic connectors

The replication process is slightly altered compared to the sliding contact ball and socket joint. Given the stringent requirements on the surface accuracy of the orifices and replicated surface, it is not possible to separate the ball from the socket by removing the orifices and prying the joint apart with a threaded screw. Instead, the ball is fitted with a ¼" (6mm) threaded shaft onto which is screwed a ½" (12mm) shaft. The ball can then be manually pulled apart without risk of damage to the orifices or replicated surface. The ball is furthermore coated with a wax compound to achieve an even surface coating approximately 10μm thick. A mold release is applied to the wax coating to allow the ball to be removed from the socket following replication. The same Teflon impregnated epoxy used in the surface-contact ball and socket joint is used as the replication material. The mold release and wax coating are removed and the replicated surface cleaned using mineral spirits. The resultant surface finish following replication is typically rougher than the sliding contact joint on account of the wax compound; furthermore, plastic deformation of the wax due to the high contact forces at the orifices may cause slight indentations in the replicated surface. These can be removed with fine grit sandpaper until a consistent flow is achieved.

4.4 Measurement

4.4.1 Fluid Flow Measurement

The critical dimension of the air bearing joint is the air gap between the socket and the ball. A coordinate measurement machine (CMM), accurate to 2 micrometers is used to measure the displacement of the center of the ball as the inlet pressure is increased from 0 to 6.8atm above atmospheric pressure. The resultant profile, detailed in Figure 4.21, compares the vertical displacement of the ball to the predicted vertical displacement described in Section 4.2.1. This indicates an underestimation of the vertical displacement at lower pressures, with higher pressures displaying a reasonable correlation. It is believed that the degradation in correlation at low pressures is due to surface irregularities affecting fluid flow at small gap sizes. For inlet pressures above 4.1atm, the measured and predicted agree to within 10% which is acceptable for a first order model.

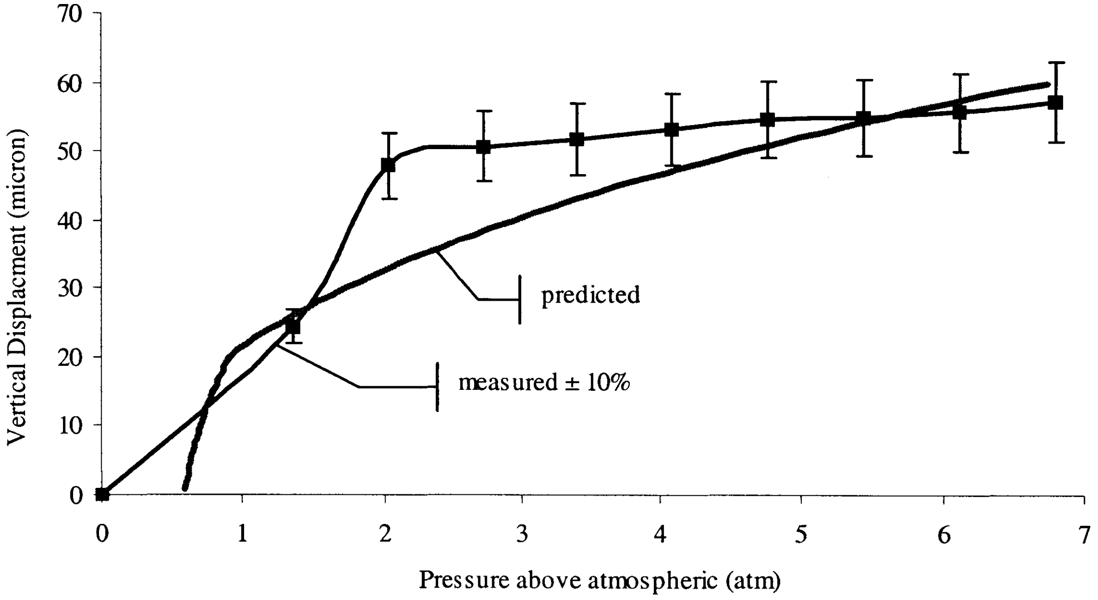

Figure 4.21 Vertical displacement as a function of inlet pressure

The air gap corresponding to the vertical displacement is primarily controlled by the ball and socket separation at the edge of the socket. The equivalent air gap versus pressure profile, detailed in Figure 4.22, reveals an asymptotic air gap of 20μm and an improved correlation between the adjusted CMM data and the model.

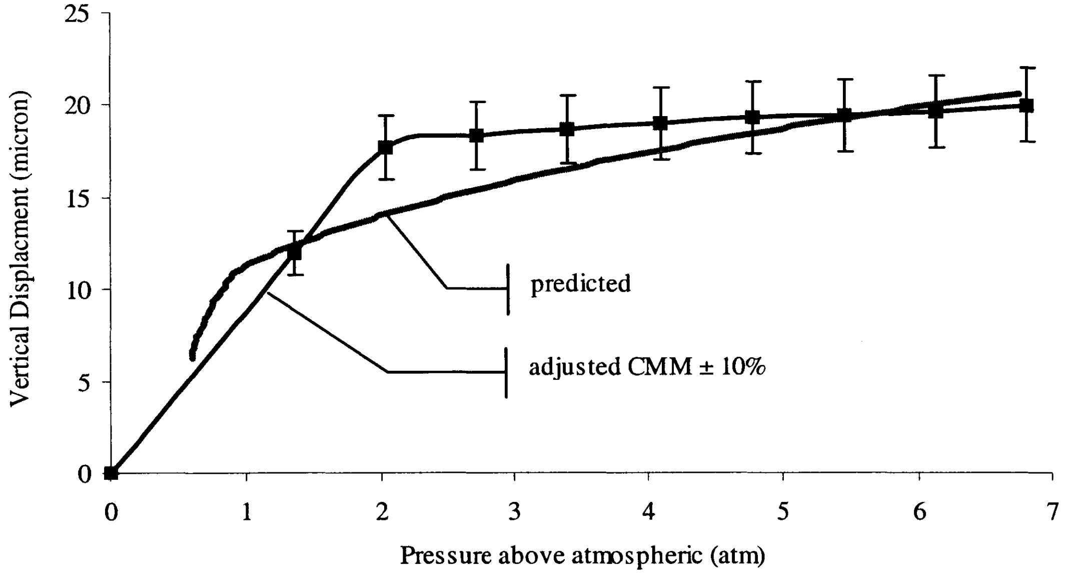

Figure 4.22 Predicted air gap as a function of inlet pressure

In order to improve the correlation between predicted and measured, the spherical Navier Stokes formulation could be used to model the physical system. Alternatively, the exit gap size (which is believed to be the primary flow restrictor) could be directly measured with capacitance probes and the gap size compared directly with the inlet pressure. Finally, the flow through the system can be measured in order to compare with the predicted flow.

4.4.2 Stiffness Measurement

A “Stable Micro Systems TA-XTPlus” texture analyzer *[SMS, 2003]* is used to determine the tensile characteristics of the ball and socket fluid contact joint, as shown in Figure 4.23. The load cell range is ±300N and an encoder at the base of the arm measures the displacement of the arm tip.

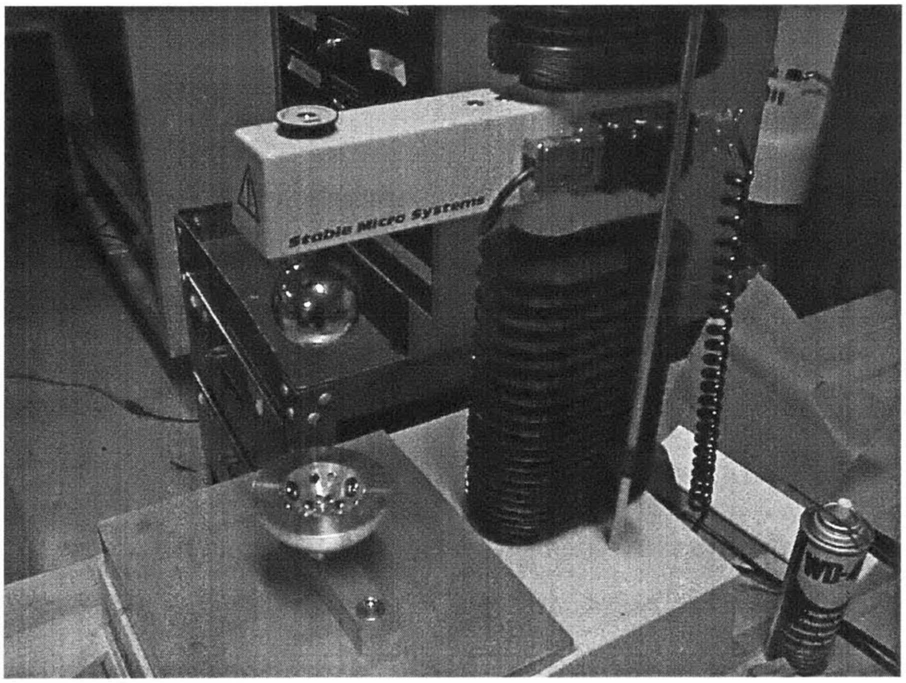

Figure 4.23 Texture analyzer mounted with socket and ball

The force-displacement curve is shown in Figure 4.24. The load cell is initialized to zero when the ball is sufficiently separated from the socket that the magnetic forces are negligible. The ball is brought into contact with the socket until a nominal compressive force of approximately 150N is registered. As the ball separates from the socket but remains in the linear elastic “contact” region, the force is linear with displacement. The point at which the ball makes contact with the socket (“separation”) defines the maximum preload force, which is approximately 90N, in agreement with the predicted preload forces and those measured for the sliding contact joint (refer to Figure 3.25). The magnet preload force produces a tensile force on the ball, resulting in a positive measured force (“magnet”). The relationship between the separation distance and applied force agrees with the inverse quadratic formulation (Figure 4.18).

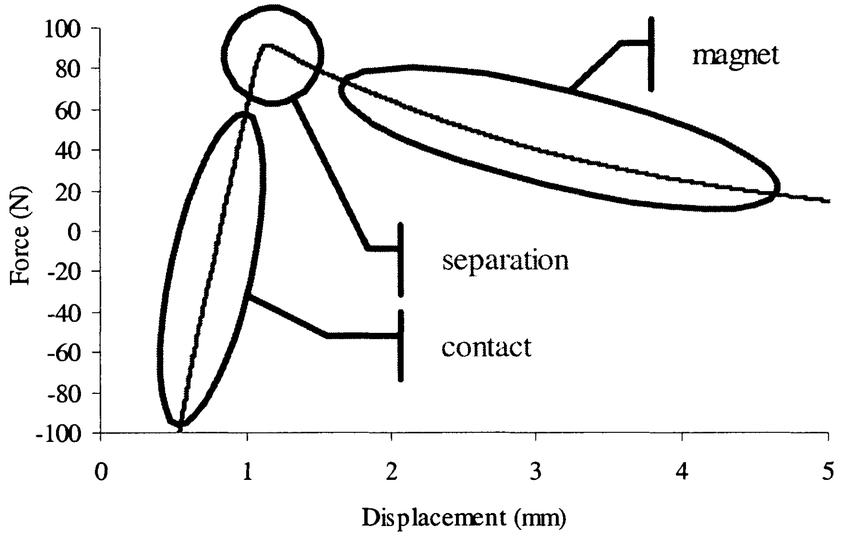

Figure 4.24 Force-displacement characteristics with encoder displacement data

However, the displacement scale indicates that the ball is pushed at least half a millimeter into the replication material, which is unrealistic for a material with a high elastic modulus. Clearly, deflection of the cantilevered arm of the tensile testing machine under the applied loads accounts for a significant proportion of the measured displacement. A static deflection test is performed wherein a beam is simply supported upon the joint and a roller and the deflection of the joint end measured using an extensometer. A deflection of approximately 10μm is observed for an applied 100N load, indicating a stiffness of 5N/micron (as the reaction force at the joint is 50N). In order to obtain a more accurate assessment of the ball displacement, the joint is mounted in a Zwick tensile testing machine *[Zwick, 2003]*. The relative displacement of the ball and socket is measured using an extensometer, and the force-displacement characteristics presented in Figure 4.25. The three regimes are distinguished based on the slope and form of the force-displacement characteristics. Additionally, there exists a region between the contact and fluid regime, where the force transitions between negative and positive, which causes a large displacement of approximately 50μm at a low stiffness. The contact and fluidic regimes are presented in Figure 4.26 and Figure 4.27.

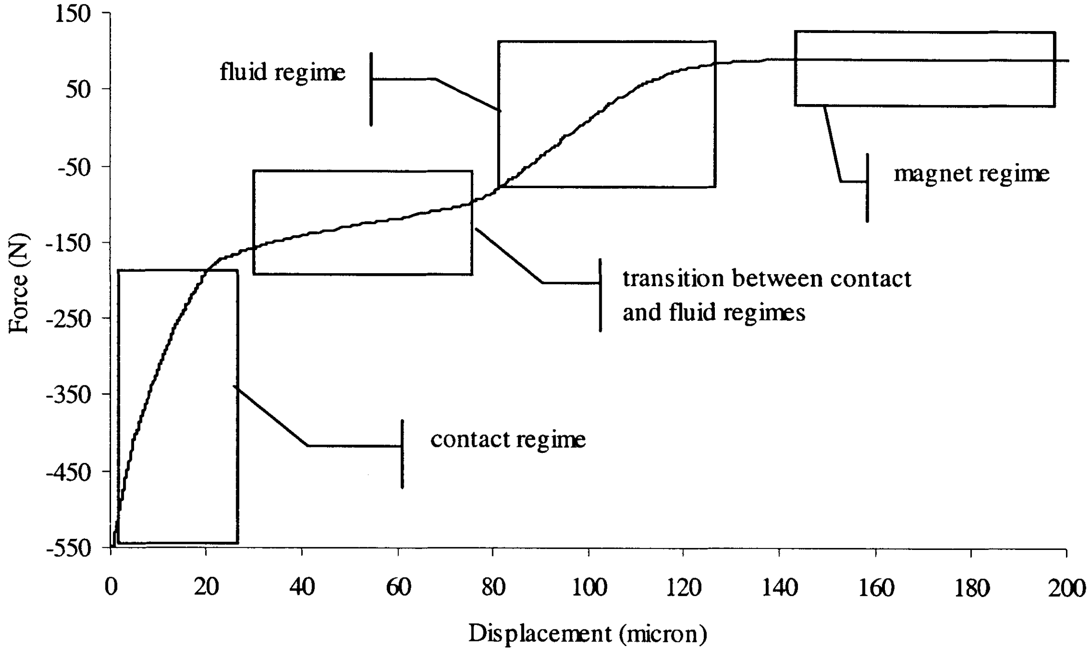

Figure 4.25 Extensometer force-displacement characteristics for tension cycle

The force-displacement characteristics yield the stiffness coefficients detailed in Table 4.3. The linearized stiffness in the fluid regime is determined to be 4.5N/μm which agrees relatively well with the predicted stiffness of 7.3N/μm. The contact stiffness is significantly lower than the predicted stiffness range determined from Figure 4.18. Both fluid and contact stiffness coefficients underestimate the predicted stiffness, due to an inherent flexibility in the mounting of the ball and socket. The presented extensometer data measures the displacement of the socket edge relative to the machine base. Separate measurements of the ball motion reveal a displacement that can be neglected compared to the socket motion. A more accurate stiffness estimate can be obtained through measurement of the displacement of the center of the ball relative to the socket edge, using a coordinate measurement machine.

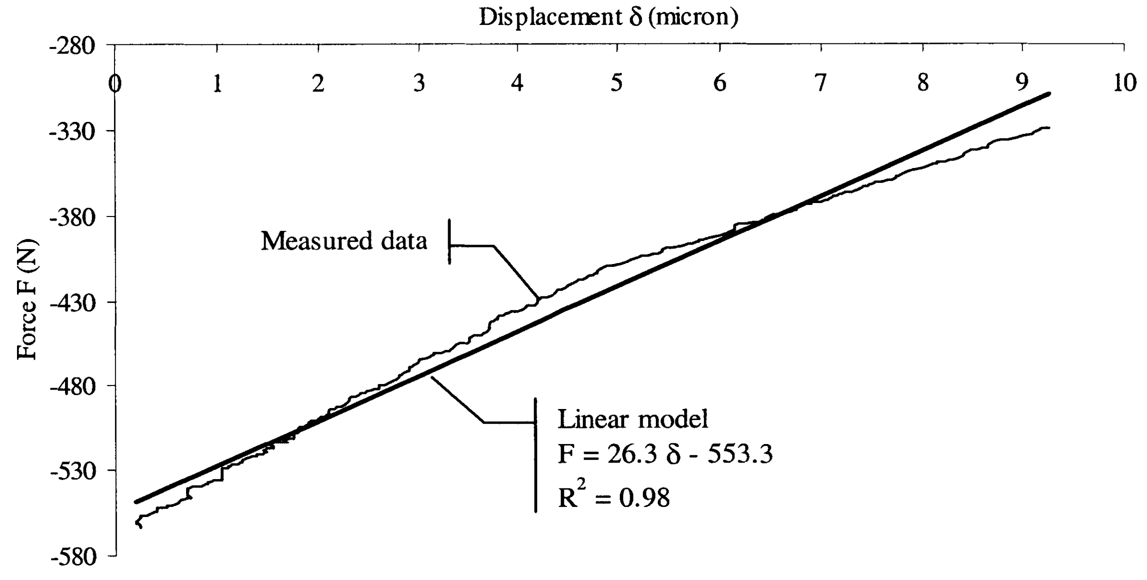

Figure 4.26 Contact region force-displacement characteristics

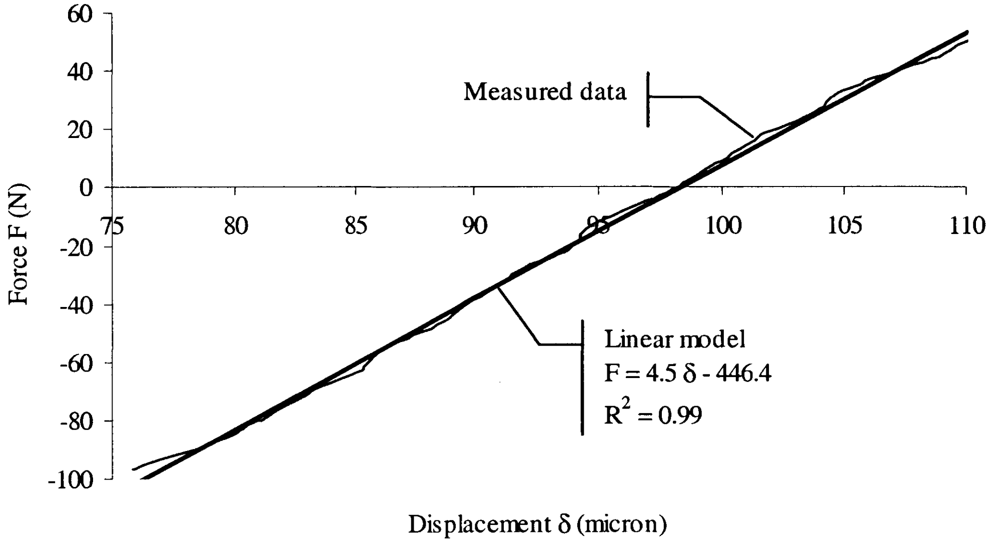

Figure 4.27 Fluid region force-displacement characteristics

TABLE 4.3 Stiffness coefficients for fluid and contact regimes

Regime	**Measured** (N/μm)	**Predicted** (N/μm)
Fluid Linear Stiffness (K_f)	4.5	7.3
Contact Linear Stiffness (K_c)	26	140 – 2700
Transition Stiffness	1.2	–

The transition region between the contact and fluid regimes displays a stiffness that is on the order of 1N/μm which is significantly lower than both the fluid and contact stiffness. A comparison of the tensile characteristics for no air and for a nominal air gap of 19μm is shown in Figure 4.28. This indicates that the contact and magnet regimes display the same stiffness, and that both profiles display a transition region of comparable stiffness. For the no air case, the transition occurs prior to the magnet regime when the ball and socket separate. For the air case, the transition occurs prior to the fluid regime, which also represents the point at which the ball and socket are no longer physically connected. The lower stiffness of this region is likely due to change from full surface contact between ball and socket to discrete sites of point contact due to the surface finish of the replicated socket. Furthermore, for the air case, this occurs before the air gap is able to form between the ball and socket. Due to lower area and Hertz contact stresses, the stiffness of a point contact is lower than a surface contact stiffness, which may explain the lower stiffness observed in this region.

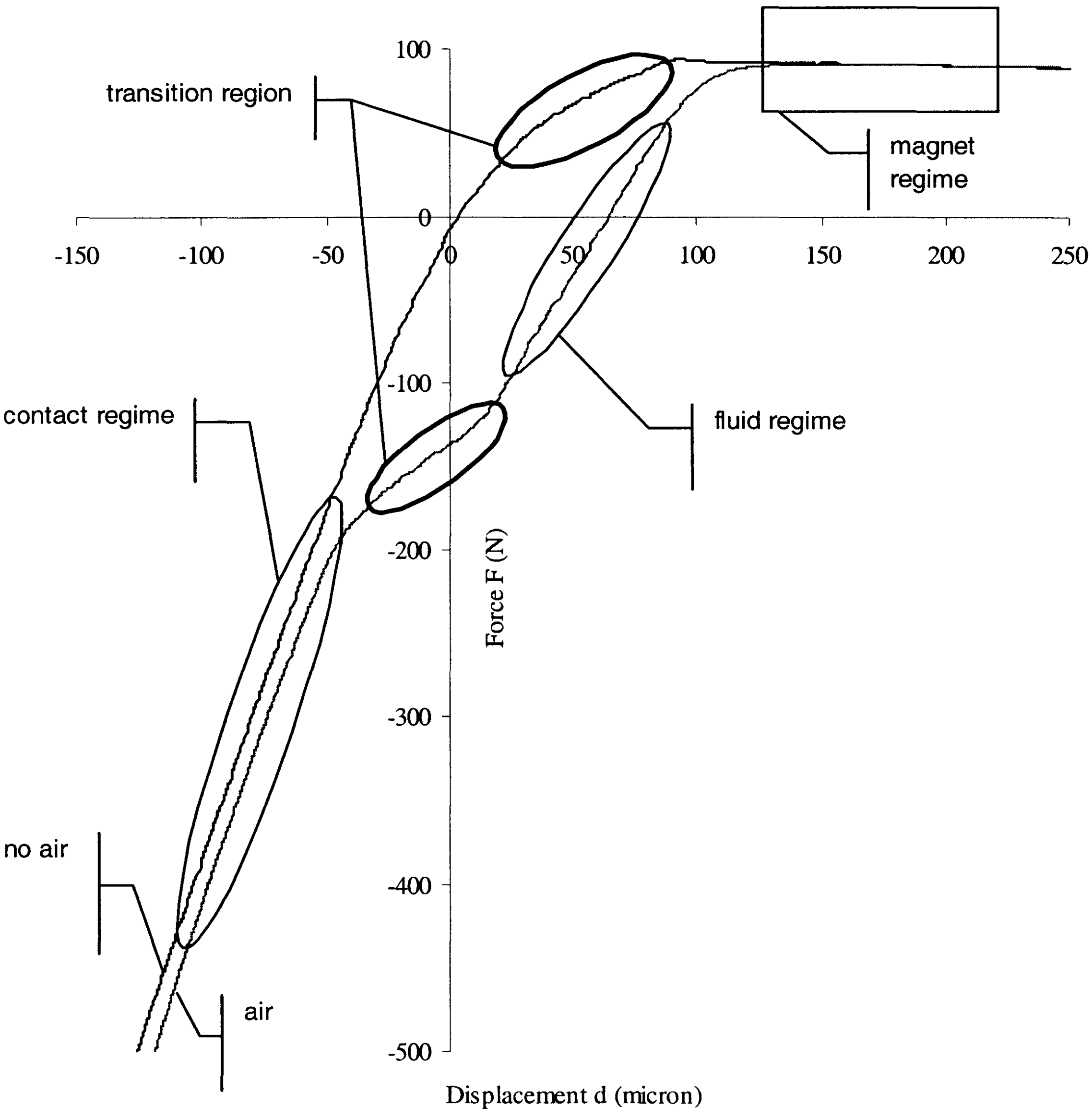

Figure 4.28 Force-displacement characteristics for air and no air

4.4.3 Accuracy Measurement

The accuracy distribution of the air joint with a vertical displacement of 50μm (corresponding to an air gap of 19μm) is detailed in Figure 4.29. The maximum residual error with the sphere fit algorithm is 16μm; kinematic calibration reduces this error to 11μm. These values are slightly higher than the rolling contact joint, due to the large air gap which may have caused a deflection of the ball center during the measurement process; as well as inaccuracies due to the manufacturing process.

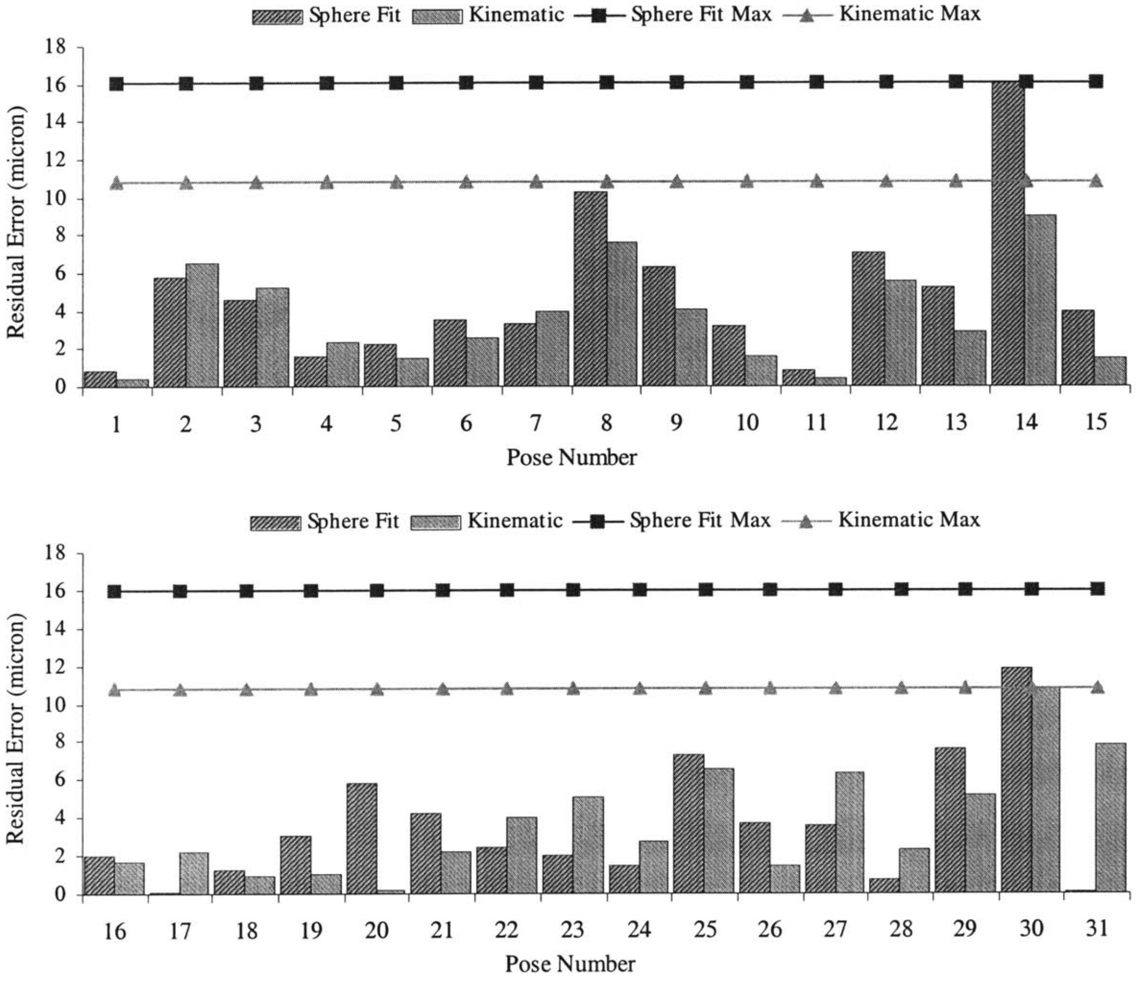

Figure 4.29 Fluid contact joint residual error distribution

4.4.4 Joint Comparison

The maximum and mean errors for each of the four prototype joints are presented in Figure 4.30. The fluid contact joint compares consistently with the other three prototypes; the higher maximum error is due to slight inaccuracies in the replication process which could be improved through the use of a dedicated replication sphere of diameter ten micrometer larger than the nominal ball diameter.

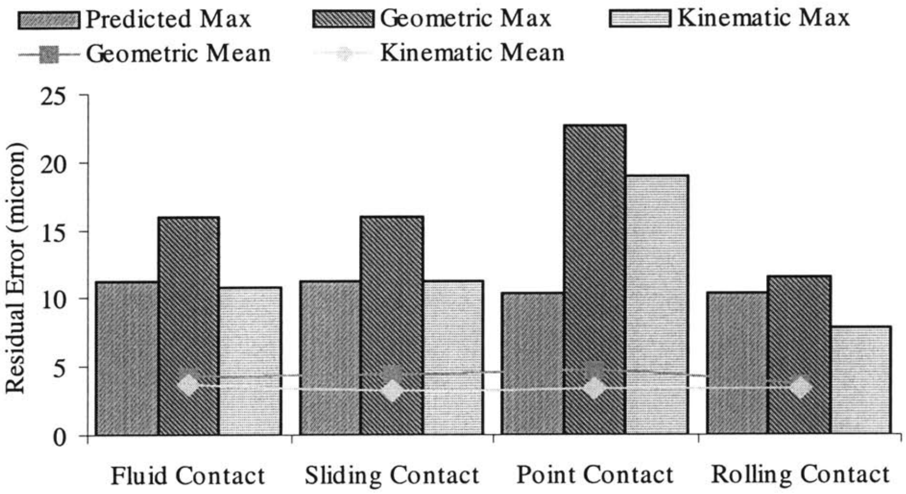

Figure 4.30 Maximum and mean residual errors for joint prototypes

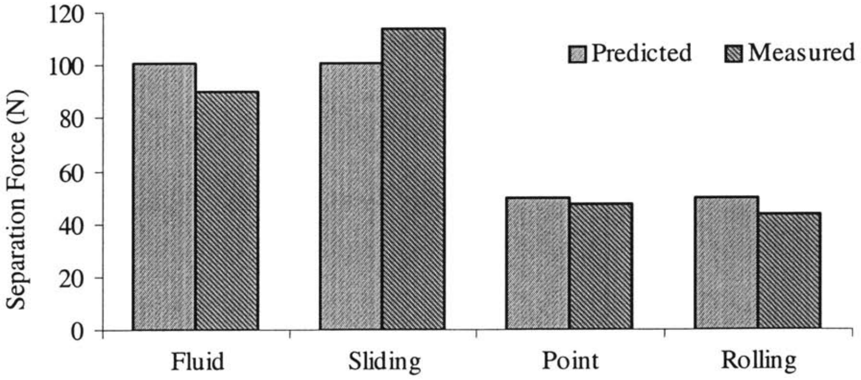

Figure 4.31 Predicted and measured preload forces

The predicted and measured preload forces are summarized in Figure 4.31. The fluid contact joint preload is the same as for the sliding joint, however the measured values differ slightly. The measured preload force for the fluid contact joint (shown for an inlet pressure of 4.1 atm.) is lower than the predicted as a result of the air gap, which increases the ball to socket separation and hence decreases the preload force.

4.5 Conclusions

The spherical air joint has been approximated by a first order flat plate model in order to predict the pressure and displacement characteristics. For high pressures, corresponding to an air gap greater than 15 micrometers, the model agrees with measurements to within 10%. This is sufficient to allow first order predictions of joint fluidic performance. However, the agreement between measured and predicted for low pressures, corresponding to an air gap less than 15 micrometer, is only to within 20%. It is believed that the predominant cause of this discrepancy is the replication surface finish. Due to deformation of the wax interface layer and irregularities in the mold release, the surface is not as precise as the surface finish seen on the sliding contact prototype. The replication process could be improved through the use of a dedicated replication ball that is sized to be 10μm larger than the desired ball diameter. This would ensure a repeatable and smooth gap size and surface finish, thereby improving the low pressure joint characteristics.

The stiffness characteristics are consistent with the predicted data for the fluidic region, as described by the flat-plate Navier Stokes approximation, yielding a stiffness of approximately 5 N/micrometer. The stiffness of the contact region is lower than predicted; potentially due to flexibility in the tensile testing machine, or due to Hertz contact deformations resulting is greater than anticipated displacements for a given force. The fluid contact joint accuracy is comparable to the rolling contact joint, displaying a maximum error of 16 micrometer un-calibrated and 10 micrometer when calibrated. This is slightly higher than predicted, due to the innacuracies inherent in the replication process and the corresponding larger than anticipated fluid gap. Improved control of the replication process and resultant surface finish should result in a smaller operating gap and an improved overall accuracy. The joint motion also displays some damping, due in part to the viscosity of air in a small gap as well as some hysteretic damping from the magnet preload arrangement. The Navier-Stokes model can be extended to model fluidic damping and compared to hydrodynamic viscosity tests.

Chapter 5

ADVANCED MODELING

5.1 Overview

The calibration models and techniques developed for the analysis of the spherical joint prototypes can be extended to generic multi-axis manipulators. Comparison to existing measurement and calibration results serves to validate and verify the predicted results of the simulation models, and defines a generic modeling framework for modeling and improvement of multi-axis kinematic mechanisms. The ABB IRB6400R robot (Figure 5.1) is chosen due to the significant amount of kinematic and measurement data available.

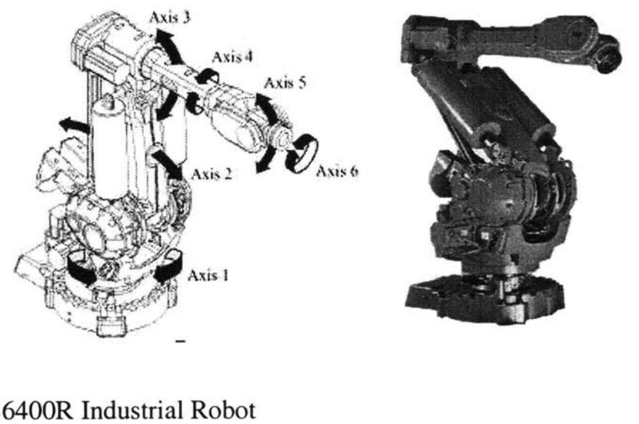

Figure 5.1 ABB IRB6400R Industrial Robot

The algorithms developed for the improvement of the robot manipulators is used to improve the joint kinematic models with the goal of reaching a maximum calibrated error on the order of several micrometers.

5.2 Genetic Programming Based Model Improvement

This section is taken from a paper presented to the International Symposium on Robotics and Automation, *[Robertson et al, 2002].*

Existing robot calibration models are derived through inspection of the primary physical properties of the manipulator structure. This is a powerful technique for the modeling of common effects such as gearbox flexibility and manufacturing tolerances. However, in situations where the accuracy level achieved by these models is insufficient for the required task, it is difficult to determine the nature of the remaining errors. In this paper, Genetic Programming is used to evolve equations that describe these un-modeled phenomena. These equations are used to identify the location and form of potential improvements to the existing calibration model. Improved models are implemented in an existing calibration simulation, resulting in a significant improvement in the simulated robot positional accuracy.

Two Genetic Programming representations – linear sequence and binary tree – are implemented to evolve the equations from a set of basic mathematical operators. The merits of each representation are discussed and a suitable evolution structure proposed. An iterative design framework is presented for the investigation and development of physical models for implementation in mechanical modeling problems.

5.2.1 Introduction

High accuracy industrial manipulators are required for many applications such as automated inspection and spot welding of car bodies. Current applications demand an accuracy of better than 1mm in the entire robot workspace; however, future applications are expected to target accuracy levels of 0.1mm. Typically, physically based representations are used to create kinematic models of the key error sources, such as flexibility of gearboxes, manufacturing tolerances and transmission errors *[Bernhardt et al, 1993]*, *[Shröer et al, 1997]*. The robot end effector position is measured using a high accuracy (10μm/m)

Leica laser tracker *[Leica, 2002]*. A numerical Jacobian and linear regression solver are then used to determine the robot-specific error parameters. While this technique has been successful in satisfying current demands, extending these models to the future targets requires the implementation of additional error models. The development of such extended error models by inspection is difficult as the source of the errors is typically not known, and may vary between different robot structures.

The goal of the proposed design framework is to obtain insights into the underlying physical phenomena in order to be able to derive an improved calibration model. Initially, three options were considered: Artificial Neural Networks (ANN), Genetic Algorithms (GA) and Genetic Programming (GP). Neural networks have been successfully implemented in robot–based problems *[Yoneda et al, 1990]*, however it is typically difficult to interpret the ANN to obtain insights into the underlying physical phenomena. Genetic Algorithms have been used in place of the linear regression solver to determine appropriate error parameters *[Wright, 1991]*, however they were deemed too inefficient for the purposes of function optimization. Genetic Programming has proved to be effective in the evolution of physically based organisms by Simms *[Simms, 1994]*; the design of optimal control solutions by Koza *[Koza et al, 1997]*; and the modeling of evolutionary systems by Ray *[Ray, 1992]*. In these implementations, a set of operators is defined and their optimal arrangement determined through an evolutionary process.

A framework is presented for the investigation and development of physically based mechanical models. Section 5.2.2 presents the two Genetic Programming representations, binary tree and linear sequence. A set of suitable mathematical operators is chosen and equations are evolved based on measured robot data. In Section 5.2.3, the validity of the results is demonstrated by investigating the set of inputs and the operators used in the equations. It is shown that certain inputs and operators are consistently used, pinpointing that these primary phenomena should be considered in the development of a new physical model. Two new models are proposed, and implemented in the existing calibration simulation, resulting in a 50% improvement of maximum robot error. Finally, in Section 5.2.4, a Genetic Programming design framework is discussed.

5.2.2 Implementation

The GP algorithm must evolve a sequence of operators that can improve the positional accuracy of the robot. This can be achieved in two distinct ways: altering the joint angles; or altering the position, where the joint angles are the inputs to the kinematic model and the position is the output. Altering the joint angles requires the implementation of the kinematic model within the GP algorithm, which increases the complexity of the system. Therefore, the Cartesian output of the existing kinematic model is altered and the results are compared with existing measurement data to provide an accuracy, or fitness, feedback (refer to Figure 5.2).

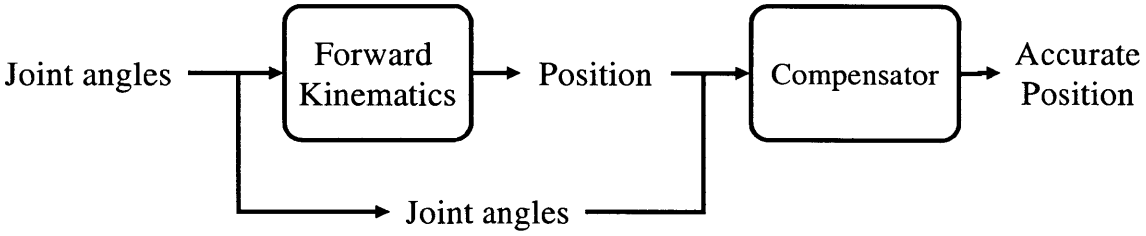

Figure 5.2 Compensator model

Applying standard Evolutionary Algorithms, appropriate equations are chosen based on their fitness and new equations created through a process of crossover and mutation:

```
initialize population with random individuals
loop for number of generations
    evaluate fitness function
    exit if fitness is less than threshold value
    sort population by fitness
    loop for entire population
        select two individuals with high fitness
        crossover and mutate to produce new individual
        add new individual to new population
    end population loop
    replace old population with new population
end generation loop
```

The list of available operators is detailed in Table 5.1. Through an iterative process, these operators were found to be relevant to the problem at hand. These operators are well scaled (the output is of the same order of magnitude as the input) and well behaved (most inputs can be accepted without numerical complications).

The two GP representations – linear sequence and binary tree – can access an input array, with joint angles, position and some predefined constants (Table 5.1). The sequence of operations and operands must then construct constants based solely on the input data, requiring no additional calibration parameters. This ensures that the evolution creates a mathematical representation of the problem at hand rather than a numerical approximation.

TABLE 5.1 Mathematical operators and input registers

Code	Op	Code	Op	Element	Property	Element	Constant
0	input	9	max	0	x	9	1.E-06
1	load	10	abs	1	y	10	1.E-05
2	store	11	square	2	z	11	1.E-04
3	add	12	sqrt	3	J1	12	0.001
4	subtract	13	not	4	J2	13	0.01
5	multiply	14	sin	5	J3	14	0.1
6	divide	15	cos	6	J4	15	1
7	modulo	16	tan	7	J5		
8	min	17	atan	8	J6		

Linear Sequence

The linear sequence implements a fixed-length array of operators and operands. Single parameter commands (*cos*, *not*, etc.) take an input from the accumulator and return a result back to the accumulator. Double argument commands (*add*, *sub*, etc.) reference a register for the second argument. Additionally, elements in the input array can be loaded into the accumulator using the *input* command. Registers are local arrays of data that can be used by the sequence, but are not saved. The effectiveness of the evolution improves as the population and sequence sizes increase, however there is a trade-off with the computational speed and memory requirements. Typically, a sequence size of 160 elements was used with a population size of 64K. The selection, crossover and mutation rates (refer to

Figure 5.3) were determined to be in the range 1% to 5%, as is typical of most evolutionary algorithms *[Jefferson et al, 1991], [Bäck et al, 1993].*

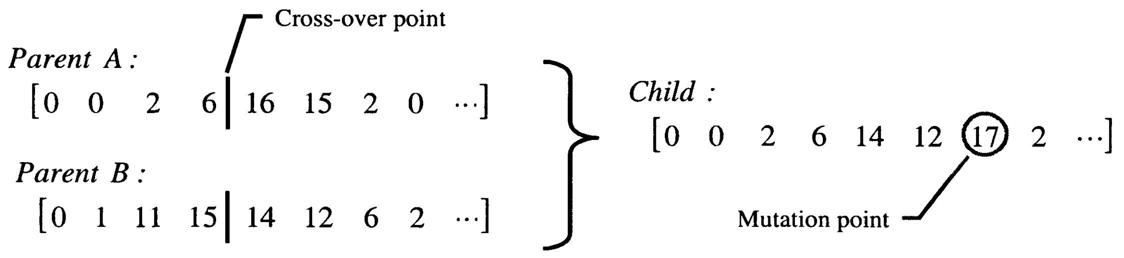

Figure 5.3 Cross over and mutation for linear sequence

A sequence and corresponding operations is presented in Figure 5.4. The first element (0) represents the *input* operator and the second (0) references an input register i_0. Hence, i_0 (x-coordinate) is loaded into the accumulator ($acc = i_0$). The next operators (2 6) store the accumulator in register r_6 ($r_6 = acc$), and so on. There are no loops or branch statements, and the sequence exits after the last operator.

Sequence :

$[0 \;\; 0 \;\; 2 \;\; 6 \;\; 16 \;\; 15 \;\; 4 \;\; 6 \;\; \cdots]$

Subsequenc e operations :

$[0 \;\; 0]$ $acc = i_0$

$[2 \;\; 6]$ $r_6 = acc$

$[16]$ $acc = \tan(acc)$

$[15]$ $acc = \cos(acc)$

$[4 \;\; 6]$ $acc = acc - r_6$

$\vdots$

Figure 5.4 Linear sequence and equations

A measured robot position and joint angle vector comprise the inputs to the sequence. Typically, 90 such positions are chosen, spaced evenly throughout the workspace. For each point, the fitness evaluation function compares the r_0 register element with the x measurement, r_1 with y and r_2 with z. The final fitness is the maximum Euclidean norm over all the training points, shown in Figure 5.5.

$$Fitness = \underset{i}{Max}\left(\sqrt{(x_i - r_0)^2 + (y_i - r_1)^2 + (z_i - r_2)^2}\right)$$

x_i, y_i, z_i : measuremen t points (i = 1...n)

r_0, r_1, r_2 : output registers

Figure 5.5 Fitness function

Binary Tree

The binary tree implementation uses Koza–style crossovers and mutations *[Koza, 1990]*. Each node corresponds to either an operation or a register depending on its position in the tree. All leaf nodes refer to register elements and all parent nodes correspond to a specific operation. The binary tree representation ensures that each operator in the tree always has access to the correct number of inputs. An operator that uses only one input uses the value returned by the left child and ignores the right child. The size of the tree increases exponentially with the depth, and is typically set between 10 and 15 in order to optimize system performance. During evolution, two parents are chosen from the high-fitness proportion of the population. Either crossover or mutation is performed, chosen at random based on their relative probabilities. The crossover operator uses one crossover point and ensures the convergence of the algorithm. The sequence of operations is described as follows and illustrated in Figure 5.6.

1. Randomly select a crossover point within the first parent.

2. Copy, from the first parent to the child, all the nodes between the root and the generated crossover point. The nodes are numbered using a depth-first traversal.

3. Copy into the child all the nodes between the crossover point (excluded) and the end of the second parent. If the size of the second parent is smaller than the crossover point then no nodes are copied.

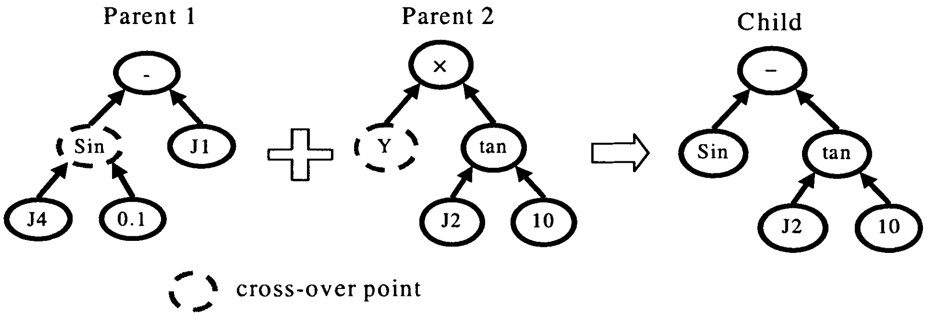

Figure 5.6 Binary tree crossover

Two types of mutation, structure and operator, are implemented. Structure mutation is a variation of the crossover operator. Instead of copying the second parent into the child at the crossover point, a new crossover point is randomly chosen in the second parent, and all subsequent nodes copied to the child. This type of mutation allows the reuse of entire sequences of operations. Operator mutation involves randomly selecting a node in the child tree and randomly changing its operator. The root node of the tree returns a single value, hence a separate tree is required for each of the x, y and z coordinates.

5.2.3 Results and Analysis

Linear Sequence Results

The linear sequence algorithm is evolved on 40 of the 90 measurement points, resulting in the fitness versus generation profile as shown in Figure 5.7. The initial value of 1.3mm represents the error of the current kinematic error model and the final value of 0.6mm represents the error on the taught points after applying the sequence equations.

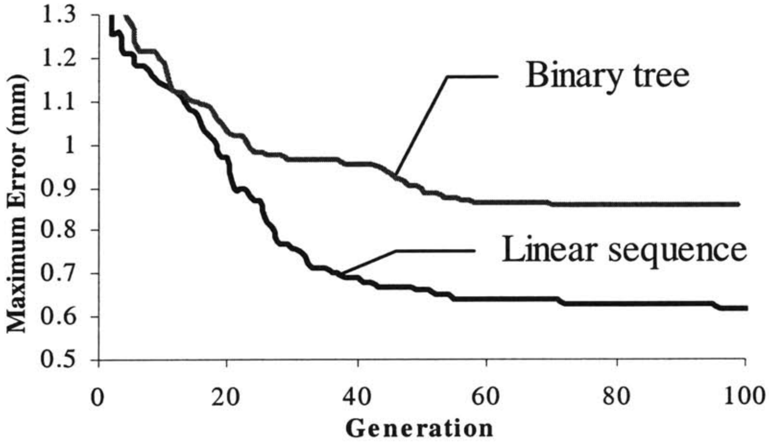

Figure 5.7 Fitness vs. generation

Simulations have shown that the extrapolation of the evolved linear sequence on the 50 remaining points results in a maximum error larger than the original error of 1.3mm (Figure 5.8). This is due to the inherent inability of the solution evolved by the evolutionary algorithm to extrapolate, as the solution is optimized for the specific input dataset *[Jefferson et al, 1991]*. Therefore, it is not possible to directly implement the evolved equations in the existing models; rather a physical model must be deduced from the evolved equations.

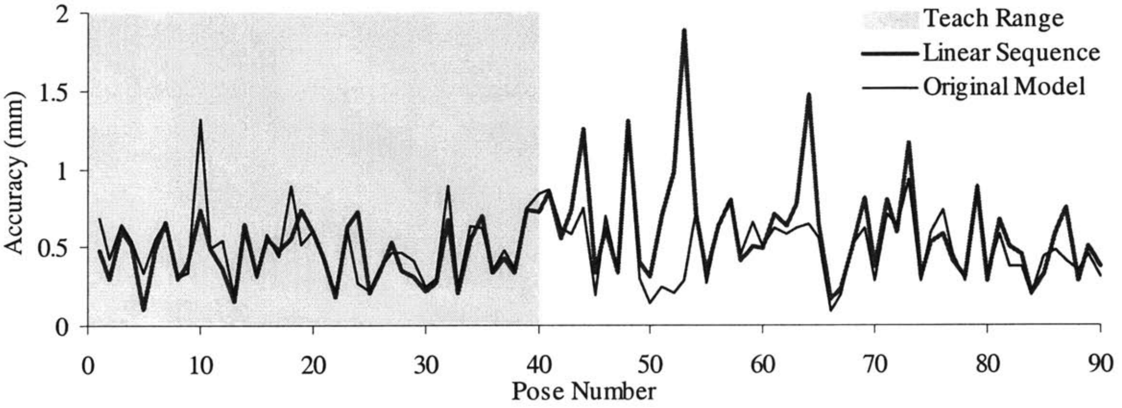

Figure 5.8 Extrapolation of linear sequence

Binary Tree Results

The evolution of the binary tree equations on the same 40 points as for the linear sequence results in a maximum error of 0.9mm (Figure 5.7). The resultant tree reveals a structure with the input coordinate on one branch of the root node and an evolved constant on the other. The evolved–constant branch is typically deep and narrow, similar to the linear sequence, but limited by the maximum depth of the tree. As the depth of the tree is significantly smaller than the length of the sequence, the tree is unable to evolve equations of sufficient complexity to further reduce the error. As the size of the tree increases exponentially with depth, there is a trade-off between performance and computing limitations.

Analysis

A histogram of the input variables referenced in several simulations using data from the standard model highlights three cases that warrant investigation (refer to Figure 5.9):

- Case 1: joint independent errors (XYZ)
- Case 2: joint-5 dependent errors (J5)
- Case 3: joint-1 dependent errors (J1)

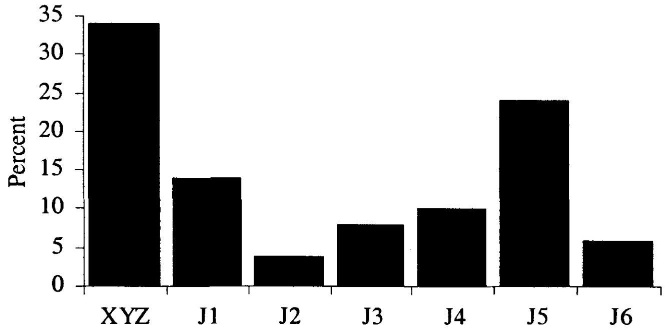

Figure 5.9 Histogram of referenced inputs for standard model

An equation, derived from the linear sequence evolution and representing the joint independent phenomenon (case 1), is chosen for further investigation (Figure 5.10). The sequence has been trimmed to remove operations that do not contribute to the final solution and simplified. Furthermore, for the presented results, only operators that are continuous in the first derivative were used, in order to ensure good performance of the linear–regression solver. The equations show that a generic constant (α) is applied for each of the x, y and z compensations. Each coordinate is furthermore transformed using non-linear operators.

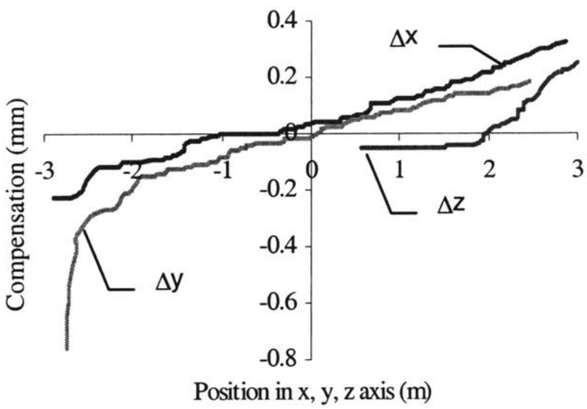

$$\Delta x = -\alpha + \left| \left(z_{in} + \Delta z + x_{in}\right) \cdot \left(10^{-4} - \alpha\right) \right|$$

$$\Delta y = -\alpha + \left| \frac{\left(\beta - y_{in} + \alpha\right) \cdot \left(10^{-4} - \alpha\right)}{y_{in} - \alpha} \right| \cdot \left(x_{in} - \alpha\right)$$

$$\Delta z = \alpha + z_{in} \cdot 10^{-5} - 10^{-4}$$

$$\alpha = \operatorname{atan}\left(\sqrt{\cos\left(\operatorname{atan}\left(z_{in}\right)^{2}\right)}\right)^{32} + 3 \cdot 10^{-5}$$

$$\beta = \cos(\tan(1))$$

Figure 5.10 Linear sequence compensation and equation

Design of Physical Model

In order to develop an improved physical model, the compensation vectors Δx, Δy and Δz are analyzed as functions of the robot position. The Δx and Δy characteristics are particularly interesting as they are linear in a large portion of the workspace (Figure 5.10) – when the robot is further out in the workspace, a greater compensation is required. From this information, it is deduced that this phenomenon could be modeled as a torsion spring system at the base of the robot.

The base compliance model was implemented by calculating the reaction torques at the base of the robot multiplied by a torsion-spring parameter, resulting in an angular deflection about the x- and y-axes. The performance of the derived model is presented in Figure 5.11.

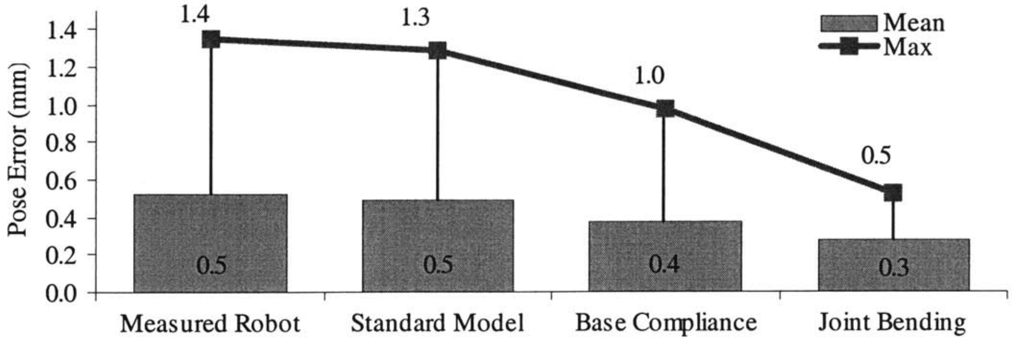

Figure 5.11 Comparison of calibration models

The *Measured Robot* result represents the actual robot accuracy, using the best available calibration model, implemented in the robot controller and measured using the Leica laser tracker. The *Standard Model* is an offline simulation of the controller model and is used as a test platform for the rapid development of new physical models. The measured and simulated maximum errors are consistent to within 5%, indicating that the simulated model can be used to predict the actual robot accuracy. The *Base Compliance* model implements the base compliance phenomenon in the simulation environment, resulting in an improvement of 25% in both the mean and maximum errors. The *Joint Bending* model investigates the joint-5 dependent errors (case 2). It is modeled as a torsion spring about axis 5, in the same fashion as the base compliance model. The resultant maximum error decreases to 0.6mm, representing an improvement in the maximum error of over 50% compared to the standard model. The greater relative reduction of the maximum error compared to the mean error is consistent with the use of the maximum operator in the fitness function.

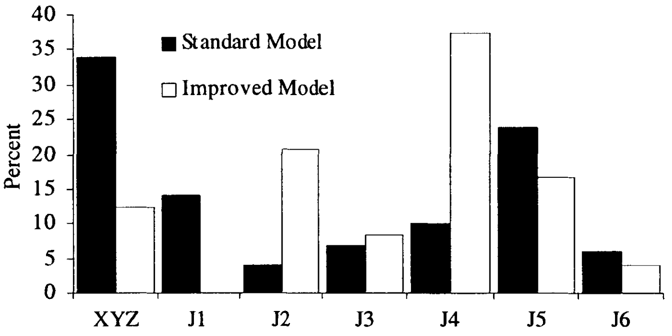

Figure 5.12 Histogram of referenced inputs for improved model

The histogram of referenced inputs following the implementation of the improved model (base compliance and joint bending) is shown in Figure 5.12. The reduction in relative influence of joint independent (XYZ) and joint-5 dependent (J5) errors confirms the validity of the improved model. Furthermore, the histogram suggests that the next model improvement should focus on joint-4 dependent (J4) errors.

5.2.4 Framework

A Genetic Programming framework for the development of physically based mechanical models is presented as a six-step iterative process.

1. Select a set of operators that are appropriate to the problem at hand. Issues of scalability and continuity should be considered, and intuition about the physics of the problem can be used to select suitable operators.

2. The choice of implementation should be made based on the type of expected solution. Solutions that require few operations on many inputs would benefit from the tree representation. For cases where many operations are performed on few inputs, the linear sequence is more appropriate.

3. Selection of appropriate evolutionary parameters – crossover, mutation and selection probabilities – can be determined experimentally. A wise choice of

parameters can dramatically improve the performance, in terms of execution time and final fitness.

4. Through simulation and statistical analysis of the distribution inputs and operators used, determine the important physical phenomena to be modeled.
5. Study the behavior of the evolved equations in terms of the phenomena to be modeled. Plot the relationship between the fitness and the critical input parameters. Develop hypotheses about which physical phenomena could cause the observed behavior.
6. Implement a physically based model in the simulation environment and assess the performance.

It is important to note that prior expectations about the desired solution are required in such applications. Furthermore, conventional physical modeling should be performed using classical techniques in order to produce an initial fitness that is close to the required level of accuracy. The combination of modeling experience and Genetic Programming can considerably aid the engineer in the modeling of complex mechanical systems.

5.3 Spherical Joint Models

The Genetic Programming framework of Section 5.2.4 is applied to the rolling contact joint in order to improve the accuracy distribution. The Linear Sequence implementation was used with the operators detailed in Table 5.1. The mutation and cross-over rates were set at 1% and the selection rate at 5%. The referenced inputs histogram is shown in Figure 5.13.

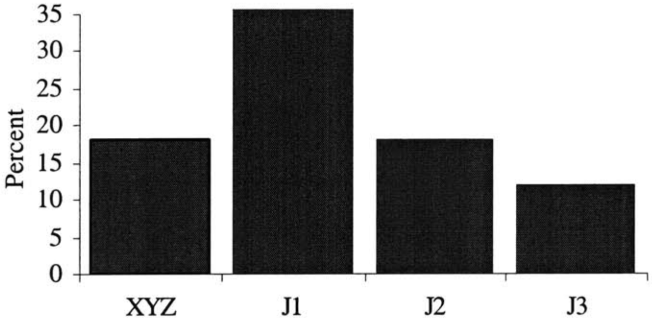

Figure 5.13 Histogram of referenced inputs for spherical joint

The critical input parameter is J1 and the relationship between the joint angle and the compensation is shown in Figure 5.14. The resultant form implies a cubic relationship between the axis 1 angle and the y-coordinate offset.

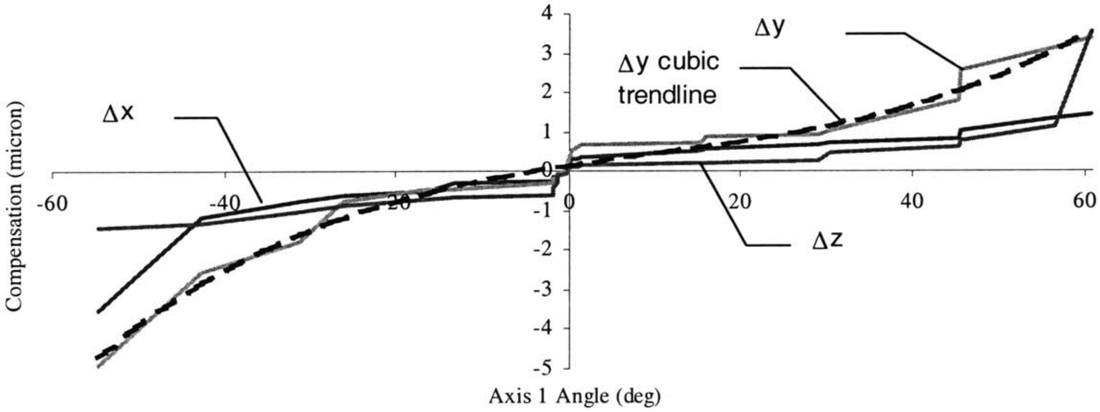

Figure 5.14 Linear sequence compensation for spherical joint

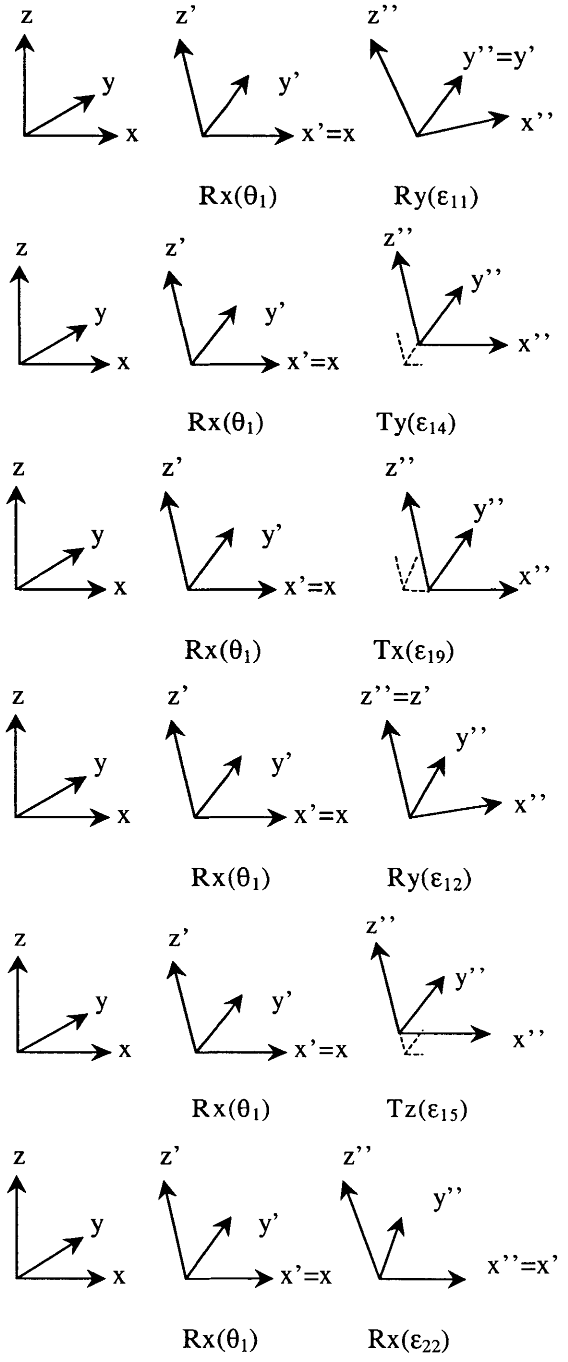
z
z'
z''
y
y'
y''=y'
x
x'=x
x''
Rx(θ1)
Ry(ε11)
z
z'
z''
y
y'
y''
x
x'=x
x''
Rx(θ1)
Ty(ε14)
z
z'
z''
y
y'
y''
x
x'=x
x''
Rx(θ1)
Tx(ε19)
z
z'
z''=z'
y
y'
y''
x
x'=x
x''
Rx(θ1)
Ry(ε12)
z
z'
z''
y
y'
y''
x
x'=x
x''
Rx(θ1)
Tz(ε15)
z
z'
z''
y
y'
y''
x
x'=x
x''=x'
Rx(θ1)
Rx(ε22)

Figure 5.15 Relationship between error parameters and axis 1 motion

The forward kinematic model parameters that are relevant for axis 1 are:

- Parameter 11. Y-axis rotation error.
- Parameter 12. Z-axis rotation error.
- Parameter 14. Y-axis translation error.
- Parameter 15. Z-axis translation error.

Figure 5.15 describes the kinematic sequence for each error parameter. The initial frame, denoted by (x, y, z) is rotated about its x-axis by the axis-1 angle (J1). The resultant frame is then rotated or translated (depending on the parameter) about another axis to produce the final frame position. Both y- and z-axis translation errors cause a significant effect in the y-coordinate. The evolved compensation curve indicates that the compensation error in the y-coordinate is zero when axis-1 is zero and increases in magnitude as axis-1 increases. Therefore, the relationship should be cosine dependent on axis-1 for the y-axis or sine dependent on axis-1 for the z-axis; note that these are equivalent and hence only one can be implemented. The z-axis parameter dependent on the cosine of the axis-1 angle is chosen for the calibration routine, resulting in the final set of calibration parameters is detailed in Table 5.2, and the accuracy distribution shown in Figure 5.16.

TABLE 5.2 Error parameters for improved joint model

Frame	Parameter	Index	Description
Tm_Ts	TxTyTz RxRyRz	1...6	Base frame
Tby_TCP	TxTyTz	7...9	TCP position
Ts_Tbr	Ry	11	Y-axis rotation error
Ts_Tbr	Rz	12	Z-axis rotation error
Tbr_Tbp	Ty	14	Y-axis translation error
Tbr_Tbp	cos(J1)*Ty	31	Y-axis translation error
Tbr_Tbp	Tz	15	Z-axis translation error
Tbp_Tby	Tx	19	X-axis translation error
Tbp_Tby	Rx	22	X-axis rotation error

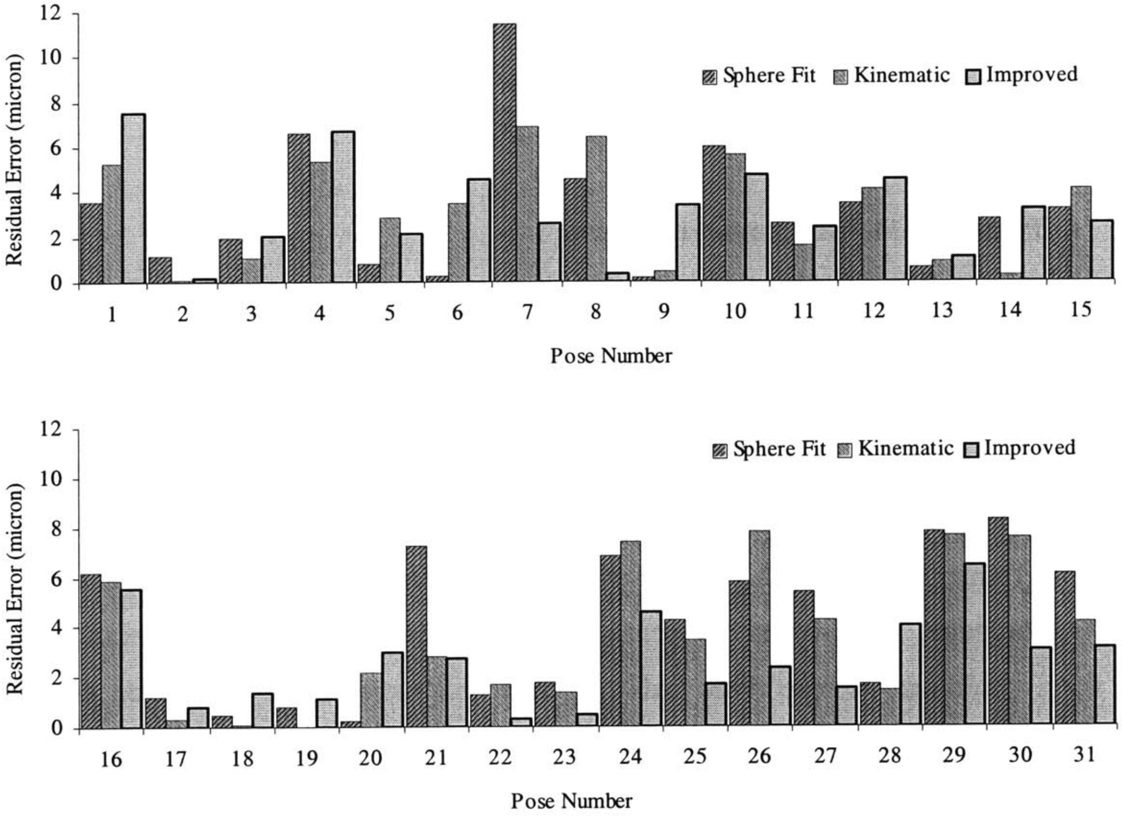

Figure 5.16 Accuracy distribution for improved joint model

The improved model is effective in some cases, reducing the maximum error by up to 50% compared to the kinematic model; furthermore, the average error is reduced from 3.5μm to 2.9μm. However, over the entire pose set, the maximum error remains the same at approximately 8μm; hence further improvements are still required in order to achieve a reduction in error similar to the robot calibration case.

5.4 Conclusions

Genetic Programming represents an effective technique for the optimization of complex calibration models. Through an evolutionary process, involving crossover and mutation of operation structures, equations can be derived for the required position compensation in the x, y and z coordinates. Whereas these equations are effective in minimizing the error for the input data, extrapolation to new positions typically results in accuracy degradation, suggesting that a direct implementation of the result is not be effective in solving the global accuracy problem. Due to the complexity of the evolved equations, a statistical analysis of the inputs referenced is used to indicate the potential source of remaining errors. Two physically based error models have been deduced through inspection and improvement of an existing robot model, resulting in a 50% reduction in the maximum error compared to the original model. A statistical approach is effective for improvement within the framework of the existing model, however it provides no intuitive information about more complex joint-based physical phenomena, such as backlash and friction. The evolved equations from the position-compensator are inherently complex due to the encoding of both the joint-based phenomena as well as the forward kinematics converting the joint space to Cartesian space. Working directly in joint space, via a joint-based compensator, could provide a more intuitive set of evolved equations. Implementation of the improved calibration model in a robot controller is required in order to confirm the robustness and accuracy of the simulation results. The goal of this approach is to achieve a maximum error of the order of the robot repeatability (0.1mm), indicating that the majority of non-stochastic error phenomena have been successfully modeled.

The spherical joint kinematic model is based on the robot manipulator concept and hence is also subject to improvement through the use of Genetic Programming. Using the linear sequence approach, a simple improved model is proposed, resulting in a decrease in mean error over the residual error distribution. The maximum error, however, remains relatively unchanged indicating that further work is required to achieve additional model improvements.

Chapter 6

CONCLUSIONS

Four spherical joint prototypes have been developed with the goal of high accuracy, high stiffness, and singularity free motion throughout a large hemispherical workspace. The key functional requirements are divided into three categories: spherical motion, contact type and preload. Spherical motion requires a singularity-free workspace of 180° and an accuracy on the order of several micrometers. Contact type considers the interaction between the elements of the joint assembly and considers lubrication, material selection and contact mechanics. Finally, preload determines the mechanism by which the joint is physically constrained, which in turn determines the joint's resultant stiffness and load capacity.

A five stage design process is used to develop the joint prototypes and determine appropriate testing mechanisms. At each stage: Requirements; Strategy; Concept; and Module; evaluation tables are used to determine and compare sets of viable alternatives; finally, the prototypes are constructed in the Manufacturing stage. The joint prototype structure is chosen to be a spherical ball housed in a hemispherical socket; preloaded with magnets arrayed in the socket. Four varying contact mechanisms: point, rolling, sliding and fluid contact represent the distinguishing characteristic between the joint prototypes. The point contact prototype mounts the ball kinematically on three smaller spheres embedded in the socket. The rolling contact joint significantly reduces friction, compared to the point contact concept, by kinematically mounting the ball on three rolling ball-transfers. The surface contact prototype uses replication with a teflon-laced epoxy to achieve a high-accuracy mating surface with low friction. The fluid contact joint extends the sliding contact joint by introducing an air film between the ball and replicated socket surface, reducing friction while maintaining a high accuracy interface. A spherical kinematic test rig is used to actuate each joint to a predefined position, which is measured by a coordinate measurement machine. The resultant un-calibrated accuracy of the joints is between 12 and 22μm, which is reduced by 30% to 8 to 18μm through calibration. The average accuracy throughout the workspace is determined to be 3 to 4μm.

A tensile testing machine is used to measure the load capacity of each prototype; the point and rolling contact joints display a preload force on the order of 50N while the sliding and fluid contact joints have a higher preload of 100N. The load capacity can be increased through the introduction of additional magnets about the socket, as well as by shunting the back-side of the magnets with a steel band.

A flat-plate Navier Stokes approximation is used to model the pressure and displacement characteristics of the fluid contact joint. The model agrees to within 10% for an air gap greater than 15 micrometers, and to within 20% for smaller air gaps. This discrepancy is believed to be due to non-uniformity of the wax interface layer and irregularities in the mold release during the replication process. The replication process could be improved through the use of a dedicated replication ball that is sized to be 10μm larger than the desired ball diameter to ensure a repeatable and smooth gap size and surface finish. The stiffness characteristics of the fluid contact joint are divided into three regimes: contact; fluid; and magnet; with the fluid regime representing the critical joint stiffness. The stiffness modeled using the flat-plate approximation agrees relatively well with the measured characteristics, yielding a stiffness of approximately 5N/μm. This stiffness can be improved by running the joint at a smaller air gap size, which is achievable through the improvement of the surface finish resultant from the replication process.

The kinematic calibration of the joint prototypes results in a residual error distribution that is highly varied. Genetic Programming is used to optimize the joint calibration model by evolving equations to improve the predicted joint end-effector position. Using the linear sequence approach, a simple improved model is proposed, resulting in a decrease in mean error over the residual error distribution. The maximum error, however, remains relatively unchanged indicating that further work is required to achieve significant model improvements.

Additional characterization of the joint prototypes involves the modeling and measurement of the joint damping; due to the friction in the point, rolling and sliding contact joints; and the air film viscosity in the fluid contact joint. Given the stiffness and damping parameters for each joint, a simple spring-mass-damper dynamic system can be proposed to model the dynamic performance of each joint. Measurement of the frequency response of each prototype can be used to experimentally determine the stiffness and damping, which can then be compared to the modeled and measured values determined through tensile and viscosity testing.

Chapter 7

REFERENCES

[Alam et al, 1999] M. Alam, C. Mavroidis, N. Langrana, P. Bidaud, "Mechanism design using rapid prototyping", The Tenth World Congress on the Theory of Mechanisms and Machines, 1999

[Bieg, 1999] L. F. Bieg, G. L. Benavides, "Double slotted socket spherical joint", United States Patent 6,234,703, 1999.

[Bernhardt et al, 1993] R. Bernhardt, and S. L. Albright (Eds.), "Robot Calibration", Chapman and Hall, 1993.

[Bryan, 1992] J. B. Bryan, *Telescoping magnetic ball bar test gage.* U.S. Patent 4,435,905, 1982.

[Brogårdh et al, 1998] T. Brogårdh, S. Ellqvist, *A device for relative displacement of two elements.* U.S. Patent 6,336,374, 1998.

[Brogårdh, 1997] T. Brogårdh, *A device for relative movement of two elements.* U.S. Patent 6,095,011, 1997.

[Bäck et al, 1993] T. Bäck, and H. P. Schwefel, "An overview of evolutionary algorithms for parameter optimization", Evolutionary Computation, 1993.

[Callister, 1994] W. D. Callister, *Materials Science and Engineering: An Introduction*, John Wiley and Sons, 3rd edition, 1994.

[Clavel, 1989] R. Clavel, *Device for the movement and positioning of an element in space.* U.S. Patent 4,976,582, 1989.

[Furlong, 1998] T. Furlong, J. Vance, P. Larochelle, "Spherical Mechanism Synthesis in Virtual Reality", ASME Journal of Mechanical Design Vol.121, No.4, 1999

[Hayati et al, 1985] S. Hayati, M. Mirmirani, *Improving the Absolute positioning Accuracy of Robot Manipulators*, Journal of Robotic Systems, 1985.

[Hvittfeldt et al, 2002] H. Hvittfeldt, J. Larsson, P. Mikaelsson, F. Persson, *Manipulator and method for manufacturing the manipulator.* U.S. Patent 6,419,211, 2002.

[Jefferson et al, 1991] D. Jefferson, R. Collins, C. Cooper, M. Dyer, M. Flowers, and R. Korf, "Evolution as a theme in artificial life: The Genesys/Tracker system", Proceedings of Artificial Life II, Addison–Wesley, 1991.

[Koza, 1990] J. R. Koza, "Non-Linear Genetic Algorithms for Solving Problems", United States Patent 4,935,877, 1990.

[Koza et al, 1997] J. R. Koza, F. H. Bennett III, M.A. Keane, and D. Andre, "Automatic Programming of a Time-Optimal Robot Controller and an Analog Electrical Circuit to Implement the Robot Controller by Means of Genetic Programming", Proceedings of the 1997 IEEE International Symposium on Computational Intelligence in Robotics and Automation (CIRA '97), 1997.

[Leica, 2002] Leica LTD500 Industrial Measurement System, Available: http://www.leica-geosystems.com.

[Lundberg et al, 1999] I. Lundberg, M. Andreasson, "Matematisk analys av en parallelkinematisk robot", Kungl Tekniska Högskolan, Examsarbete Rapport, 1999.

[Lundberg, 2001] T. Lundberg, "Mekatronisk implementering samt verifiering av Tau-prototyp, Kungl Tekniska Högskolan, Preliminär Rapport, 2001.

[OMAX, 2002] OMAX Waterjet 2626, Available: www.omax.com.

[Powell, 1970] J. W. Powell, *Design of Aerostatic Bearings Machinery.* Publ. Co. Ltd. London, 1970.

[Ray, 1992] T.S. Ray, "An approach to the synthesis of life", Artificial Life II, Vol X, Addison-Wesley, 1992.

[Robertson et al, 2002] A. P. Robertson, C. Dumont, "Design of Robot Calibration Models Using Genetic Programming", International Symposium on Robotics and Automation, Mexico, 2002.

[Shröer et al, 1997] K. Shröer, Albright S.L., and Lisounkin A., "Modeling closed-loop mechanisms in robots for purposes of calibration", IEEE Transactions on Robotics and Automation, vol. 13, num. 2, 1997, pp. 218-229.

[Simms, 1994] K. Simms, "Evolving Virtual Creatures", Computer Graphics Annual

Conference Series (SIGGRAPH'94), July 1994, pp.15–20.

[Slocum, 1992] A. H. Slocum, *Precision Machine Design*, Society of Manufacturing Engineers, 1992.

[SMS, 2003] Stable Micro Systems TA-XTPlus, Available: www.stablemicrosystems.com

[Wright, 1991] A. H. Wright, "Genetic algorithms for real parameter optimization", Foundations of Genetic Algorithms, Rawlins, G. (Ed.), 1991.

[Yoneda et al, 1990] Yoneda, Takao, Komura, and Katsuhiro, "Method and apparatus for controlling a robot using a neural network", United States Patent 5,555,347, 1990.

[Zwick, 2003] Zwick testXpert, Available: www.zwick.com

2853-62